Project KORSO

Anaerobic Corrosion of Stainless Steel 309S at High Temperatures and Pressures in Geological Relevant Brines

GRS - 624

Gesellschaft für Anlagen-
und Reaktorsicherheit
(GRS) gGmbH

Project KORSO

Anaerobic Corrosion of Stainless Steel 309S at High Temperatures and Pressures in Geological Relevant Brines

Andrés G. Muñoz (GRS)
Dieter Schild (KIT - INE)

December 2020

Remark:

This report refers to the research project 02E11496A which has been funded by the German Federal Ministry of Economic Affairs and Energy (BMWi).

The study was conducted by the Gesellschaft für Anlagen- und Reaktorsicherheit (GRS) gGmbH in cooperation with the Karlsruhe Institute of Technology (KIT).

The authors are responsible for the content of the report.

GRS - 624
ISBN 978-3-949088-12-4

Key-Words:
AISI 309S, Corrosion Mechanisms, High-Temperature Corrosion, Localized Corrosion, Salt Films, Stainless Steel

Table of contents

1 Introduction

The selection of a host rock for a deep repository of high-level radioactive waste is a subject of ongoing debate in Germany. In 2017 the German Government passed the law for the search and selection of a site for a final storage facility for high-level radioactive waste /STA 2017/. This law establishes the framework for the location of an appropriate final disposal of high-level radioactive waste. As host rocks, salt rock, claystone and crystalline are considered. Recently, the German institutions GRS, BGR and BGE-TEC reported a compilation of technical fundamentals (RESUS-project) to evaluate the feasibility of candidate sites as final disposal /MOE 2020/.

Salt rock, which is present beneath the entire north of Germany offers an advantageous hydraulic impermeability, which, if the repository is constructed and managed properly, renders a very low probability of direct contact between waste containments and aqueous solution /BER 2016/. However, it cannot be excluded altogether that the repository undergoes an unforeseen evolution, where the steel containment of high-level radioactive waste undergoes a contact with geological waters. This will be in any case a near saturated brine.

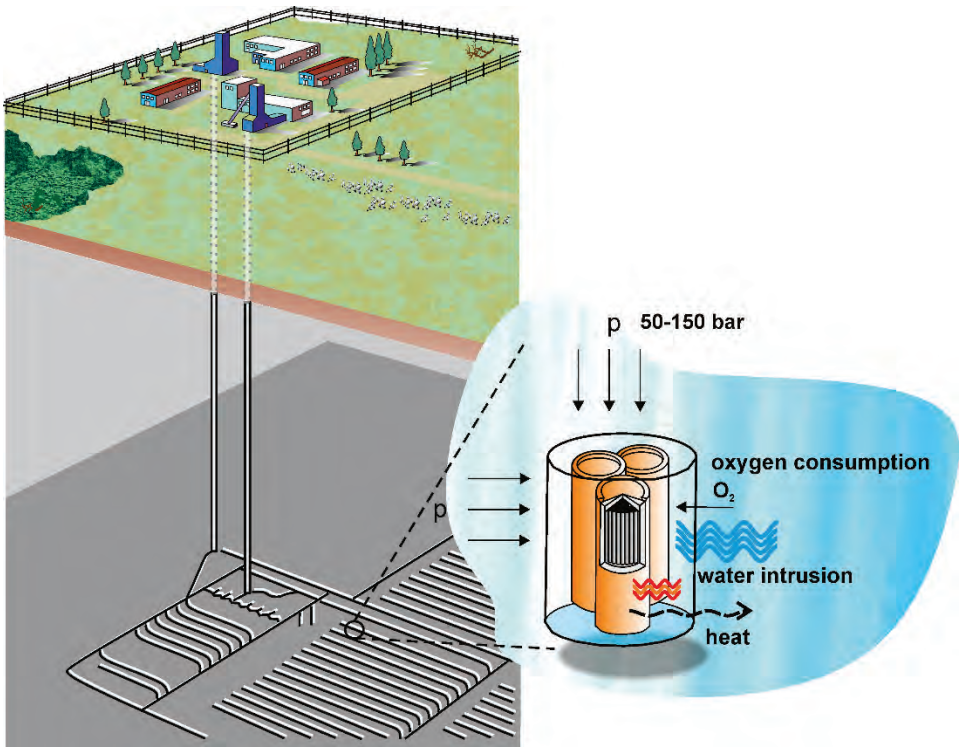

Fig. 1.1 Generic graphic representation of the environment developed in a repository in the case of water intrusion, adapted from /KIN 2020/

The design of containers in the repository concepts envisaged for Germany /HAS 2019/, /BER 2017/ consist of a multi-barrier system where materials are selected according to mechanical and corrosion resistance requirements. The container Pollux® 10 is taken as a reference for the storage of fuel elements in the different types of host rocks. This container consists of an overpack from spheroidal graphite carbon steel (GGG 40 / 0.7040) which has a shielding function. Polyethylene rods are embedded in the body of the container for neutron shielding purposes. The inner container is made of low-alloyed steel 1.6210 which encloses the fuel basket tubes made from stainless steel 1.4541.

The austenitic stainless steel 1.4833 is a heat-resistant material with a high corrosion resistance and good weldability used in the construction of inner vessels of containers /PEI 2011/. Therefore, the study of the corrosion of this material is of great relevance in the case of a corrosion degradation of the container. In other types of European disposal concepts in clay, this material is recommended for the construction of the inner container /BEN 2008/.

The metallic corrosion in the environment developed after the closure of the repository will define the overall performance and longevity of the steel-based containment. Predictive calculations of the evolution of the near-field environment were reported for a deep geological disposal in saturated host rock /KIN 2010/, /KIN 2010a/, /KIN 2006/. Fig. 1.2 shows a representative graphic showing a prediction of the evolution of temperature, oxygen concentration and humidity. The first period after emplacement is characterized by a warm and aerobic environment. After about 30 years it turns colder, wet and anaerobic because of the decay of the heat generation by the fission products and the consumption of oxygen by reaction with the container wall, microbes, and minerals in the surrounding rock and backfill materials. At this point, the condensation of water may bring about an aggressive environment which increases the probability of a container damage by corrosion, especially if localized corrosion in its different types occurs: pitting corrosion, crevice corrosion, stress corrosion cracking and hydrogen induced cracking.

The expected temperature maximum can vary depending on the type of deep geological disposal concept. The temperature increase over the natural value in the host rock may enhance the corrosiveness of the environment, governed in principle by the chloride concentration of the groundwater, see analysis reported by Shoesmith /SHO 2006/ Fig**.** 1.3.

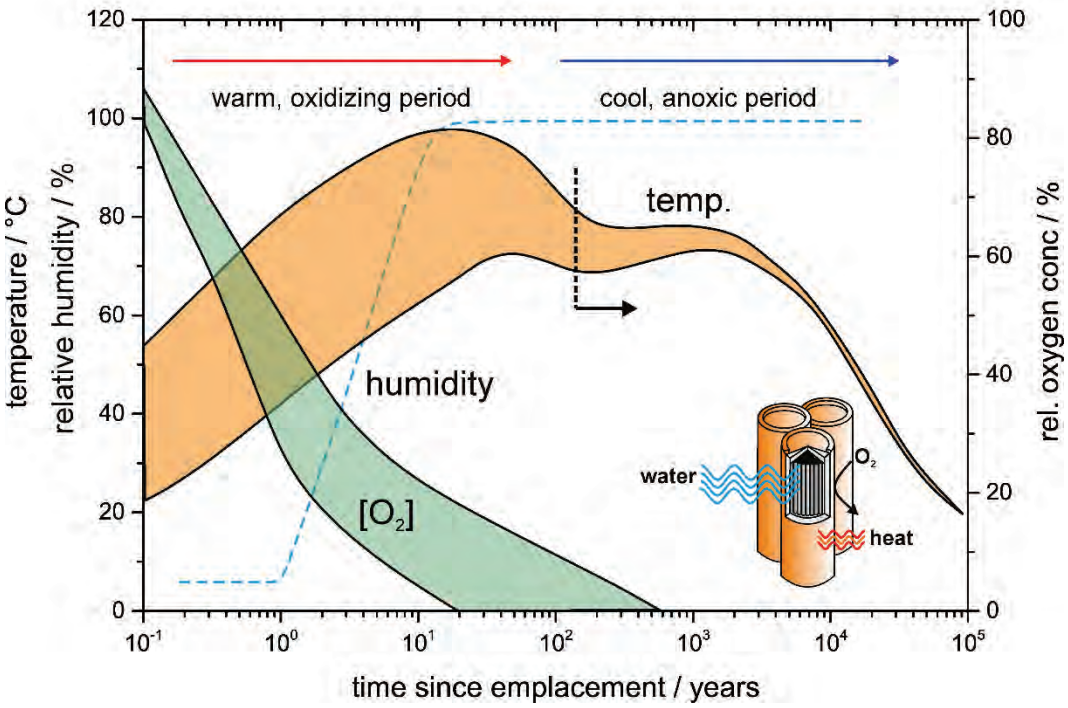

Fig. 1.2 Schematic evolution of the near-field environment of a repository (after /SHO 2006/)

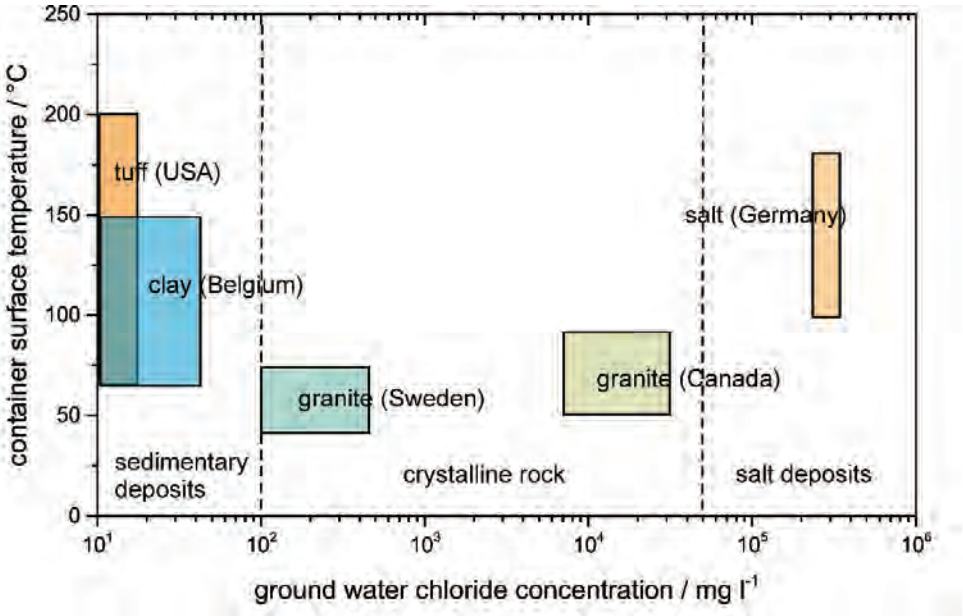

Fig. 1.3 Comparative diagram showing temperature ranges and water chloride concentration in several national nuclear waste management programs (after /SHO 2006/)

Apart from the high temperatures and the large ionic strength of the contacting medium, the corrosion may be influenced by the large hydrostatic and lithostatic pressures, which can vary from 50 to 250 bar /GRA 2016/. King et.al. /KIN 2014/, /KIN 2007/ presented a comprehensive analysis of the corrosion of carbon steels in pore water regarding the evolution of the environmental conditions in a bentonite based deep geological repository. In the presence of humidity, the corrosion of iron starts with an initial aerobic phase described by:

$$\mathbf{Fe + H_2O + ½\ O_2 \rightarrow Fe(OH)_2} \quad (1.1)$$

$$\mathbf{Fe(OH)_2 + O_2 \rightarrow 2\ (\alpha,\gamma)\text{-}FeOOH + 2\ H_2O} \quad (1.2)$$

$$\mathbf{2\ (\alpha,\gamma)\text{-}FeOOH \rightarrow Fe_2O_3 + H_2O} \quad (1.3)$$

After the consumption of enclosed oxygen, corrosion continues according to:

$$\mathbf{Fe + 2\ H_2O \rightarrow Fe(OH)_2 + H_2} \quad (1.4)$$

The formed iron hydroxide can further convert to Fe_3O_4 via the Schikkor reaction:

$$\mathbf{Fe(OH)_2 \rightarrow Fe_3O_4 + 2\ H_2O + H_2} \quad (1.5)$$

The corrosion of iron may have a large impact on the migration of radioactive contaminants that have been mobilized from the waste matrix. For instance, the use of iron was pondered as a method for the removal of uranium from the groundwater /FAR 1999/, where the precipitation of uranyl to slightly soluble U(IV) products and the adsorption of uranium species on iron corrosion products are the main retention mechanisms. The waste container design based in a multibarrier concept should offer anytime the warranty for the barrier integrity during the tens of thousands of years, as demanded by regulatory limits for crystalline formations. Thus, an adequate selection of materials provides at least, a mean to control the release of radionuclides from the possibly failed container. As the groundwater gains access to interior of the container, carbon steel liners corrodes under anoxic conditions releasing Fe(II) and hydrogen. Both products act as scavengers for the radiolytic oxidants which induce the formation of soluble U(VI) products during the corrosion of spent fuel (UO_2) /SHO 2003/.

Three exemplary materials are commonly considered in repository concepts in Germany: stainless steel 1.4833 AISI 309S, low carbon steel 1.6210 and nodular carbon steel 0.7040 (GGG40). Due to the complexity of the corrosion behavior of stainless steel (1.4833 AISI) 309S, the electrochemical studies were focused on this material.

Although austenitic steels present a strong passivity, they are susceptible to pitting corrosion over a certain chloride concentration threshold /LEC 1966/, /SMA 2003/. Olsson and Landolt /OLS 2003/ stated that the passive film consists of a strongly chromium enriched oxide without incorporation of Ni, whereas the metal closest to the metal-film interface is strongly enriched in nickel. The susceptibility of stainless steels to pitting corrosion can be evaluated by the pitting resistance equivalent number (PREN), given by /SED 1996/:

$$\textbf{PREN = \%wt Cr + 3.3 \%wt Mo + 16 \%wt N} \quad (1.6)$$

Accordingly, the susceptibility to pitting decreases in the order (AISI): 304L > 316L ≈ 309S > 904L. The chloride content and the temperature of corroding media shift the breakdown and repassivation potentials towards more negative (active) values /LAY 1998/. A critical situation arises, as the repassivation potential (E_{pp}) moves to values more negative than the free corrosion potential (E_{corr}) without chloride. In this case, pits cannot nucleate, but once initiated by an occasional local attack they would not be able to repassivate. Kursten et al found that at 90°C this situation is attained as the chloride concentration increases over 0.24 mol L^{-1} and 0.93 mol L^{-1} for 316L and 904L respectively in a solution containing 0.018 mol L^{-1} SO_4^{-2} under anoxic conditions /KUR 2007/. The E_{corr} for 316L and 904L sets at -0.25 V in a solution containing 4.6×10^{-4} mol L^{-1} of Cl^- and 0.018 mol L^{-1} SO_4^{2-} at 16 °C. Thus, these materials are susceptible to undergo long-term corrosion problems because of localized attack under the conditions prevailing in salt rock disposals, with almost saturation concentration of chloride and high temperatures.

The aim of this work is to gain a comprehensive knowledge about morphological and chemical aspects of the localized corrosion of stainless steel 309S under conditions close to those found in a geological disposal after the hot oxidant period, i. e., geological relevant salt solutions, anoxic atmosphere, pressures over 50 bar and temperatures near 90 °C. To understand the analysis methodology followed in this work, based fundamentally in polarization experiments, some corrosion concepts must be briefly reviewed. The metal corrosion is the result of electrochemical anodic and cathodic half-

reactions which take place spatially separated. This separation distance can vary from atomic to macroscopic dimensions. Fig. 1.4a represent the particular case of a pit, where the anodic metal dissolution is supported by cathodic reactions, which in anoxic conditions are circumscribed to the reduction of water and protons. The breakdown of the passive film by chloride ions, either through dissolution of the oxide film or by penetration, induces a lateral change of the surface potential $\Delta^m\phi^s$ drop between metal and solution. These potentials are determined by the kinetics of coupled anodic and cathodic reactions, which in turn depend on the local steel composition and the chemical environment locally developed by these reactions. For instance, steel phases, e. g. intermetallic particles, with a standard electrochemical dissolution potential more positive than that for the alloy matrix will preferably act as cathodic sites, thus enhancing the dissolution rate of active sites.

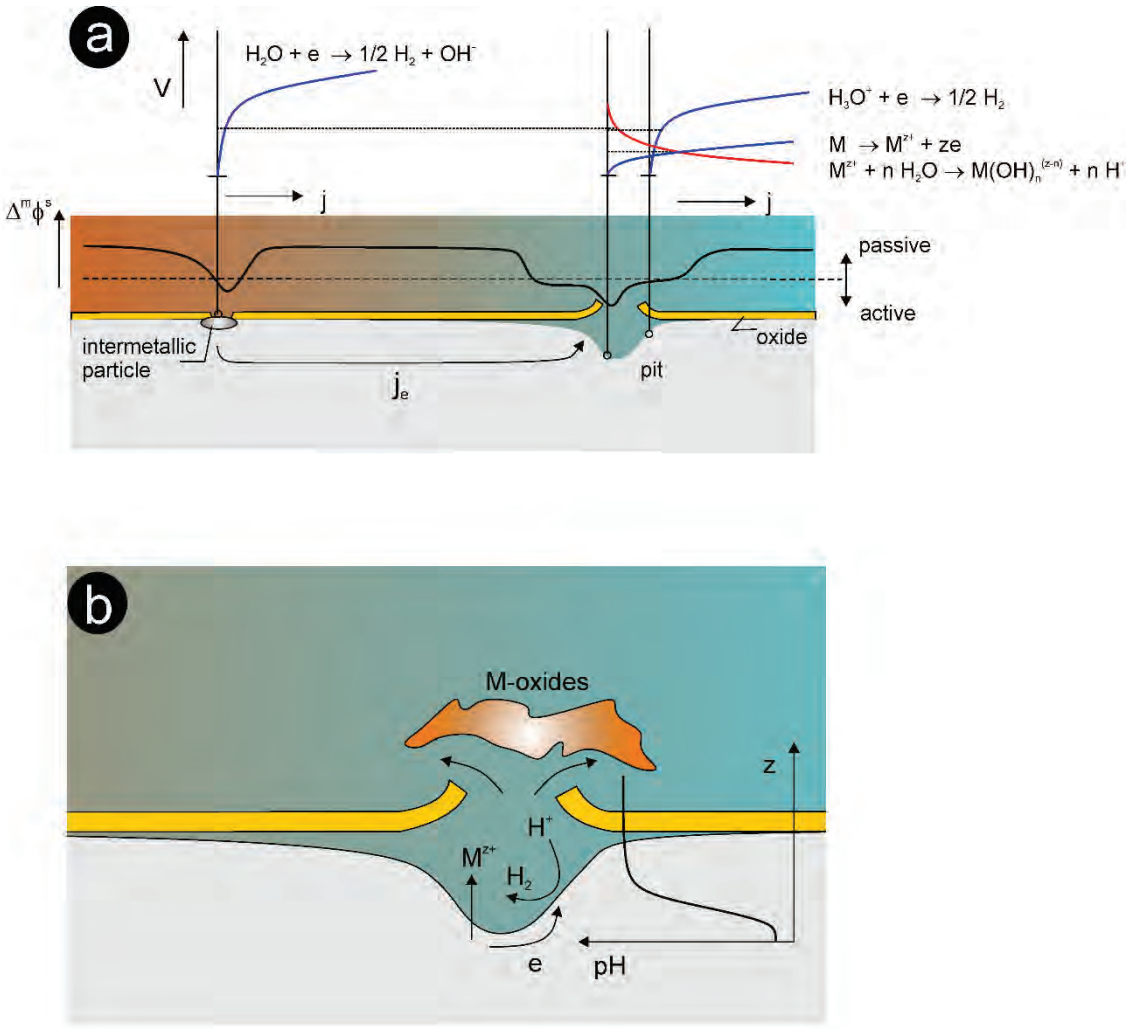

Fig. 1.4 Schematic representation of corrosion processes taking place on a naturally passivated steel surface.

The metallic ions released by dissolution inside the pit hydrolyze. As a result, the solution is locally acidified, enhancing the rate of proton reduction. This sustains a further metal dissolution, and the pit depth increases (see Fig. 1.4b). This process stops once repassivation of the active site occurs assisted by the accumulation of oxide products and/or the convective mixing arising upon the rupture of the formed cavity.

The controlled polarization of the substrate by using a potentiostate allows the half-reaction to be studied separately (schematically represented by the red curve in Fig. 1.4a). In this work, the kinetics of the anodic dissolution is emphasized. The influence of the steel structure and composition as well as the developed local chemical environment thereon was investigated.

For this study, electrochemical polarizations combined with open circuit potential measurements and electrochemical impedance were performed on steel 309S in a special designed cell to work at high temperatures and high pressures under anoxic conditions. The attacked surfaces were analyzed by SEM-EDX (scanning electron microscopy – energy dispersive X-ray spectroscopy) and XPS (X-ray photoelectron spectroscopy).

This challenge was undertaken by the institutions Gesellschaft für Anlagen- und Reaktorsicherheit (GRS) gGmbH and the Institute for Nuclear Waste Disposal (KIT-INE), Karlsruhe Institute of Technology.

2 Experimental details

2.1 The electrochemical cell

The electrochemical cell was designed to work under pressures up to 150 bar and temperatures up to 120 °C. It consists of a pressure reactor of stainless steel 1.4571 (3016Ti) manufactured by the company Berghof Products + Instruments GmbH. The reaction vessel is made from PTFE (polytetrafluoroethylene). The cover of reactor is also lined with PTFE to protect it against strong corroding working conditions. The temperature control is made by a computer commanded loop including a thermocouple and an electric heating mantle. Due to the poor heat conductivity of PTFE, the temperature setting inside the reactor takes a time not shorter than 1 h depending on the final input value. The reactor is pressured by injecting nitrogen through a gas sampling valve. The input pressure is controlled by a computer-commanded pneumatic system connected to a compressed air source.

For the construction of the electrochemical reactor, electrodes specially designed for working at pressures up to 150 bar and temperatures up to 150 °C were purchased from Corr Instruments, USA. Fig. 2.2 shows some technical details of these electrodes. The upper part of the electrodes is sealed with Queon™, an insulating material with high sealability under high pressures and temperatures. In our case, the metal parts of the electrode were made from titanium. An external type reference electrode was used, where the sensor interface is located at the upper part of the electrode, i.e. the reference potential is referred to the external temperature. A 5 x 5 mm Pt-Ir sheet was welded at the end of the Pt wire of the counter electrode.

2.2 Preparation of sample

The working electrodes consisted in pieces of 6 x 6 x 4 mm of austenitic steel 309S which were cut with a water jet cutter from a 2 x 2 m commercially available sheet. This avoids structural and local chemical modifications of the material. An enameled cooper wire was soldered on the upper part of the cube. This assembly was imbedded in Araldite®. The chemical and electrical insulating resin was abraded at one lateral side with 120-grit paper. The test face was further polished with 600-, 1000-grit paper and mirror finished with 6 μm- and 1 μm diamond suspension.

Prior to the experiments, fresh polished samples were cleaned by sonicating in the following sequence of baths for 5 min in each one: propanol, acetone, ethanol and finally water. The samples were wiped with powder-free paper and plugged in at the pin of the working electrode using ferrules. The encapsulated steel samples were introduced in the reactor with its polished face in vertical position.

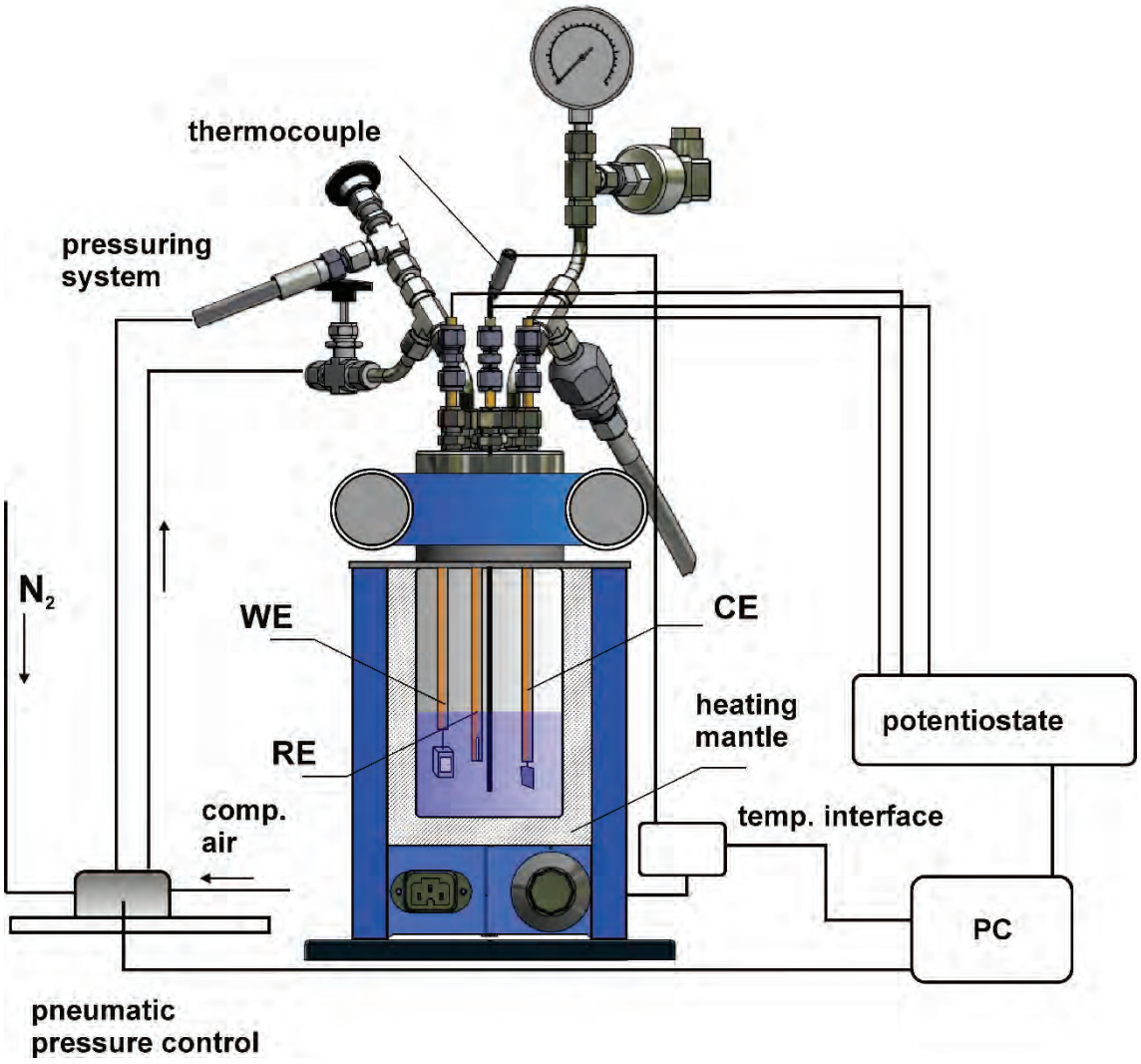

Fig. 2.1 Schematic showing the high-temperature, high-pressure electrochemical cell system for corrosion studies. WE: working electrode; CE: counter electrode; RE: reference electrode

As already mentioned in chapter 1, austenitic steel 309S is considered a candidate for the fabrication of a steel barrier in containment systems for the disposal of radioactive waste. This material is characterized by a high mechanical resistance, toughness, and

excellent high-temperature oxidation resistance provided by its high chromium and nickel content. The low carbon level reduces carbide precipitation during welding or high temperature applications. The chemical composition of the provided steel is given in Tab. 2.1.

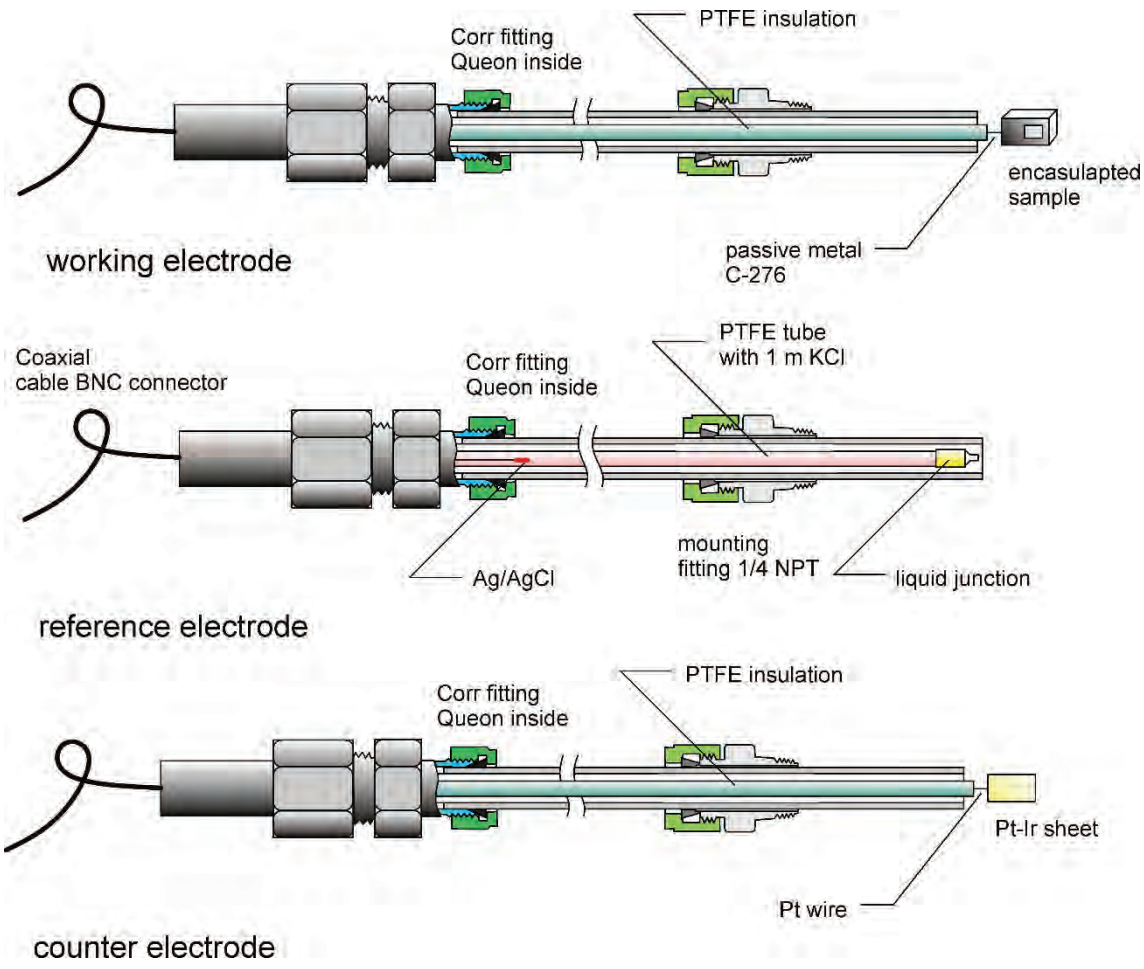

Fig. 2.2 High-pressure, high-temperature electrodes used for electrochemical experiments

The Schaeffler diagram /SCH 1949/ can be used to get a first notion of the microstructure of the austenitic steel. This diagram is generally applied to predict weld metal microstructure and weldability of stainless steels in general. The coordinates of this constitutional diagram are the equivalent $\%Cr_{eq} = \%Cr + \%Mo + 1.5 \times \%Si + 0.5 \times \%Nb$ and $\%Ni_{eq} = \%Ni + 30 \times \%C + 30 \times \% N + 0.5 \times \%Mn$, a concept based on ferritic and austenitic stabilizing elements respectively. Steel 309S is localized in a region with a low

tendency for the formation of ferrite, from which, in turn, the precipitation of the CrFe σ-phase may occur. Fig. 2.4 shows the ternary equilibrium diagrams for the the system Fe-Cr-Ni at various temperatures. They show, as already indicated in the Schaeffler diagram, that ferrite, with a composition of %wt 57.5 Fe, %wt 36 Cr and %wt 6.5 Ni is segregated in small proportions from the austenitic matrix during the solidification of the alloy. At 900 °C, ferrite transforms partially in the intermetallic σ-phase.

Tab. 2.1 Chemical composition of the stainless steel 309S as reported by the manufacturer (ThyssenKrupp- Acciai Speciale Terni S.p.A)

element	**C**	**Mn**	**Si**	**P**	**S**	**Cr**	**Ni**	**Mo**	**N**	**Cu**
% mass	0.061	1.15	0.35	0.023	0.001	22.45	13.17	0.23	0.027	0.23
% at	0.279	1.150	0.684	0.040	0.002	23.73	12.33	0.131	0.106	0.198

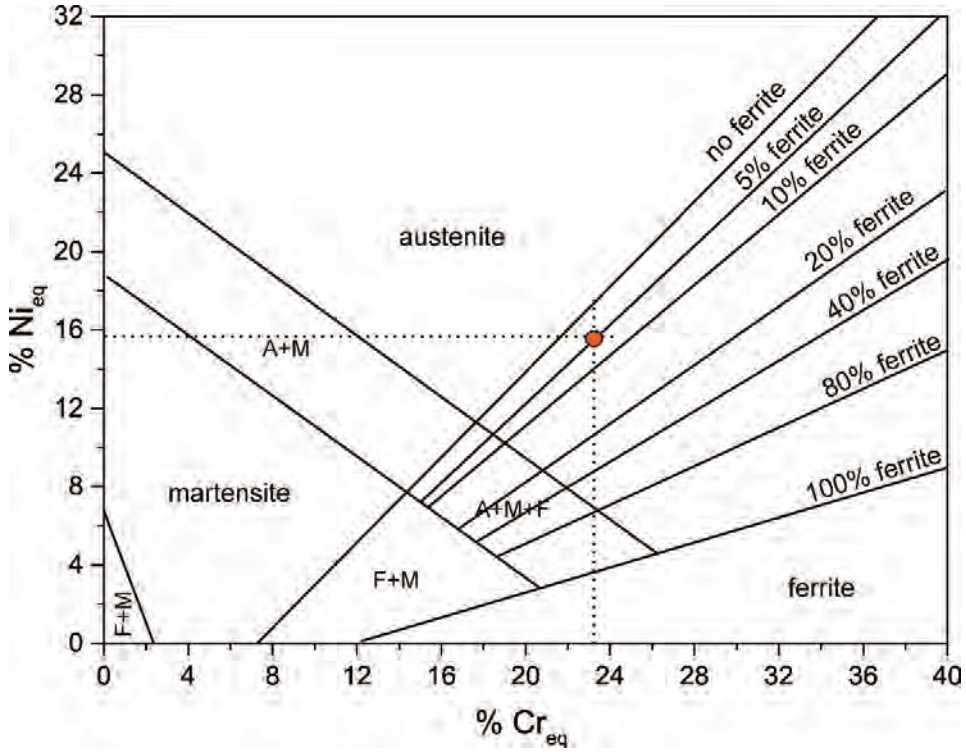

Fig. 2.3 Schaeffler constitutional diagram with indication of the composition of steel 309S (orange circles)

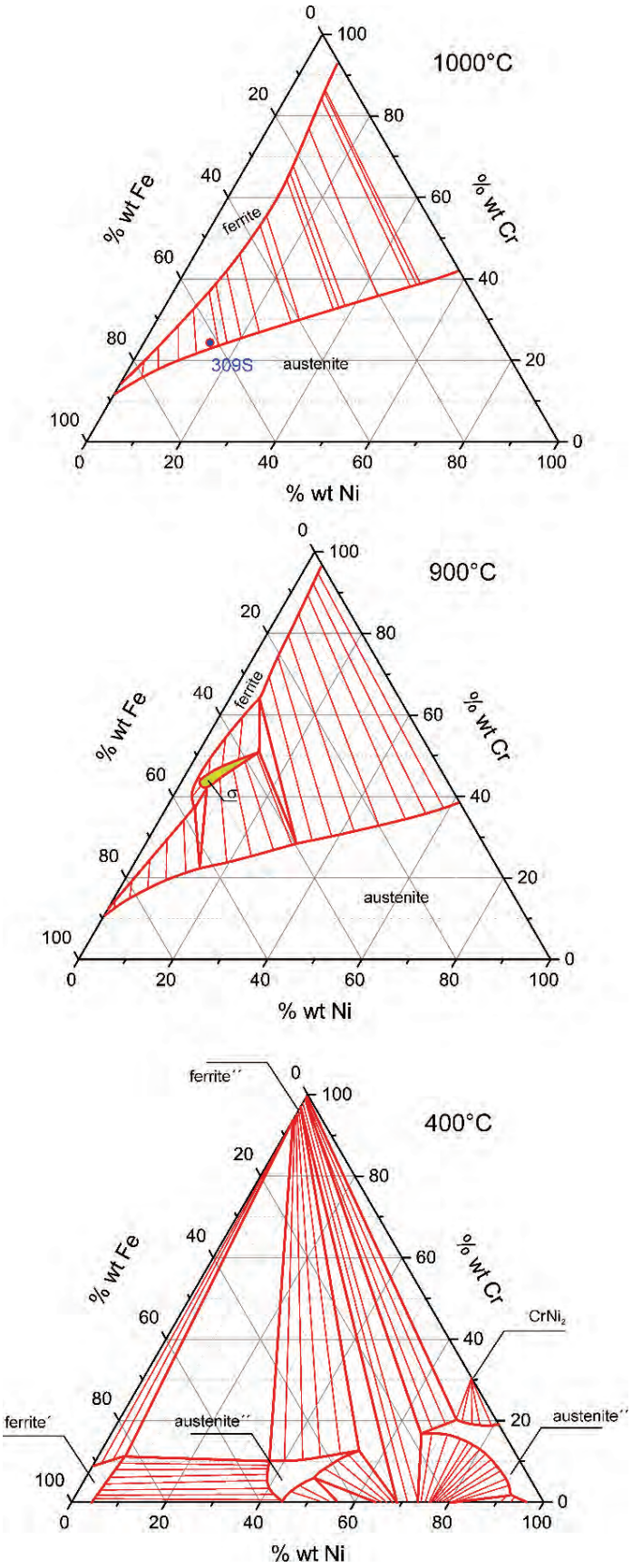

Fig. 2.4 Ternary phase diagrams for the Fe-Cr-Ni system at different temperatures /FRA 2011/

At lower temperatures, an eutectic reaction occurs with the segregation of ferrite with a composition of %wt 83 Fe, %wt 11 Cr and %wt 6 Ni, austenite: %wt 53 Fe, %wt 36 Cr and %wt 11 Ni and a Cr-rich phase with %wt 7 Fe and %wt 93 Cr.

2.3 Geological relevant solutions

Geological representative solutions, known as Q2- and Q3-brines were used for the corrosion experiments /KIE 2001/. The former is a high concentrated $MgCl_2$-$CaCl_2$ solution, which approaches the composition of brines obtained during drilling explorations in Gorleben. These solutions were characterized by a variable $CaCl_2$ content and a low pH value. The latter is a NaCl-saturated solution approaching the solution that emerges after the backing out of the salt rock during the normal operation of the mine in Gorleben. The composition of both types of solution are listed in Tab. 2.2. The solutions were prepared according to the receipts recommend in reference /KIE 2001/.

Tab. 2.2 Chemical composition of brines used in corrosion experiments

salt	**Q2**		**Q3**	
	g/l	**mol/kg**	**g/l**	**mol/kg**
NaCl	4.13	0.053	311.57	5.98
KCl	1.42	0.021	-	-
$MgCl_2$	438.90	3.54	-	-
$CaCl_2$	29.90	0.20	-	-
$CaSO_4$	0.040	3.86×10^{-4}	2.54	1.55×10^{-2}
K_2SO_4	-	-	2.82	1.35×10^{-2}
$MgSO_4$	-	-	1.95	1.35×10^{-2}

2.4 Analytical techniques

The study of the corrosion mechanisms of steel 309S in geological brines was carried out by applying electrochemical techniques as linear polarization, chronoamperometry and electrochemical impedance. The three-electrode cell shown in Fig. 2.1 was connected to an electrochemical interface Solartron 1287A for potential and current control. For the impedance measurements, a frequency analyzer Solartron 1260 was additionally assembled. Electrochemical runs were commanded with the software CorrWare and ZPlot/ZView designed for the Solartron equipment.

Experiments were performed at different temperatures ranging from 30 °C to 90 °C and pressures of 6 bar and 50 bar, referred further in the text as low and high pressures. The solutions were purged prior to the experiment during at least 20 min with Ar before they were poured into the reactor.

In selected cases, the samples were taken out from the reactor after the electrochemical experiment, washed with pure deaerated water and dried under an Ar stream. They were immediately stored into a glove box to avoid contact with air. For the surface analysis, the samples were transported from our glove box to the glove box in the Labs from KIT using a hermetic tube filled with nitrogen. In this way, we could ensure, that corrosion products generated in the electrochemical experiments do not alter by air oxidation during transport.

For XPS analyses, air sensitive samples from electrochemical experiments were mounted under anoxic conditions on a sample holder and transferred into the analysis chamber of the XPS-equipment using a gas-tight transfer vessel. XPS spectra were recorded with a PHI 5000 VersaProbe II system (ULVAC-PHI Inc.). It is equipped with a scanning microprobe X-ray source (monochromatic Al Kα 1486.7 eV) in combination with an electron flood gun and a floating ion gun generating low energy electrons (1 eV) and low energy argon ions (6 eV) for charge compensation of isolating samples (dual beam technique). The base pressure inside the spectrometer was about 2×10^{-7} Pa. The angle between sample surface and analyzer was set to 45°. Survey scans were recorded with pass energy of 187.85 eV of the analyzer and X-ray beam spot sizes of 24 µm or 200 µm of diameter at X-ray source power of 5 W or 30 W, respectively. In case of small sample features, scanning X-ray imaging (SXI) with X-ray spot size of 5 µm was applied to define positions of analysis areas. Survey scans were used to identify the elements and to determine their relative atomic concentrations (except hydrogen) by areas of elemental

lines after Shirley background subtraction, elemental sensitivity factors, and transmission function of the analyzer. The relative error of atomic concentrations is expected to be within ± (10 – 20) %. Data analysis was performed using ULVAC-PHI MultiPak program, version 9.8. Chemical bonding states were identified by comparison with binding energies reported in the literature. A scanning electron microscope (FEI Quanta 650 FEG) equipped with a silicon drift EDS detector (Thermo Scientific, Noran System 7) was used for imaging and X-ray microanalysis of sample surfaces.

3 Polarization Experiments in Q3 solution

A first insight into the corrosion behavior of the steel 309S in geological brines was gained by cyclic polarization curves performed at different temperatures in Q3 solution at a moderate pressure (3-6 bar). Some representative current-voltage curves are shown in Fig. 3.1.

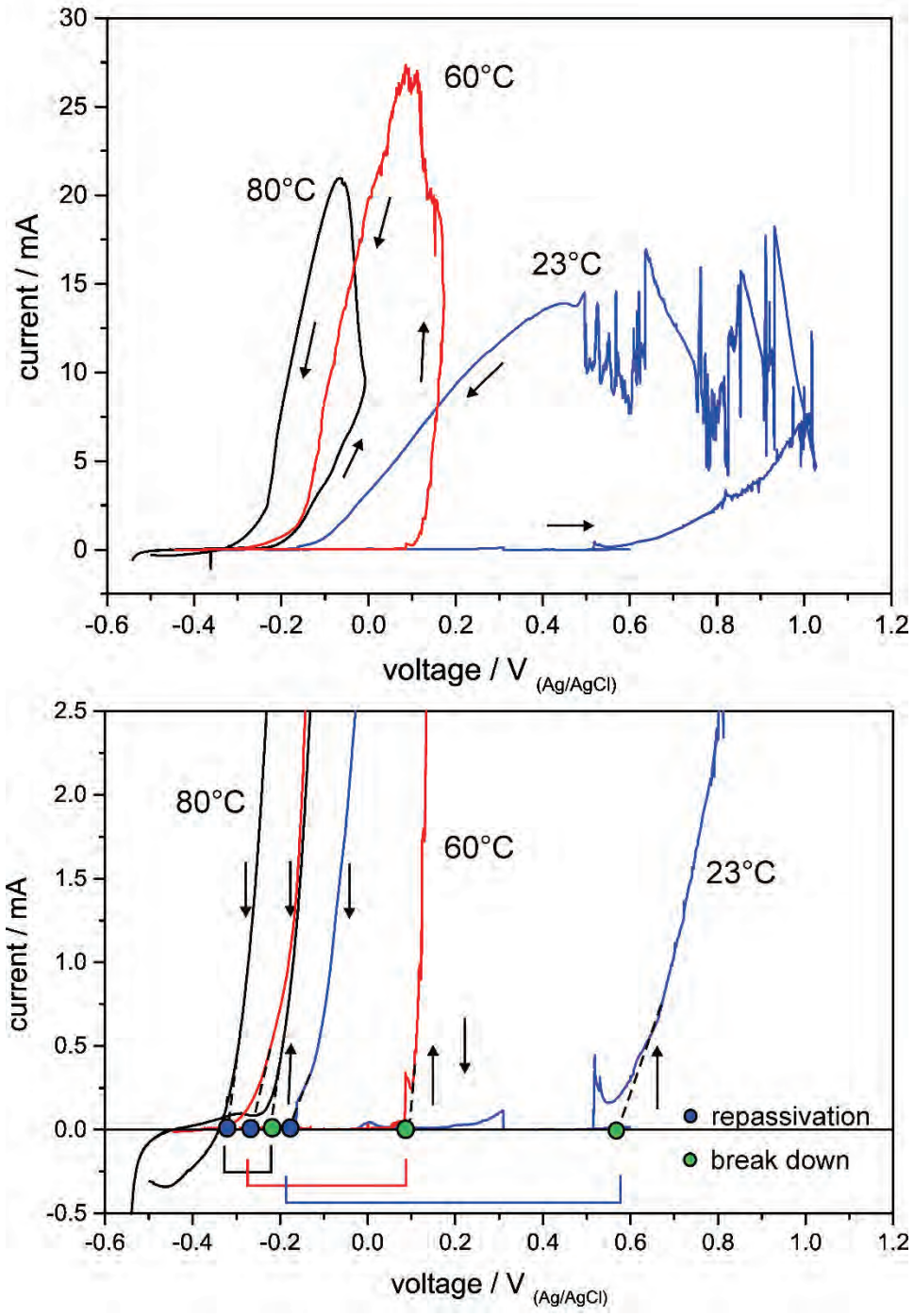

Fig. 3.1 Linear polarization of steel 309S in Q3 solution at different temperatures and at 3-6 bar pressure. Scan rate: 0.001 V s^{-1}

Starting at a voltage of 0.2 V cathodic from the rest potential ($E_i = E_{rest}$ -0.2 V), the forward anodic scan was reversed as the anodic current approaches to 10 mA. The curves show a current loop, the size of which decreases with temperature, shortening the passive potential region. This latter is characterized by strong oscillating currents between 10^{-4} and 0.1 mA until the steeply increasing onset of anodic current occurs. This type of electrochemical behavior is a clear evidence for a localized type of attack.

The potential at which the onset of anodic current occurs is known as break down potential. In the reverse scan, the current continues growing due to the enlargement of the anodic active area. The current reaches a maximum and then decreases smoothly and almost linearly until to reach the passive line. This point is known as the repassivation potential. The decrease of current indicates a stopping of the growth of the anodic dissolving area. The linear current-voltage behavior, on the other hand, denotes an ohmic control of the dissolution process, generally ascribed to the formation of a salt film at the metal-solution interface /BEK 1979/, /BEK 1984/, /MUN 1999/.

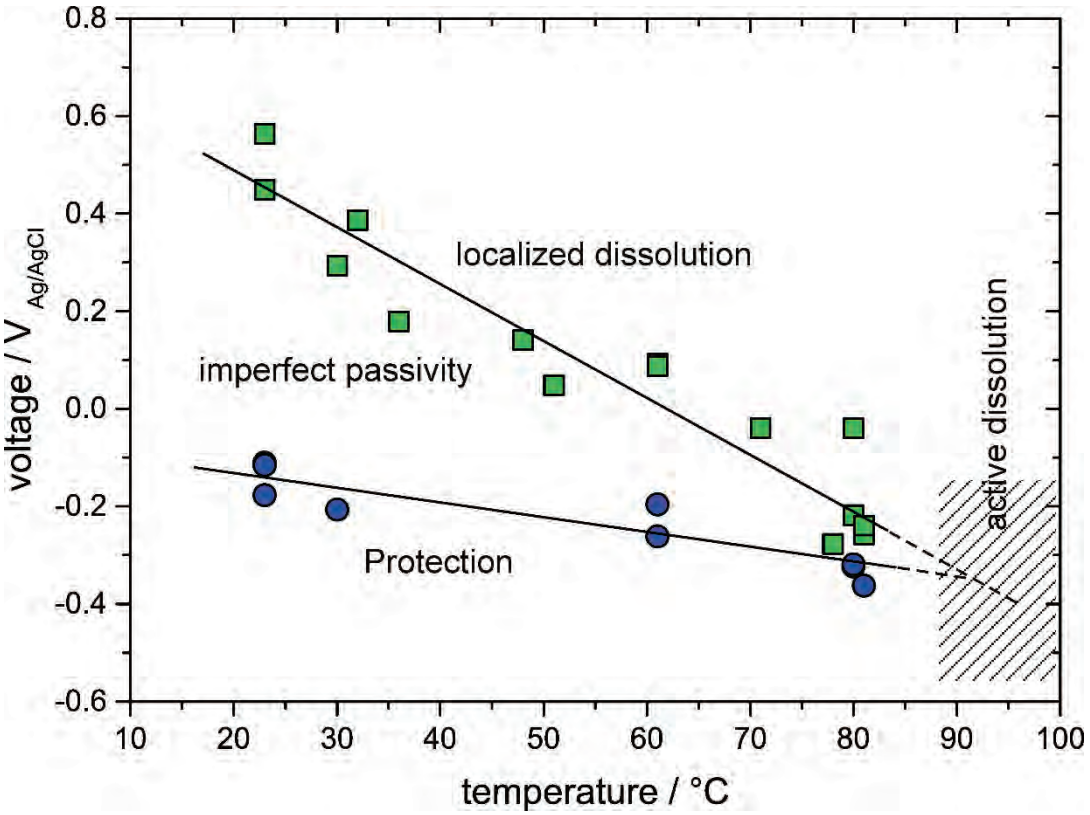

Fig. 3.2 Breakdown (green) and repassivation potentials (blue) measured at different temperatures on polarization experiments at 0.001 V s^{-1} in Q3 solution and p = 6 bar

Breakdown and repassivation potentials are indicated with green and blue points in Fig. 3.2. It can be noted that the passive behavior of steel decreases with temperature. The relatively large dispersion of break down potentials is a consequence of the stochastic nature of the breakdown process and the related dependence of the scan rate. Breakdown and repassivation potentials approach to each other with a loss of the corrosion resistance and the onset of active dissolution behavior at temperatures higher than 80 °C (indicated with dashed region in Fig. 3.2)

3.1 Localized corrosion at room temperature and low pressures

Fig. 3.3 show SEM images of the steel electrode surface after a polarization experiment at 23 °C. In line with the electrochemical response, a localized type of attack can be clearly observed. Fig. 3.3a indicates the formation of several round shaped cavities of 20 μm to 50 μm of diameter. Some of them have a size lower than 10 μm. The smooth semispherical shape of the pit indicates a transport control of the dissolution process with an equalization of the metal dissolution kinetics (see the magnification in Fig. 3.3b). This is in line with the linear current-voltage relationship observed during the electrochemical experiments.

The oversaturation of corrosion products in the pits brings about the formation of a solid salt film, introducing a resistive barrier. Issacs /ISA 1973/ has calculated a resistivity of 10^8 ohm-cm from impedance measurements. The thickness of this layer is a function of the applied voltage and the diffusion rate of metal cations from the layer-solution interface.

The bottom of the pit reveals the grain structure of the steel. Some pits of 1 μm can be observed inside the large hollow, preferentially at the grain boundaries. Some corrosion products also appear to have been left behind during the pit growth (see white particles in Fig. 3.3b and c). Some of them seem to have dropped out from the observed small pits).

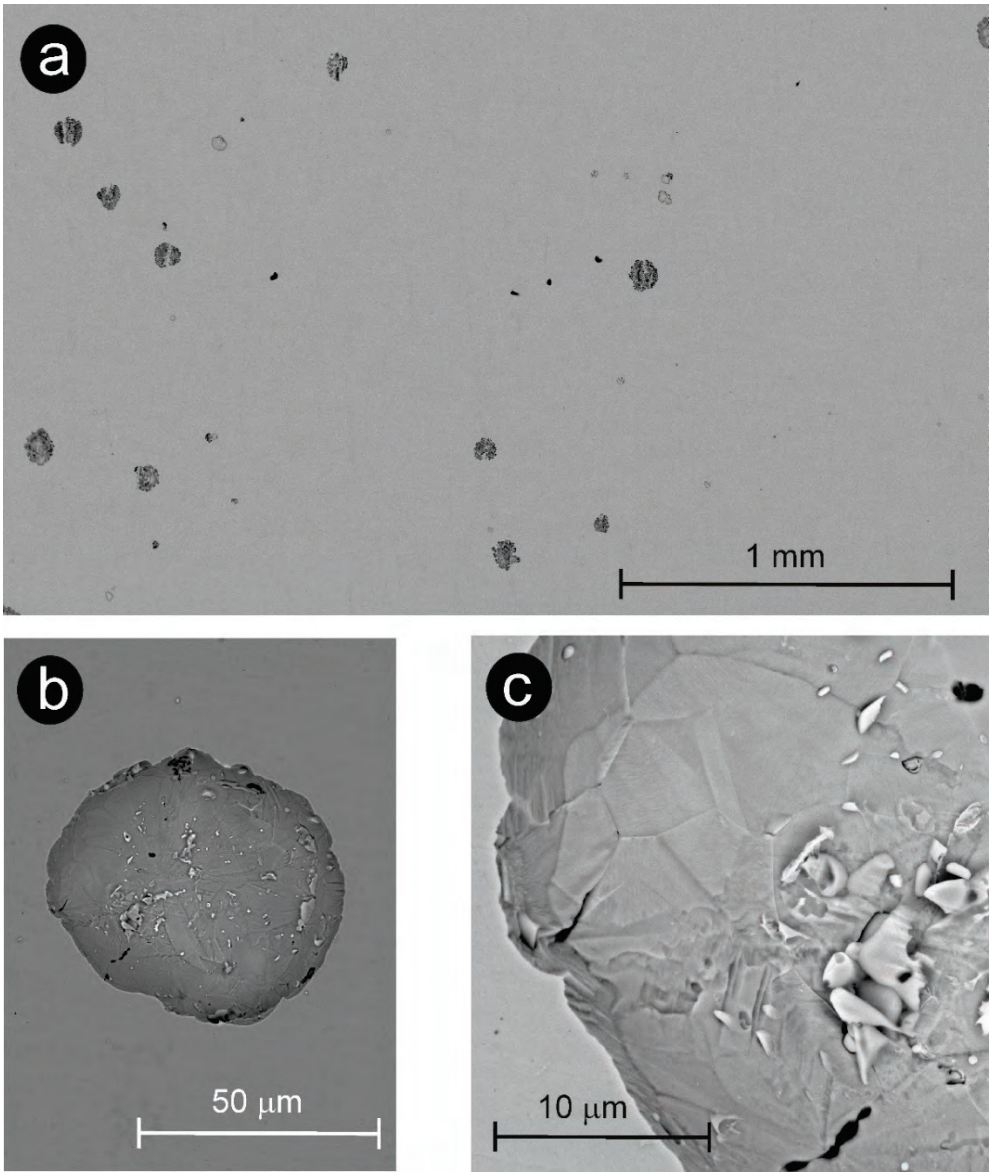

Fig. 3.3 SEM images in Z mode of steel 309S after cyclic polarization in Q3 solution at 23 °C and p = 6 bar

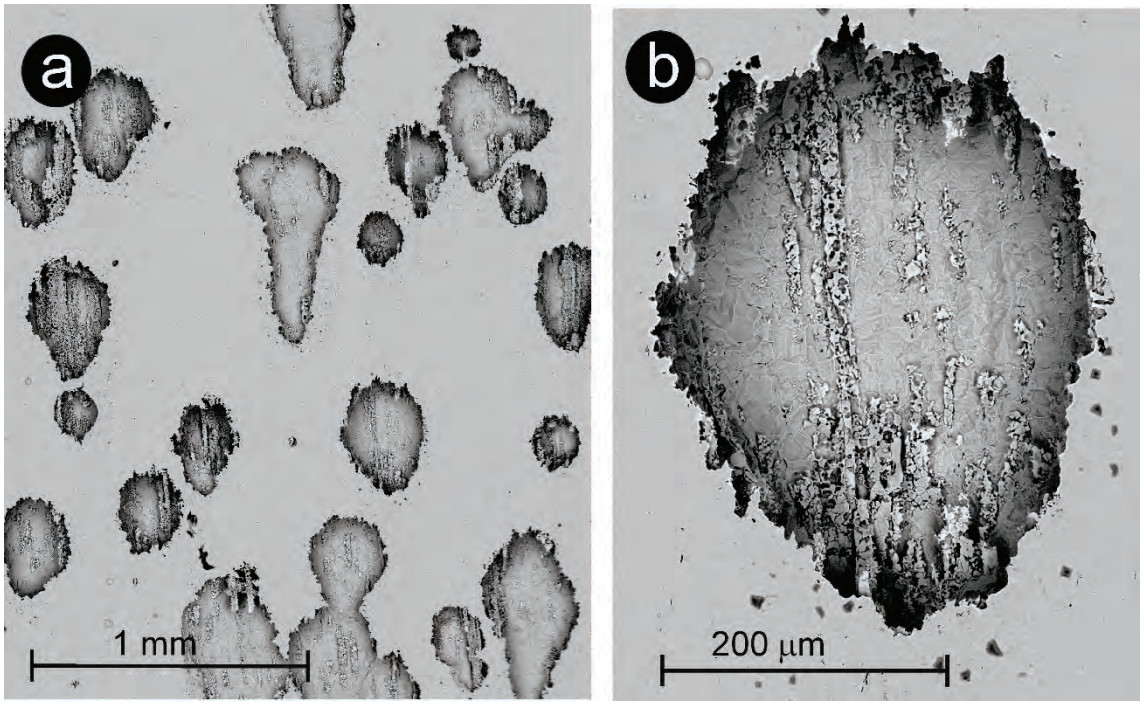

Fig. 3.4 SEM images in Z mode of steel 309S after cyclic polarization in Q3 solution at 23 °C and p = 6 bar

Fig. 3.4 shows a SEM image of the steel surface after a similar experiment as that presented in Fig. 3.1, where the pits have reached a more advanced growth stage with sizes of about 250 μm. The picture shows the surface in the same position as in the reactor. From the pit geometry, it can be inferred that after an initial radial growth, pits tend to advance vertically, probably induced by concentration gradients driven by gravity effects. The effect of the sample position on pit growth in austenitic steels was discussed by Mankowski and Szklarska-Smialowska /MAN 1975/, /MAN 1977/. Following the interpretation of these authors, the convective effects caused by the gravitational flow of corrosion products would reduce the thickness of the covering salt film with a consequence increase of current. The pit surface is characterized by stripes of a white appearance left behind the corroding front which can a priori be ascribed to an undissolved phase (see Fig. 3.4b).

The composition of the corroded surface was analyzed by EDX at different positions as indicated in Fig. 3.5. The spectra indicate that apart from the main components of the alloy Fe, Ni and Cr, also Si, Mo, Si and Mn are detected. It is worthy to note, that the small Lα Mo signal appears only at the precipitates with a Mo/Fe ratio 2.6 times higher than that in the bulk.

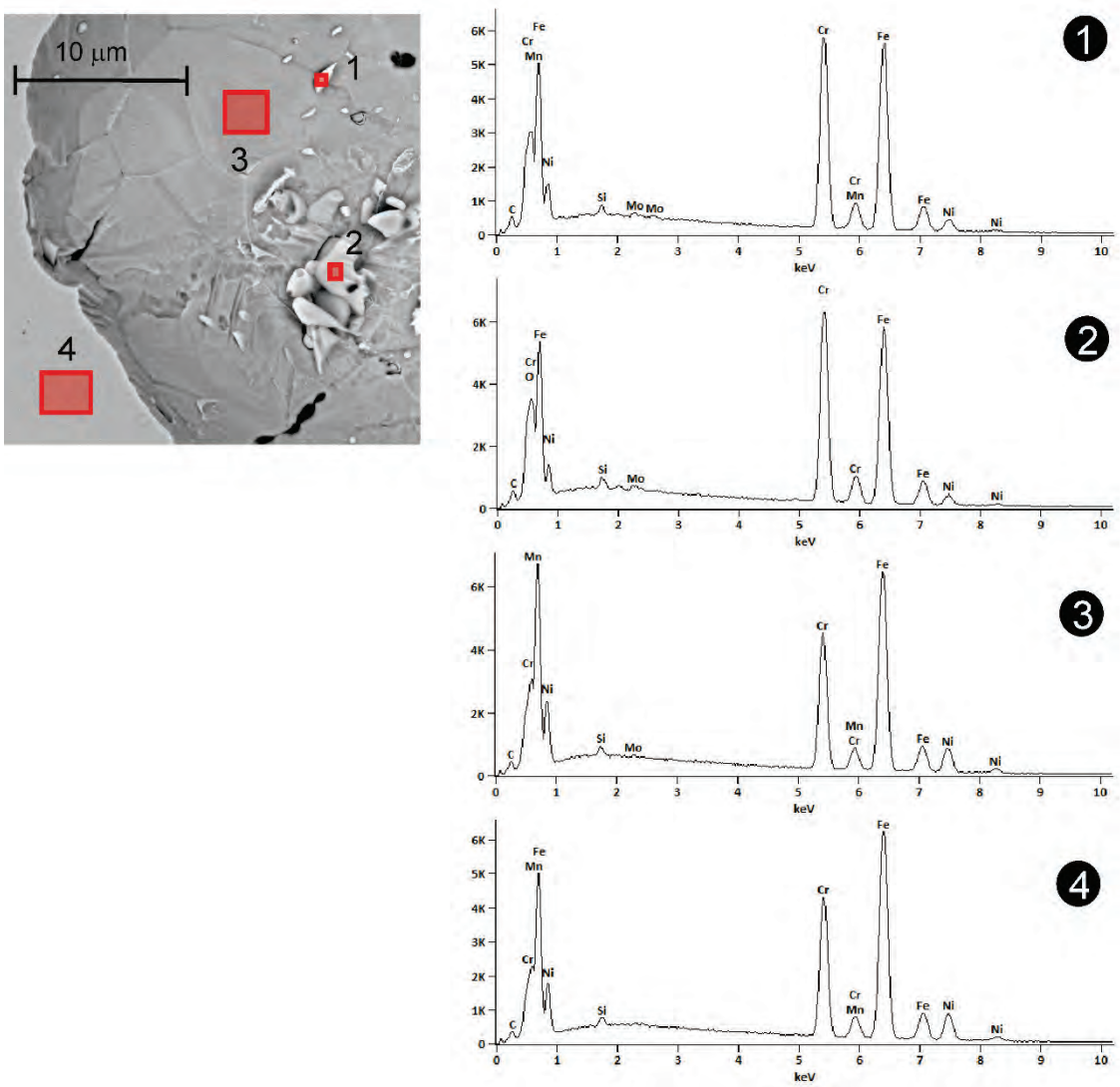

Fig. 3.5 EDX-chemical composition analysis of the 309S steel surface after cyclic polarization in Q3 solution at 23 °C and p = 6 bar

Tab. 3.1 shows the calculated elemental composition calculated from the EDX spectra for the different spots as indicated in Fig. 3.5. On the non-attacked surface (point 4), the element distribution is like that for the bulk (see Tab. 2.1), with atom % ratios Cr/Fe: 0.40 (0.38), Ni/Fe: 0.197 (0.201), Mn/Fe: 0.018 (0.019), Si/Fe: 0.012 (0.011)[1]. A composition comparable to that of the steel bulk is also measured at the bottom of the pit.

The observed carbon signal is comparatively large. The origin of carbon may be a contamination source or the accumulation of graphite during the dissolution of steel.

[1] Bulk values in parenthesis

There is, however, a clear difference between the carbon contents measured on the precipitated particles (point 1 and 2) and on the flat corroded and uncorroded surface (point 3 and 4, respectively). Presuming that the Ni signal in EDX spectra obtained on the particles arises from the underlying substrate, with the composition of point 3, one can calculate the following composition of particles: 24.61 at% of Fe, 21.30 at% of Cr. Thus, these particles can be ascribed to the intermetallic σ-phase.

Tab. 3.1 Surface elemental composition calculated from EDX-analysis shown in Fig**.** 3.5

% at	**C-Kα**	**Si-Kα**	**Cr-Kα**	**Mn-Kα**	**Fe-Kα**	**Ni-Kα**	**Mo-Lα**
point 1	12.9	0.7	31.2	0.6	49.3	4.8	0.2
point 2	14.0	0.9	31.8	-	48.3	4.3	0.3
point 3	9.6	0.8	22.9	0.9	54.8	10.6	0.1
point 4	9.1	0.6	22.3	1.	55.8	11.0	-
± % at	**C-Kα**	**Si-Kα**	**Cr-Kα**	**Mn-Kα**	**Fe-Kα**	**Ni-Kα**	**Mo-Lα**
point 1	±1.4	±0.2	±0.5	±0.2	±0.9	±0.7	±0.1
point 2	±0.9	±0.1	±0.5	-	±0.8	±0.7	±0.1
point 3	±0.8	±0.1	±0.5	±0.5	±0.9	±0.8	±0.1
point 4	±1.2	±0.2	±0.4	±0.2	±0.9	±0.9	-

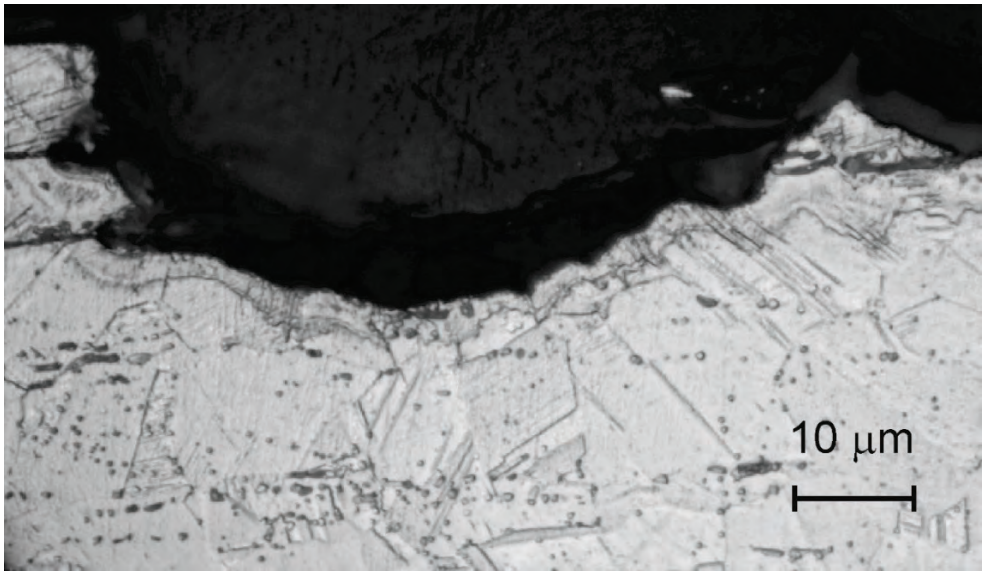

Fig. 3.6 Light microscopy picture showing a cross section view of a cut performed on a corroded sample. The cut surface was previously polished and etched with V2A solution (10:10:1 water, hydrochloric acid, nitric acid)

Fig. 3.6 shows a cross-section view of a cut obtained from a corroded sample following the cyclic polarization at 30 °C and p = 6 bar. The etching of the cut surface reveals the grain boundaries and segregated phases in the form of spheres and horizontal aligned intergranular ribbons. Intragranular straight stripes, revealing crystal twins can also be observed. The cross section clearly shows that the grain structure of the alloy does not exert any influence on the pit growth.

3.2 Localized corrosion at high temperatures and low pressures

The polarization experiments shown in Fig. 3.1 indicate a drastic change of the passive behavior of steel with increasing temperature. These changes in the corrosion mechanism are also reflected in the morphology of the attack. Fig. 3.7 shows the attacked surface after a cyclic polarization at 90 °C (voltammogram is not shown). Two types of morphologies can be distinguished. Like in samples corroded at 23 °C, spherical pits of 10 μm to 50 μm can be observed. Some of them reach a considerable depth, as suggested by their black appearance in the Z mode SEM image. The other morphology consists of vertically formed stripes of abraded metal. The corroded ribbons reveal the lamellar structure of the intermetallic phase.

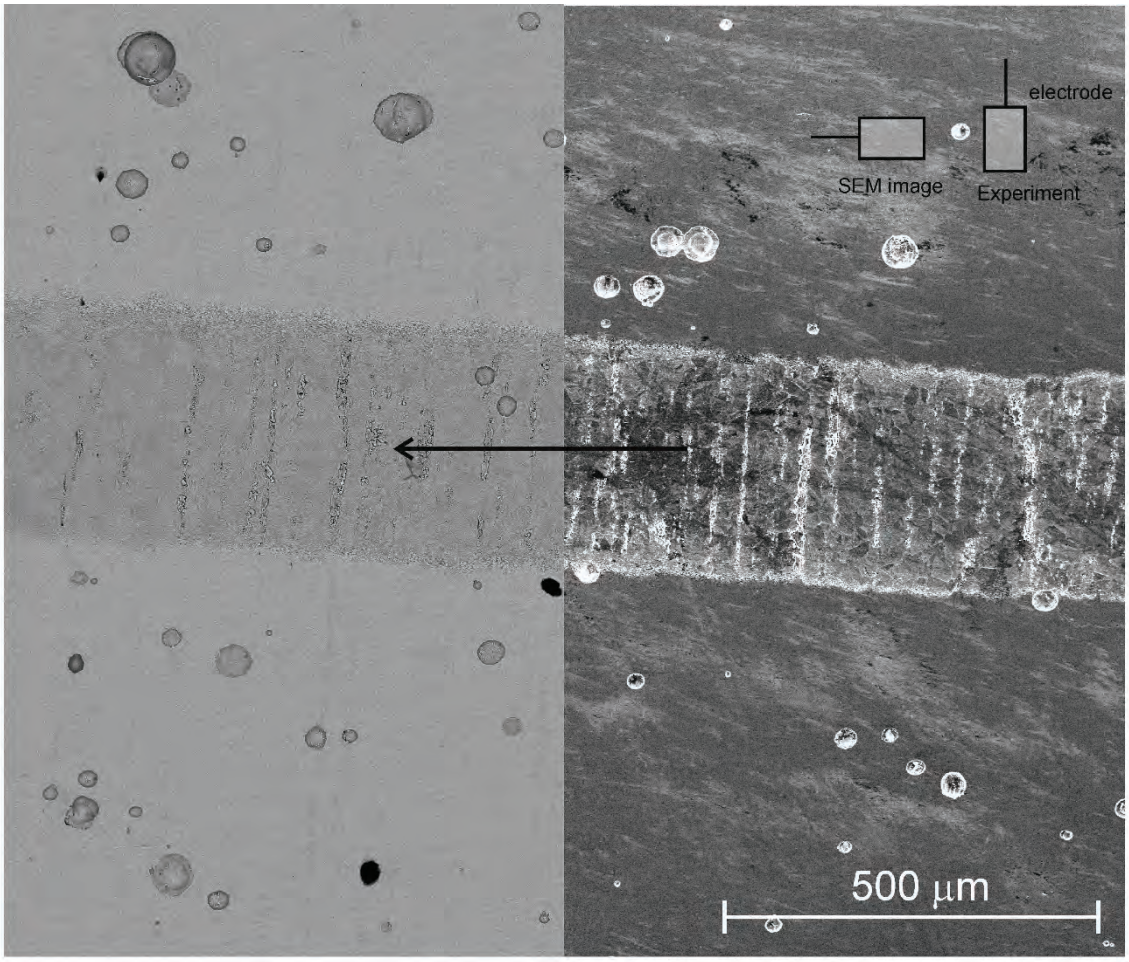

Fig. 3.7 SEM image of 309S steel surface after a cyclic polarization in Q3 solution at 90 °C and p = 5 bar**.** Left: backscattered electron image (material contrast), right: combined secondary electron and backscattered electron image (surface topography and material contrast). Arrow indicates the up-down direction of the electrode face during experiment (see scheme at the upper-right corner)

The SEM image on the right side of Fig. 3.7 (material contrast and surface topography) shows a patchily contrast outside the strong corroded areas (pits and pitted ribbons) indicating an inhomogeneous corrosion process.

The SEM image in Fig. 3.8a shows the transition of the morphology at the boundary of the corroded ribbon. From this, one can infer that the advance of the corrosion front initiates with a generalized localized attack. Pits nucleate preferentially at polishing scratches, creating a furrowed structure. On further corrosion, an equalization of dissolution rate leads to a homogeneous etching revealing the underlying grain structure.

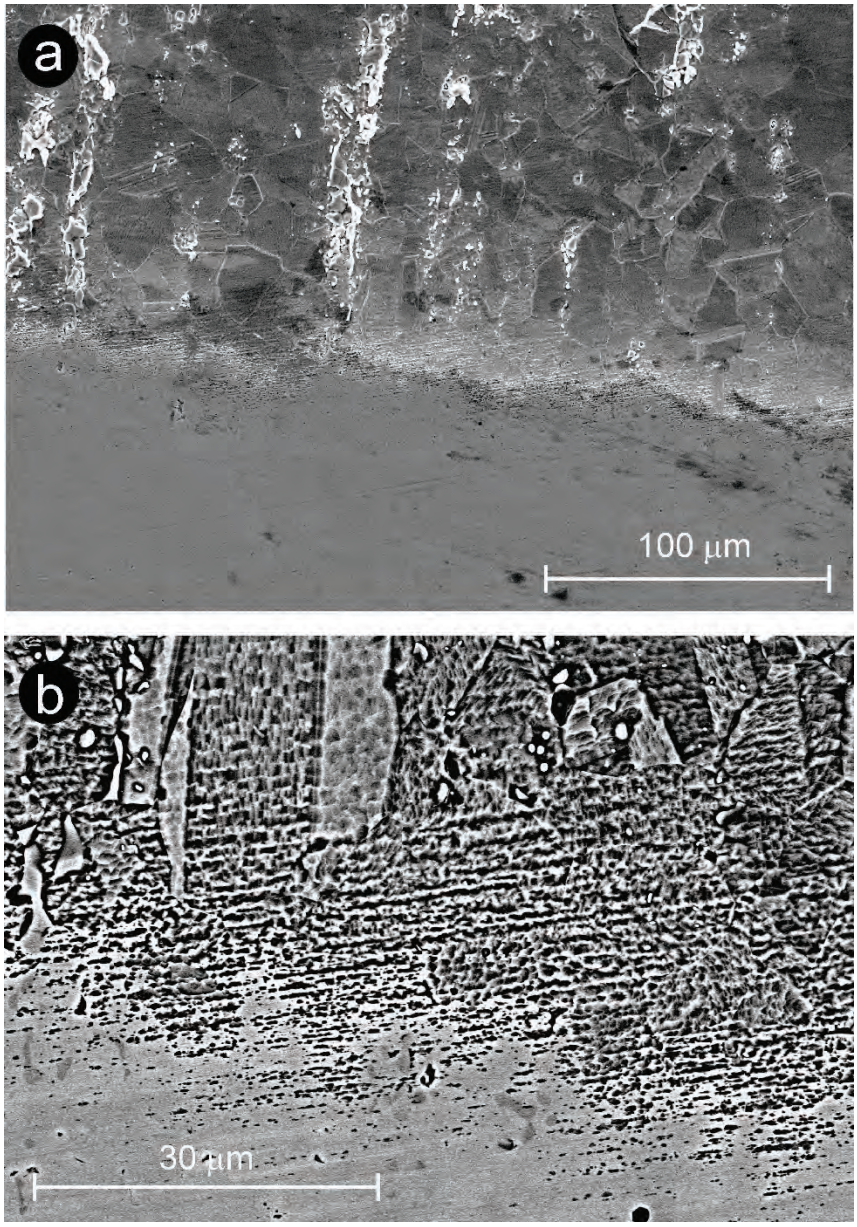

Fig. 3.8 SEM photographs depicting a magnification of the ribbon shaped corroded area of 309S steel in Q3 solution at 90 °C and p = 5 bar. a: combined material contrast and surface topography; b: material contrast

Fig. 3.9a shows a magnification of one of the pits imaged in Fig. 3.7. Unlike the etched substrate on the bottom of large pits formed at 23 °C, a rather porous morphology is observed here. It is still not clear, how such a structure can arise. A possible explanation may be a strong lateral fluctuation of the conductivity in the unstable salt film formed during dissolution. The elemental composition in the pit was investigated by EDX-

mapping. The results are shown in Fig. 3.10. The chemical mapping indicates an unexpected accumulation of carbon at the center and on the rim of the cavity.

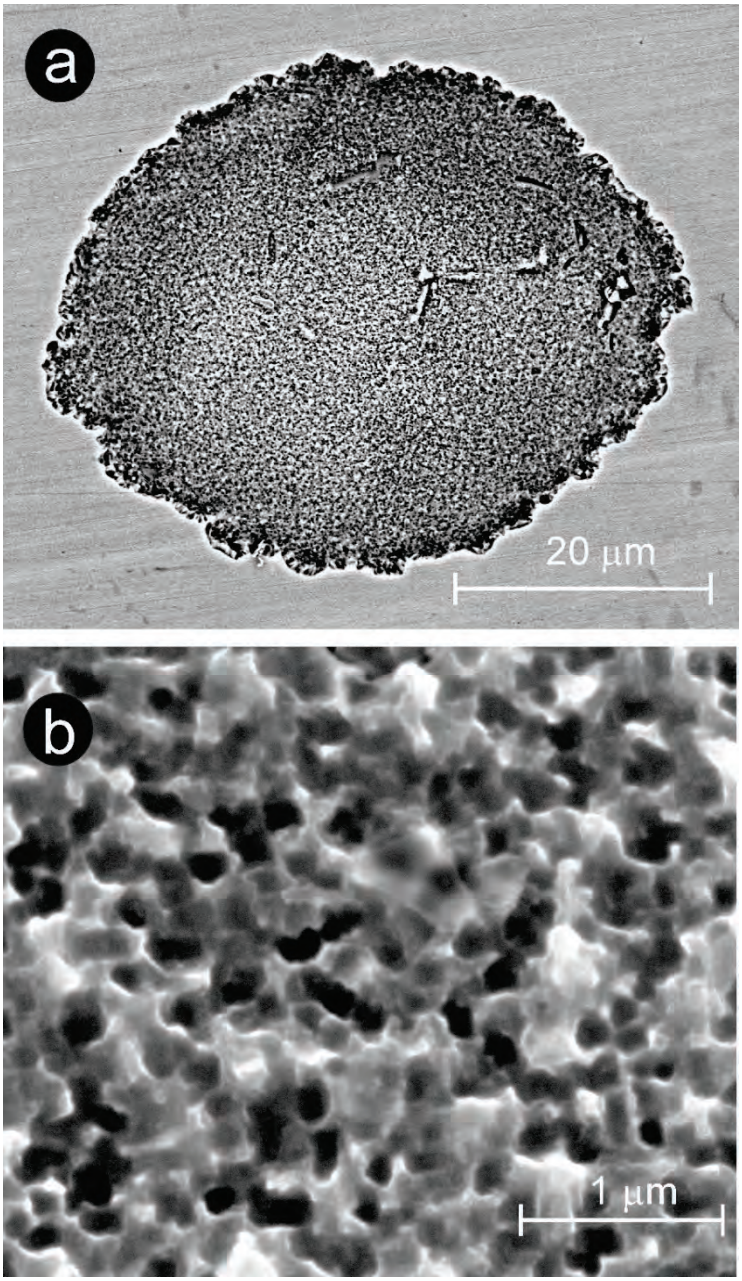

Fig. 3.9 SEM photographs depicting a magnification of pits at 309S steel surface after cycling polarization in Q3 solution at 90 °C and p = 5 bar. a: material contrast mode; b: combined mode

These areas match with a lower concentration of Fe, Cr and Ni, but keeping approximately the same relative concentrations as in the steel bulk. In addition, the higher carbon concentration spot in the middle of the pit correlates with the distribution of oxygen.

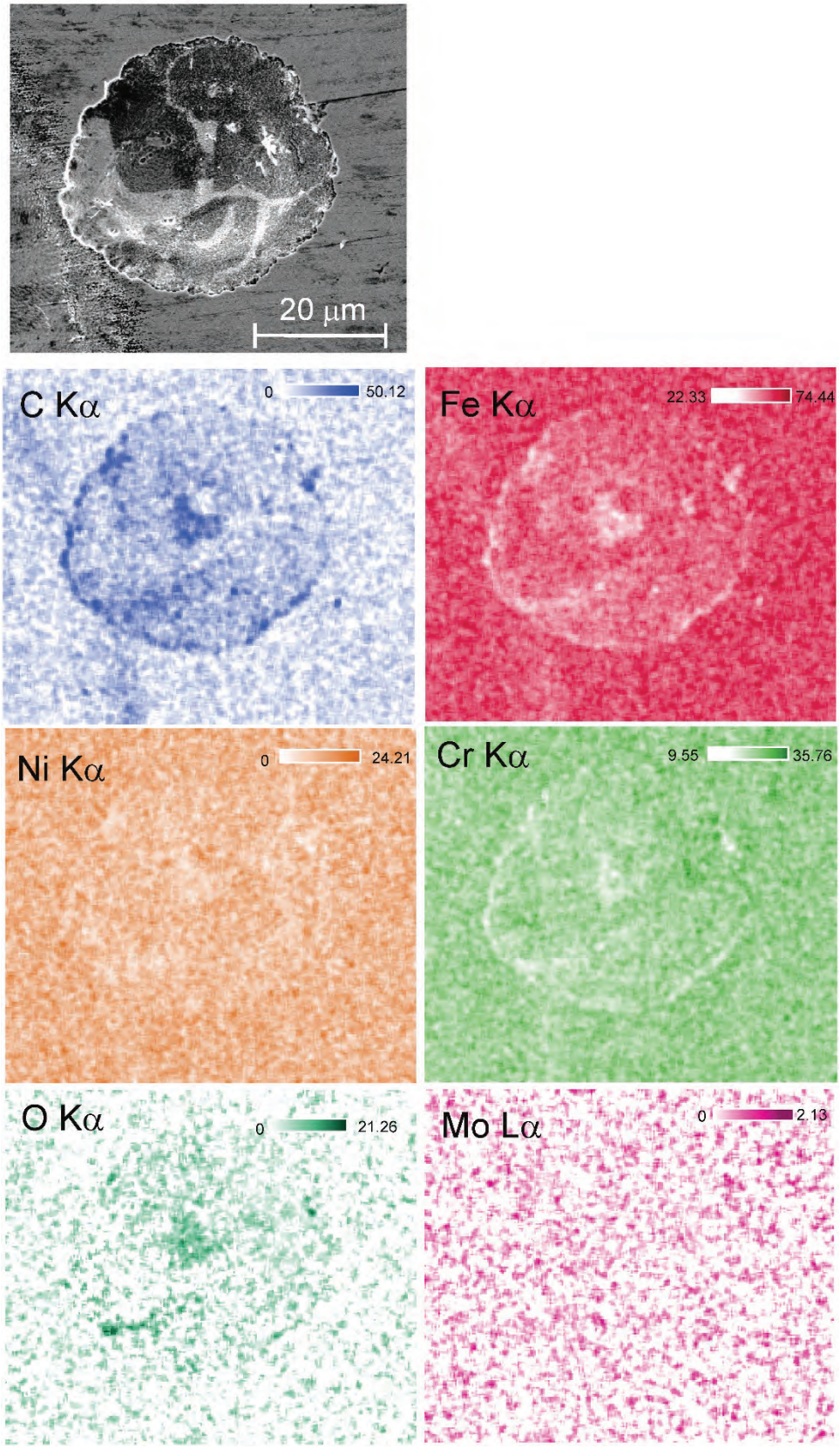

Fig. 3.10 EDX-mapping on a pit found after an anodic cyclic polarization of 309S steel in Q3 solution at 90 °C and 5 bar of pressure

Thus, it can be inferred that the accumulation of carbon is related to the formation of oxides, probably caused by its inclusion into growing hydroxide precipitates.

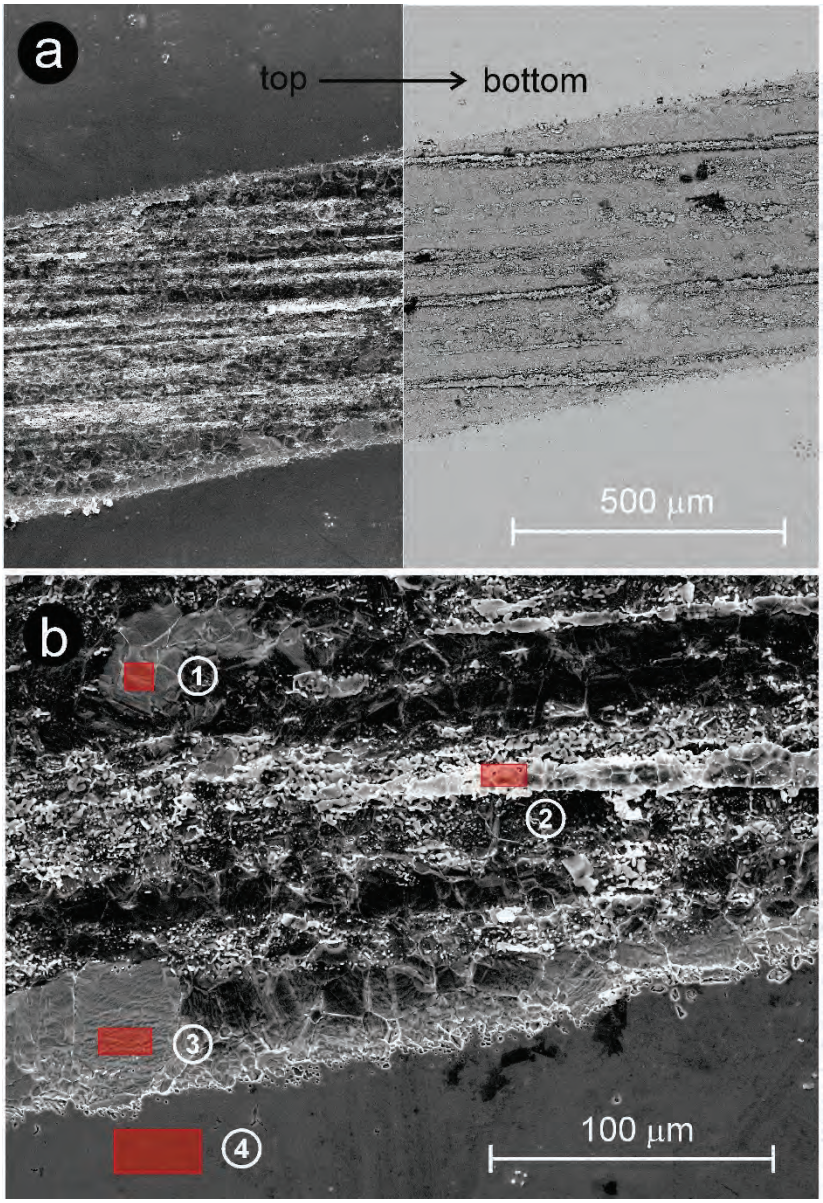

Fig. 3.11 a: SEM image of 309S steel surface after a cyclic polarization in Q3 solution at 80 °C and p = 5 bar. Left: combined ETD mode, right: material contrast. The position of the electrode during the experiment is indicated; b: magnification of the upper picture a) with indication of points of EDX analysis

Fig. 3.11a shows a SEM image of a ribbon type attack of the steel surface after a cyclic corrosion experiment at 80 °C. In this case, the revealed lamellar structure of the intermetallic phase is near parallel to the growth direction of the pit. The amount of corrosion products covering the attacked surface is larger than that on the ribbon shown in Fig. 3.7, where the intermetallic lamella appears perpendicular to the growth direction.

In Fig. 3.11b, the grain structure of the alloy is revealed in areas free of corrosion products. The EDX analysis performed in these areas (points 1 and 3) indicates an elemental composition like that of the bulk (see Tab. 3.2). As already remarked in the discussion of Fig. 3.10, a relative high concentration of carbon was here also found. It can be expected that fine particulate carbon released during dissolution remains adsorbed at the surface during the experiment. EDX analysis performed on the precipitates with a white appearance indicates a lower composition of Ni than that expected for the bulk of the alloy (%at 61.33 Fe, at% 25,36 Cr, at% 13.15 Ni and at% 0.14 Mo, in a FeNiCrMo basis). Assuming that the Ni signal arises from the underlying substrate, one can subtract the corresponding proportional amounts of Fe, Cr and Mo from the total composition and thus ratios of Cr/Fe: 0.855 and Mo/Fe: 0.014 for the precipitates can be obtained. This result supports the assumption of the formation of a Mo containing σ-phase. Note, that the large signal of oxygen appears at the point with a largest amount of carbon.

Tab. 3.2 Surface elemental composition calculated from EDX-analysis shown in Fig. 3.11

% at	C-Kα	O-Kα	Na-Kα	Si-Kα	P-Kα	S-Kα	Cl-Kα	K-Lα
point 1	11.5	-	-	0.8	-	0.3	-	-
point 2	18.8	6.4	0.8	0.7	0.3	-	0.2	0.1
point 3	9.4	-	-	0.7	-	-	-	-
point 4	8.9	-	-	0.7	-	-	-	-

Cr-Kα	Mn-Kα	Fe-Kα	Ni-Kα	Mo-Lα
21.3	1.3	53.6	11.3	-
26.8	0.6	40.9	3.9	0.4
22.1	1.2	55.1	11.5	-
22.9	0.9	55.5	10.9	-

A ribbon-type attack was observed at a temperature of 61 °C. Unlike surfaces corroded at 90 °C (see Fig. 3.7), a larger amount of corrosion products is left during the advance of the corroding front as shown in Fig. 3.12. The mapping pictures show a depletion of the alloy components inside the ribbon. Some elongated spots with the composition of the bulk indicate uncovered areas revealing the composition of the underlying substrate. The depletion of Fe, Cr and Ni inside the ribbon matches with an enrichment of O and Mo, suggesting the formation of oxides.

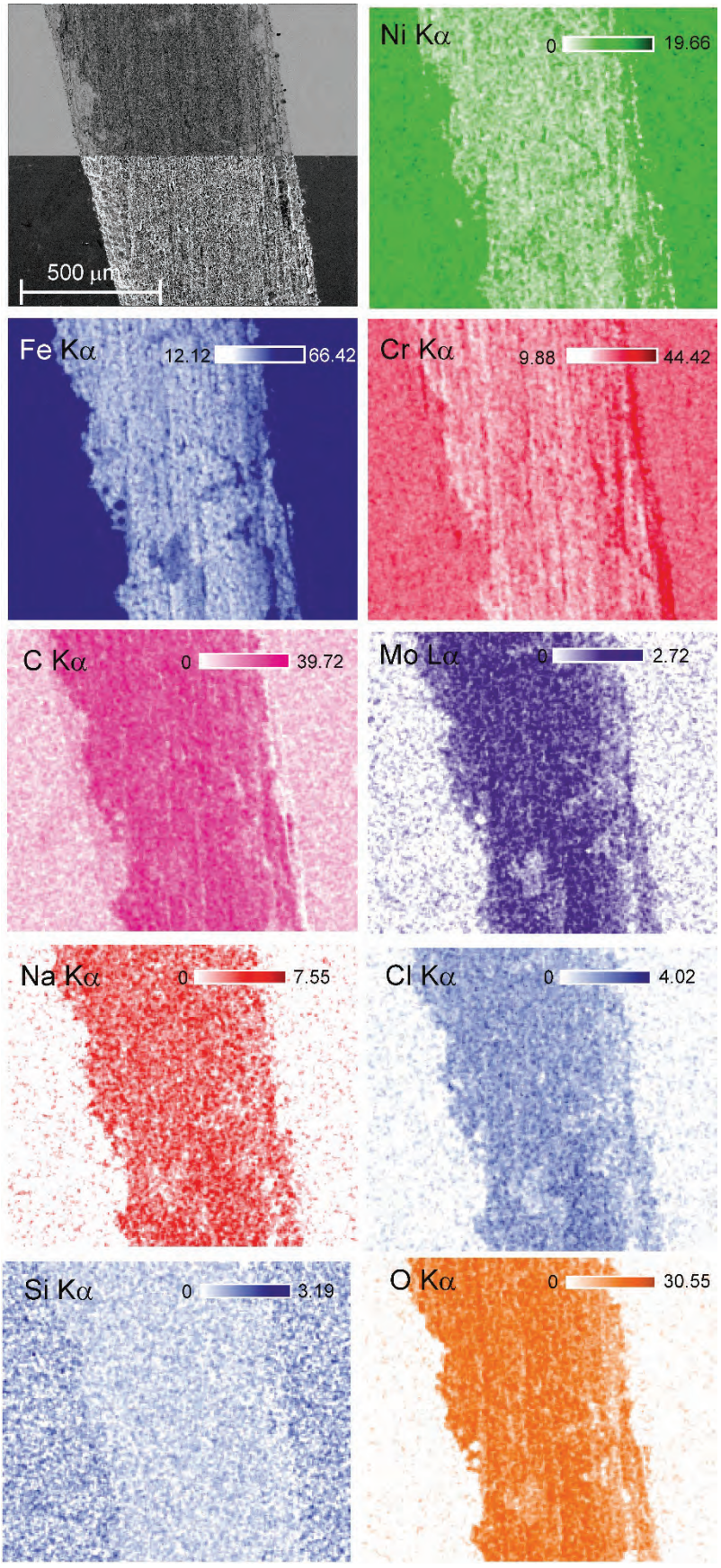

Fig. 3.12 EDX mapping analysis of a ribbon-type pit observed on 309S steel after a cyclic polarization in Q3 solution at 61 °C and p = 6 bar

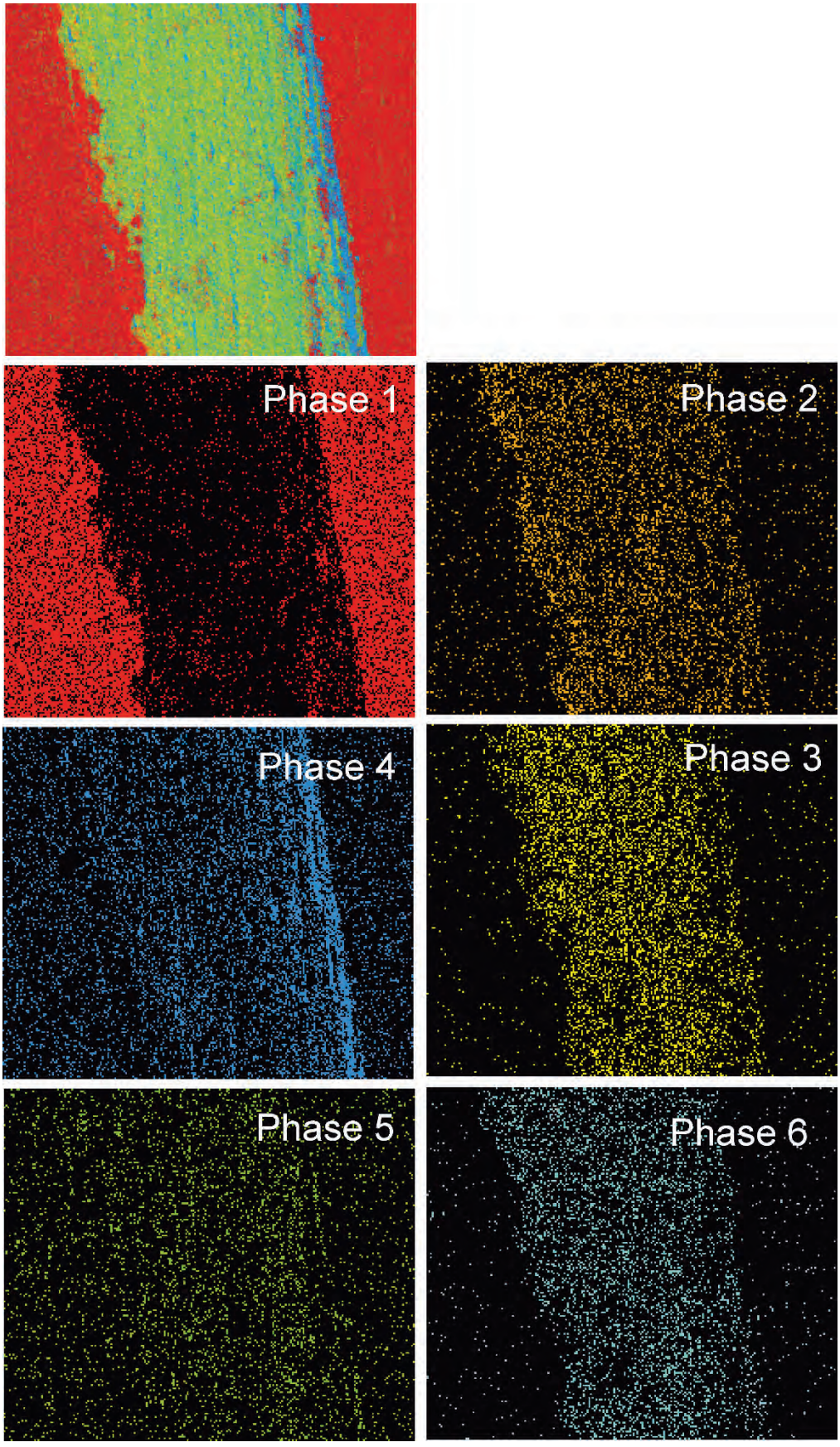

Fig. 3.13 Phase mode EDX mapping analysis of a ribbon-type localized attack after a cyclic polarization in Q3 solution at 61 °C and p = 6 bar

The analysis of the chemical composition in the mode of complementary phases of characteristic compositions can help throwing light on the understanding of the corrosion mechanism. Fig. 3.13 shows the result of such an analysis, where the total EDX signal was divided in six characteristic phases. The compositions are listed in Tab. 3.3.

Tab. 3.3 Elemental composition of a ribbon-type attack as a distribution of phases with different characteristic compositions derived from an EDX analysis. In brackets (area fraction)

	phase 1 (0.37)		**phase 2 (0.12)**		**phase 3 (0.12)**	
element line	**%at**	**± error**	**%at**	**± error**	**%at**	**± error**
C Kα	4.7	1.0	36.8	0.7	27.2	0.5
Si Kα	0.9	0.1	0.5	0.1	0.6	0.1
Cr Kα	22.6	0.1	13.6	0.1	18.7	0.1
Mn Kα	1.1	0.1	0.5	0.1	-	-
Fe Kα	58.8	0.3	22.3	0.2	21.6	0.2
Ni Kα	11.9	0.2	4.4	0.1	4.4	0.2
Mo Lα	-	-	0.8	0.1	2.5	0.1
O Kα	-	-	20.5	1.5	18.0	1.4
Cl Kα	-	-	0.7	0.1	1.7	0.1
Na Kα					1.5	0.1
P Kα					3.7	0.1
	phase 4 (0.20)		**phase 5 (0.09)**		**phase 6 (0.10)**	
element line	**%at**	**± error**	**%at**	**± error**	**%at**	**± error**
C Kα	9.6	0.2	17.8	0.9	24.7	0.5
Si Kα	0.4	0.1	0.7	0.1	0.4	0.1
Cr Kα	24.45	0.2	37.3	0.3	17.5	0.1
Mn Kα	1.2	0.1	-	-		0.1
Fe Kα	49.2	0.3	35.8	0.3	21.8	0.2
Ni Kα	8.5	0.2	2.7	0.2	4.0	0.2
Mo Lα	0.4	0.1	0.5	0.1	1.2	0.1
O Kα	5.2	0.1	3.5	0.5	17.2	0.3
Cl Kα	0.5	0.1	0.5	0.1	4.1	0.1
Na Kα	-	-	1.1	0.2	7.1	0.2
P Kα	0.5	0.1	-	-	1.7	0.1
Mg Kα	0.1	0.1	-	-	-	-

As one can see in Fig. 3.13, phases 2, 3 and 6 present a very similar pattern. They are characterized by a high concentration of C (at% 25 to 36) and O (around at% 20) and a low concentration of Ni (around at% 4). Phase 5 is characterized by a ration Fe/Cr: 0.96 and a low concentration of Mo and Ni. Thus, this phase seems to represent the distribution of released σ-phase. Phase 4, on the other hand, with ratios Fe/Cr: 2.01 and Fe/Ni: 5.76 shows an enrichment of Cr by dissolution of Fe and Ni (compare with bulk ratios Fe/Cr: 2.41 and Fe/Ni: 4.66)

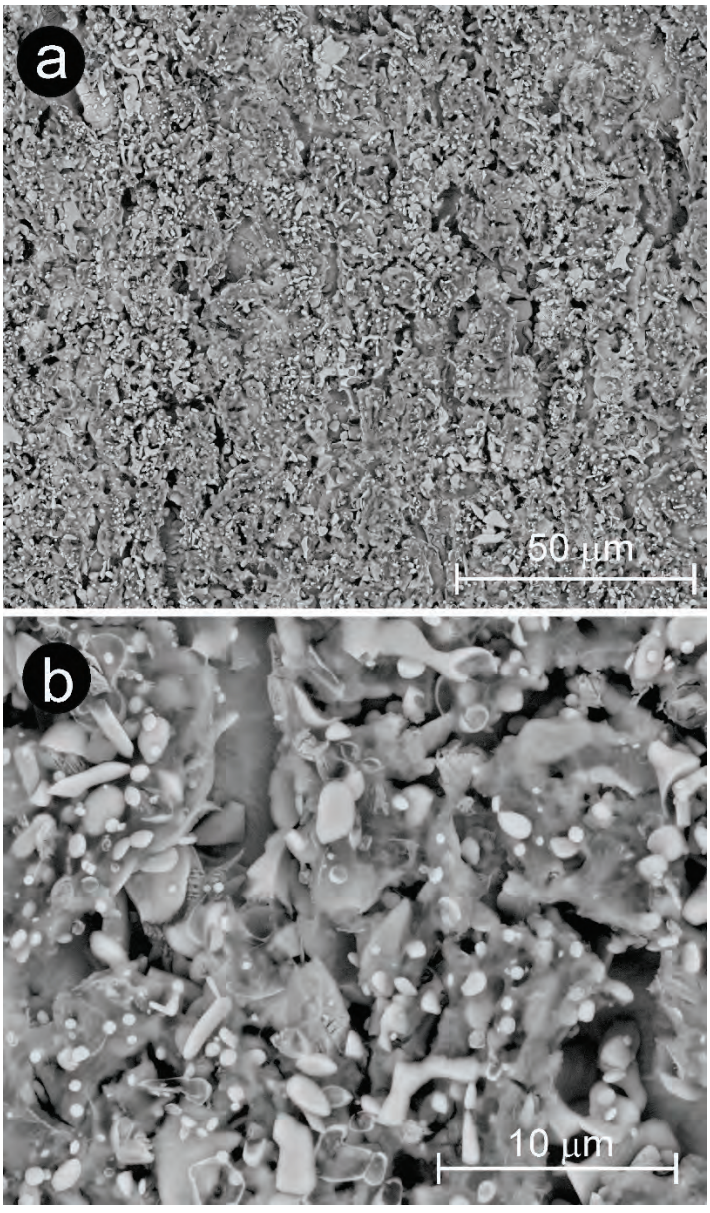

Fig. 3.14 SEM image of the center of a ribbon-type of attack of 309S steel surface after a cyclic polarization in Q3 solution at 61 °C and p = 5 bar with different magnifications

Fig. 3.14 shows the morphology of the attack inside a ribbon-type pit formed after the cyclic polarization in Q3 solution at 61 °C. A close analysis of the pictures let perceive a dispersion of different corrosion products deposited on the smoothly, due to the salt film controlled electro-dissolution, polished substrate. Under coarse, partially dissolved blocks, small spherical and stick like particles with a white appearance can be observed. In addition, peel- and dendrite-type deposits can also be distinguished.

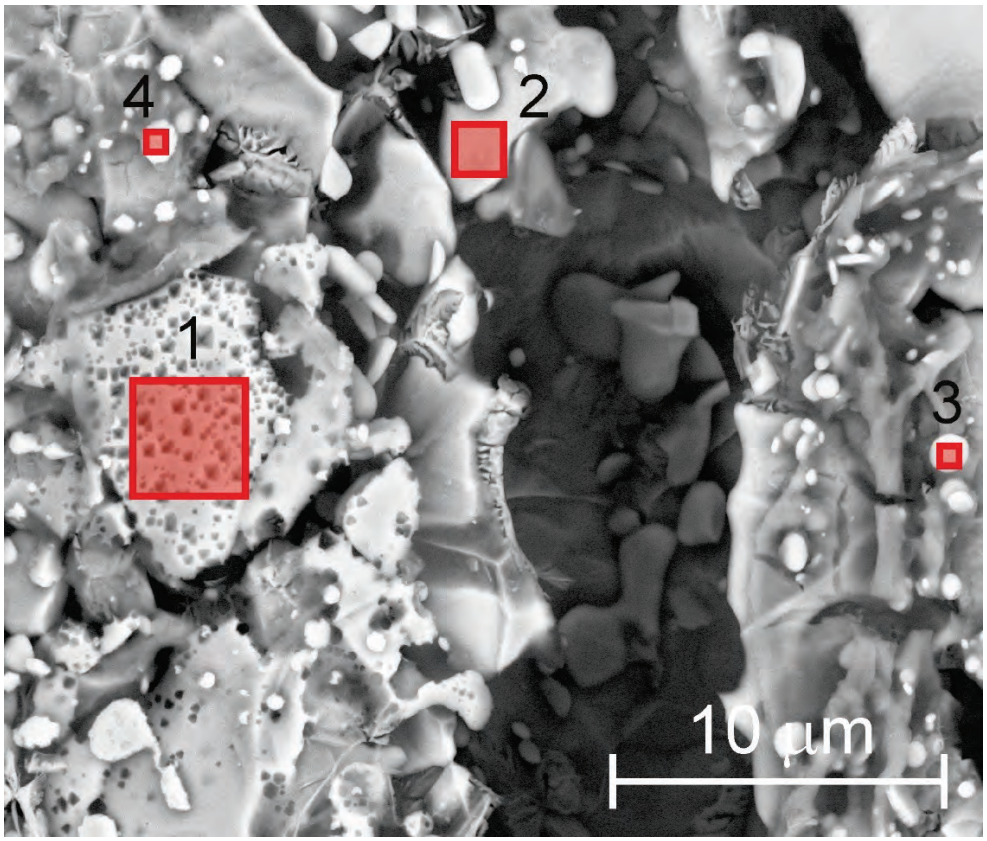

Fig. 3.15 SEM image of 309S steel surface after a cyclic polarization in Q3 solution at 61 °C and p = 5 bar with indication of points of EDX analysis

The elemental EDX analysis performed on some of the particles is shown in Tab. 3.4. Like the analysis shown in Fig. 3.12 and Fig. 3.13, a high percentage of C and O is observed. In this case, we could again assume that the Ni signal originates at the underlying substrate. On a Cr-Ni-Fe-Mo basis, amounts of at% Fe: 55.80, at% Cr: 38,00, at% Ni: 5.30 and at% Mo: 0.93 can be calculated for the analyzed particles. Accordingly, it is feasible to identify these products as ferrite /MCG 2008/.

Different types of dissolution mechanisms can be distinguished. The crystallographic attack of one of the particles, characterized by the formation of inverted pyramids, contrasts with the dissolution of homogeneous dissolution of other ones leaving a

dendrite of deposits. These later reveal an eutectic reaction during the fabrication process.

Tab. 3.4 Surface elemental composition calculated from EDX-analysis at the spots shown in Fig. 3.15

% at	C-Kα	O-Kα	Na-Kα	Si-Kα	P-Kα	Mg-Kα	Cl-Kα	Cr-Kα	Mn-Kα	Fe-Kα	Ni-Kα	Mo-Lα
point 1	15.8	8.5	1.8	0.5	0.7	0.2	0.6	27.4	0.7	39.2	3.8	0.6
point 2	16.2	7.6	1.2	0.7	0.7	0.2	0.5	27.2	-	40.5	4.0	0.5
point 3	22.5	10.8	1.4	0.6	0.9	0.2	0.4	23.7	0.5	34.8	3.3	0.6
point 4	18.1	11.0	1.7	0.7	1.3	0.2	0.9	25.2	-	36.3	3.6	0.9

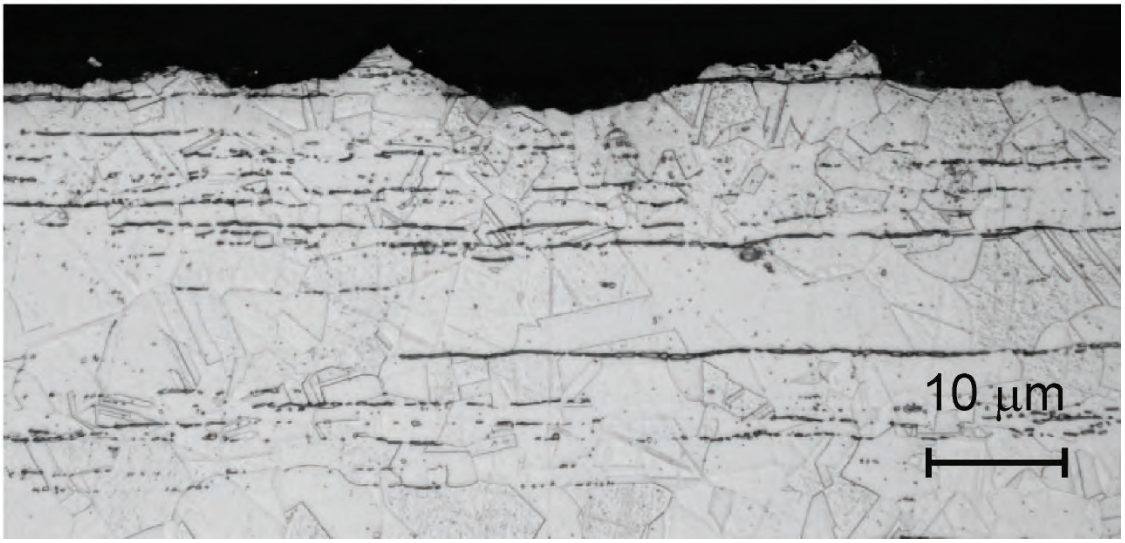

Fig. 3.16 Light microscopy picture showing a cross section view of a cut performed on a sample after a cyclic polarization at 80 °C and p = 5 bar in Q3 solution. The cut surface was previously polished and etched with V2A solution (10:10:1 water, hydrochloric acid, nitric acid)

As in the case of corrosion at low temperatures, the corrosion mechanism at 80 °C seems to be independent on the underlying metallographic structure of the steel as shown in Fig. 3.16. This picture underlines the more extended but lesser deep morphology of the attack.

3.3 Localized corrosion at high temperatures and high pressures

In order to investigate the influence of pressure on the corrosion of steel 309S, polarizations were carried out at different pressures and pre-heating programs. In all cases, the voltage scan was performed at 80 °C. The pre-heating ramp consisted in a stepwise increase of the control input in the feedback heating system from room temperature to the final experiment temperature at 5 bar. Due to the poor heat conductivity of the teflon lining in the cell, the temporal variation of the electrolyte temperature followed a damped oscillating course. The heating-up time for reaching 80 °C was approximately 3 h. For experiments at high pressure, the pressure was increased from 5 bar to 50 bar prior to the voltage scan.

At low pressure (p = 5 bar) the current-voltage curve does not show a passivation region and the anodic current initiates at about -0.3 V and increases following an exponential course (curves 1 and 2 in Fig. 3.17). This appears to be independent of a pre-heating program. The high pressure suppresses the initial exponential increase of the anodic current and sets a passive region until about -0.75 V without pre-heating (curves 3 and 4). The preheating process extends the passivation region. For instance, maintaining the sample at 80 °C during 3 h at the open circuit potential (OPC) and at 5 bar, increase the passive region up to 0.9 V when performing the polarization at 50 bar.

The mean corrosion potentials registered during 120 s prior to the voltage scan are listed in Tab. 3.5. These values do not show any visible correlation with the experiment conditions.

Tab. 3.5 Corrosion potentials measured prior to the voltage scan

Polarization	**1**	**2**	**3**	**4**	**5**	**6**
E_{corr} / V	-0.301	-0.266	-0.079	-0.165	-0.137	-0.213

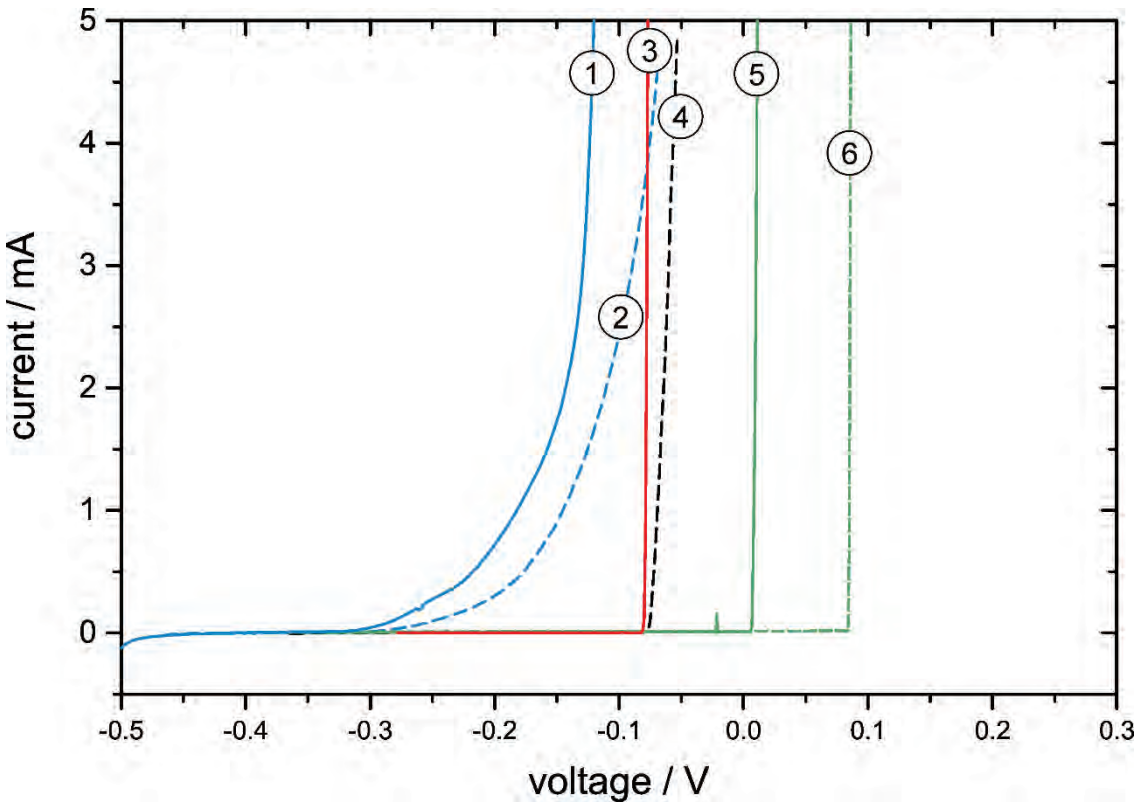

Fig. 3.17 Polarization curves performed on 309S steel in Q3 solution at 80 °C at different pressures and sample pre-heating programs. Scan rate:1 mV s^{-1}. 1: p = 5 bar without pre-heating[2]; 2: p = 5 bar with pre-heating ramp; 3 and 4: p = 50 bar without pre-heating; 5: p = 50 bar with pre-heating ramp; 6: p = 50 bar with pre-heating: 3 h at constant temperature of 80 °C

Fig. 3.18 shows SEM images of the surface after the anodic polarization 1. Despite the lack of a passive current-voltage course, the surface shows a localized type of attack. Rounded shallow pits revealing the grain structure of steel with sizes of 10 μ to 100 μm can be observed. Rounded particles and tree-like deposits are dispersed inside the pit. Tab. 3.6 shows the elemental composition calculated by EDX at different positions inside and outside the pit. As already discussed in 3.2, the amount of Fe and Cr given by the signal arising from the substrate can be subtracted from the total amount using Ni signal as a reference. Thus, ratios of Cr/Ni: 0.925 and of Cr/Mo: 31.40 can be obtained. This suggests that these white appearing deposits correspond to σ-phase. A light enrichment of Cr and Mo is observed at the bottom of the pit.

[2] The sample was immersed in the solution previously heated until the experiment temperature.

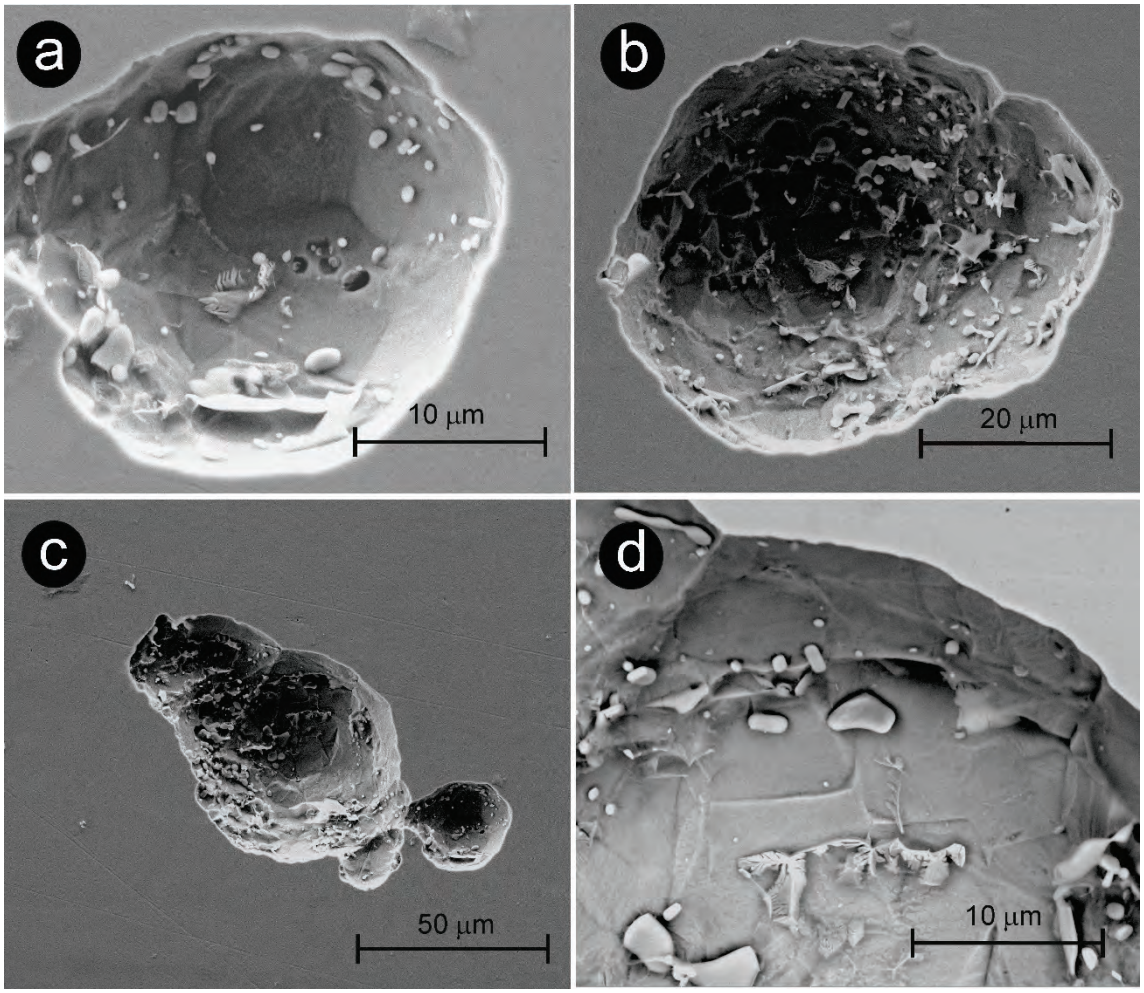

Fig. 3.18 SEM images of the 309S steel surface after the polarization 2 (see Fig. 3.17). a,b,c: secondary electron mode (SE); d: height mode (Z)

Tab. 3.7 shows the elemental composition of a tree-like deposit. It is worthy to note the enhanced concentration of Cr and Mo with a ratio Cr/Fe: 1.42 and Cr/Mo: 69.4. This result lets infer that the white appearing particles underwent a eutectic reaction leaving a Cr-rich core encased by a Fe-rich CrFeNi alloy. The high acidic conditions generated inside the pit should favor the dissolution of this particles during the anodic voltage scan.

Fig. 3.19 shows a SEM image of the surface of 309S steel after the anodic polarization at 80 °C and 50 bar of pressure (indicated as (6) in Fig. 3.17). The current-voltage curve (see Fig. 3.17) shows that under these conditions, a passive region appears. The breakdown of passivity is manifested in a rapid radial expansion of the corroding, probably originated in an oxide defect.

Magnifications of different sites of attacked surface are displayed in Fig. 3.20. Fig. 3.20a indicates that the spreading of the attacked area starts with nucleation of pits, whose density increases with the advance of corrosion process.

Tab. 3.6 Surface elemental composition (at %) at different sites on the corroded area of 309S after the anodic polarization in Q3 solution at 80 °C and 5 bar, obtained by EDX

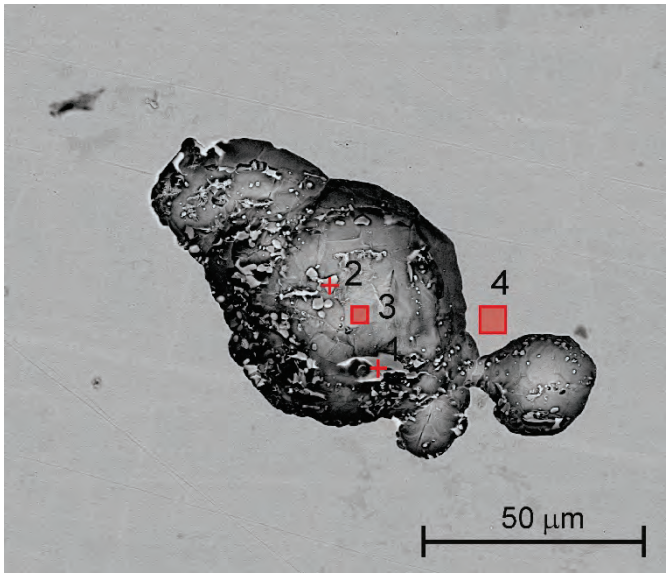

element	C-Kα	O-Kα	Si-Kα	P-Kα	Cr-Kα	Mn-Kα	Fe-Kα	Ni-Kα	Mo-Lα
point 1	19.6 ±2.8	-	0.9 ±0.4	0.5 ±0.2	28.2 ±0.9	1.1 ±0.5	45.2 ±1.5	4.2 ±1.2	0.4 ±0.1
point 2	7.6 ±0.7	2.8 ±0.7	0.4 ±0.1	0.4 ±0.1	34.0 ±0.7	0.9 ±0.4	49.1 ±1.2	4.4 ±0.5	0.3 ±0.1
point 3	8.1 ±1.0	-	-	-	25.8 ±1.0	1.8 ±0.6	55.5 ±1.8	8.5 ±1.4	0.2 ±0.1
point 4	9.4 ±1.7	-	0.7 ±0.1	-	22.7 ±0.6	1.0 ±0.3	55.9 ±1.2	10.3 ±1.0	-

The geometrical forms of the pits point out the crystallographic nature of the attack. This is an indication of the acidification process taking place at the corroding front. The coalescence of the growing pits (see Fig. 3.20e) evolves to a kinetic controlled dissolution of grains revealing the distinct crystal orientations (see Fig. 3.20b, d and f). In Fig. 3.20d, pits with a remarkable size can be distinguished. It can be supposed that these sites are left after the detachment of second phase particles, visible at the right side of the picture. The removal of second phases, in this case the ferrite phases, during corrosion leaves a characteristic imprint, as shown in the metallographic analysis depicted in Fig. 3.6., i. e. elongated baston-like channels and rows of spherical holes.

Tab. 3.7 Surface elemental composition of a tree-like deposit on the corroded area of 309S steel after anodic polarization in Q3 solution at 80 °C and 5 bar after, obtained by EDX

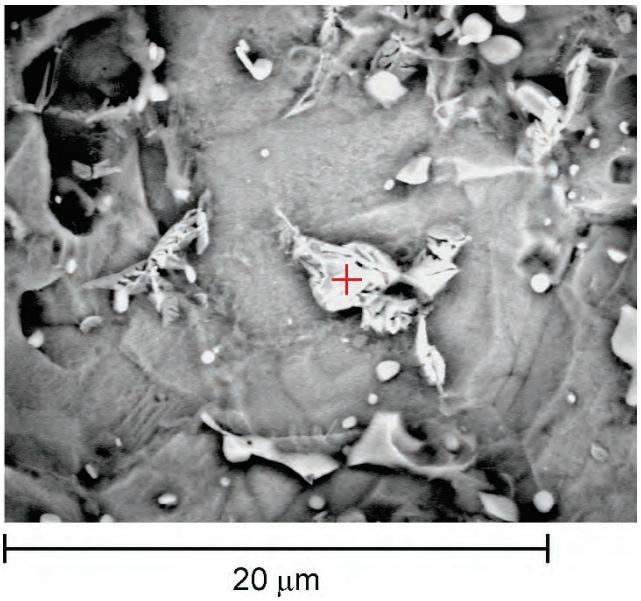

C-Kα	O-Kα	Si-Kα	P-Kα	Cl-Kα	Cr-Kα	Fe-Kα	Ni-Kα	Mo-Lα
28.7±1.4	7.3±1.6	0.4 ±0.1	0.6 ±0.1	0.2 ±0.1	34.7±0.8	24.4±1.0	3.4±0.8	0.5±0.1

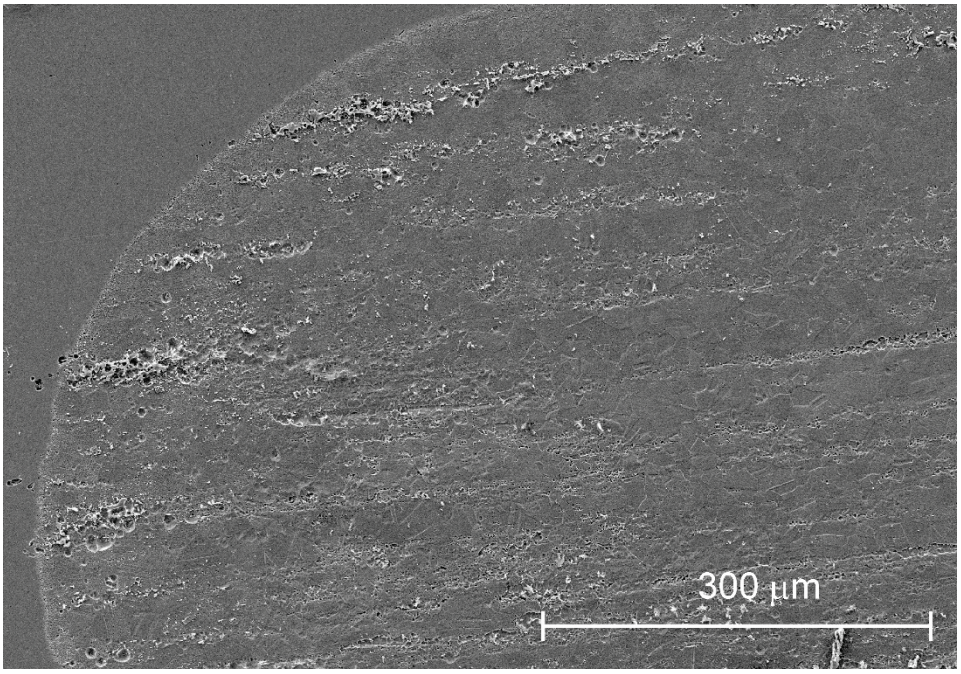

Fig. 3.19 SEM image of the 309S steel surface after the polarization number 6 (see Fig. 3.17): secondary electron mode (SE)

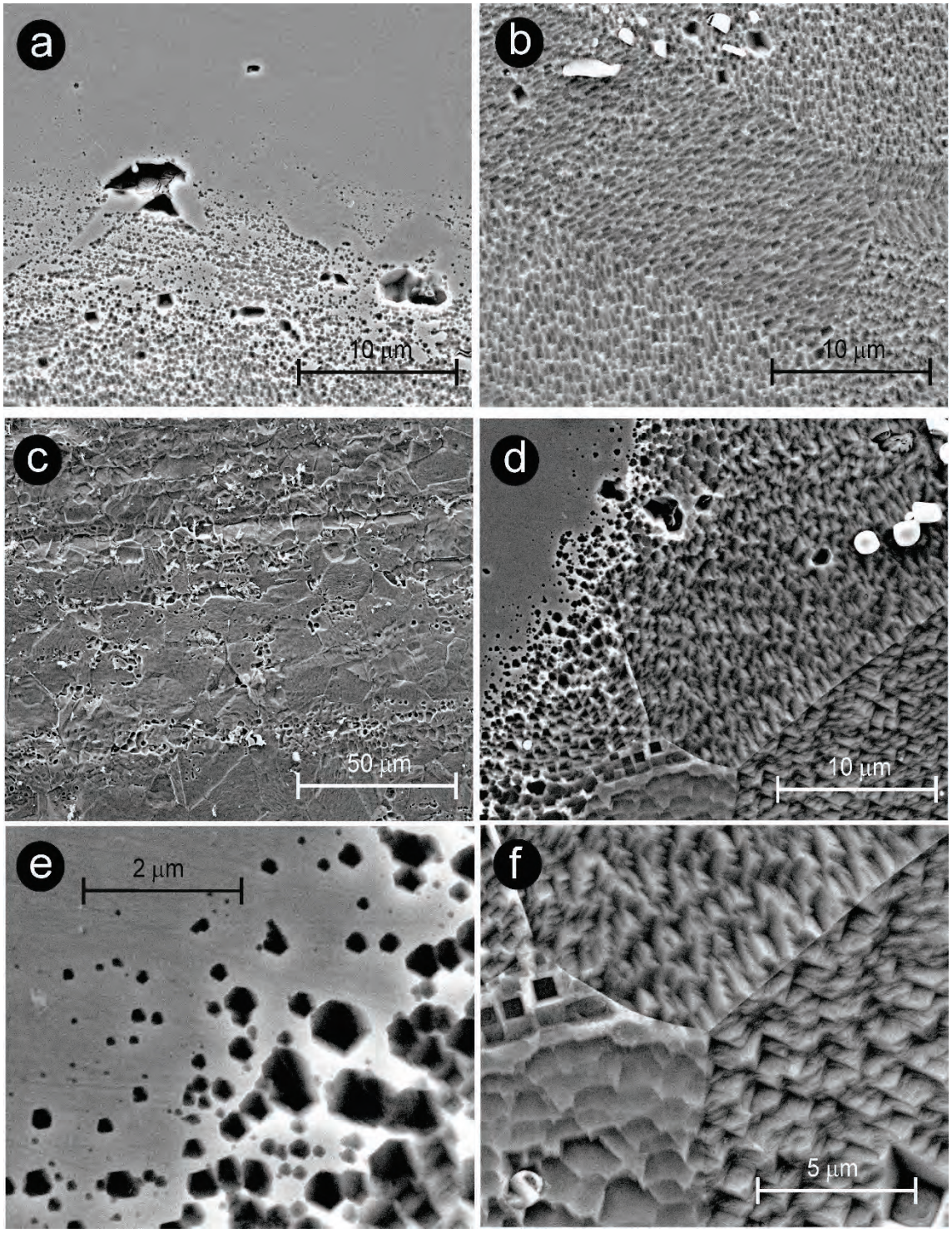

Fig. 3.20 SEM images of the 309S steel surface after the polarization 6 (see Fig. 3.17): secondary electron mode

4 Corrosion of 309S steel in Q2 solutions

In a first attempt to obtain information about the corrosion behavior of steel 309S in Q2 solution, current-voltage experiments were performed, and the results are shown in Fig. 4.1. In the first cycle an almost exponential increase of the anodic current is observed at V > -0.4 V. Considerable current noise is present in the first cycle. The reverse scan shows practically no hysteresis, indicating a rather generalized surface attack. The second and third cycles show a reduction of the current noise and a shift of the anodic curve towards more positive potentials, suggesting some kind of stabilization of the dissolution process.

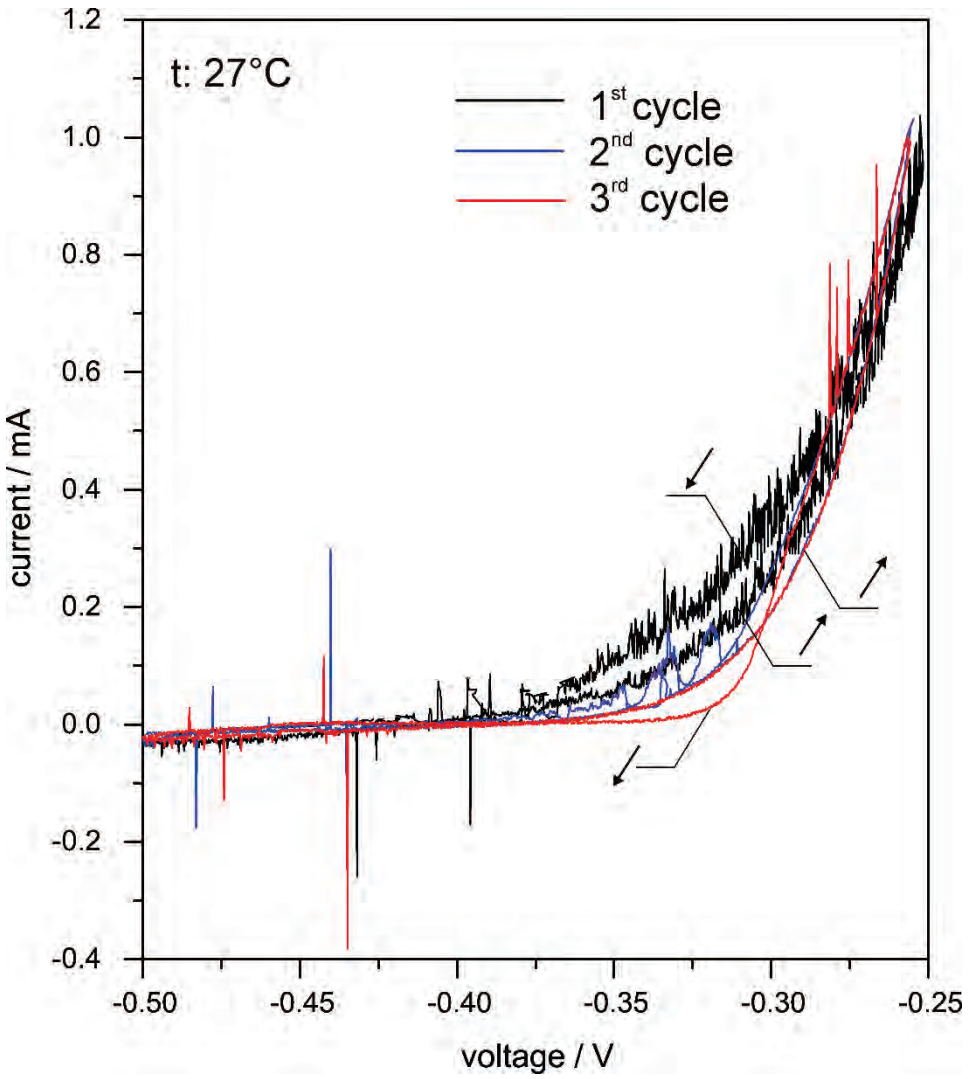

Fig. 4.1 Cyclic current-voltage curves of 309S steel in Q2 solution at 27 °C. Scan rate: 1 mV s^{-1}. Polarization were started at -0.2 V from the OCP. Arrows indicate the scan direction

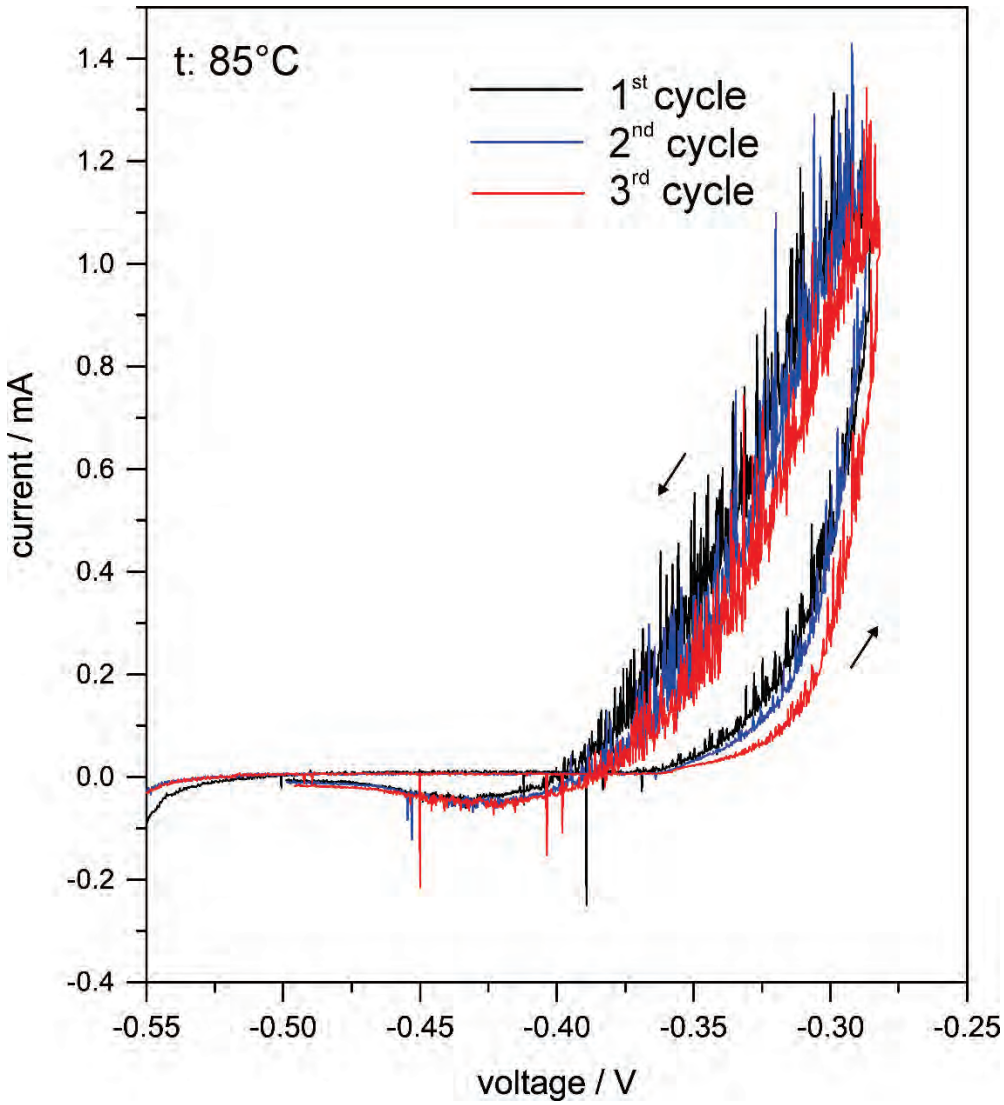

Fig. 4.2 Cyclic current-voltage curves of 309S steel in Q2 solution at 85 °C. Scan rate: 1 mV s^{-1}. Polarization were started at -0.2 V from the OCP. Arrows indicate the scan direction

The anodic behavior of the steel changes considerably at 85 °C as shown in Fig. 4.2. The anodic current increases at V > -0.37 V in the forward scan. Unlike the curves at 27 °C, a large current noise appears in the reverse scan. Here, practically no current stabilization with successive scans is visible. Also, a large hysteresis is observed. The reverse scan shows a cathodic peak at the end of the cycle, indicating a deposition process.

The surface morphology after the attack generated by the cyclic scans at 27 °C is shown in Fig. 4.3. The picture (a) shows the formation of homogeneously distributed round pits and the formation of much larger chained-like pits, as shown with more details in the magnification shown in picture (b).

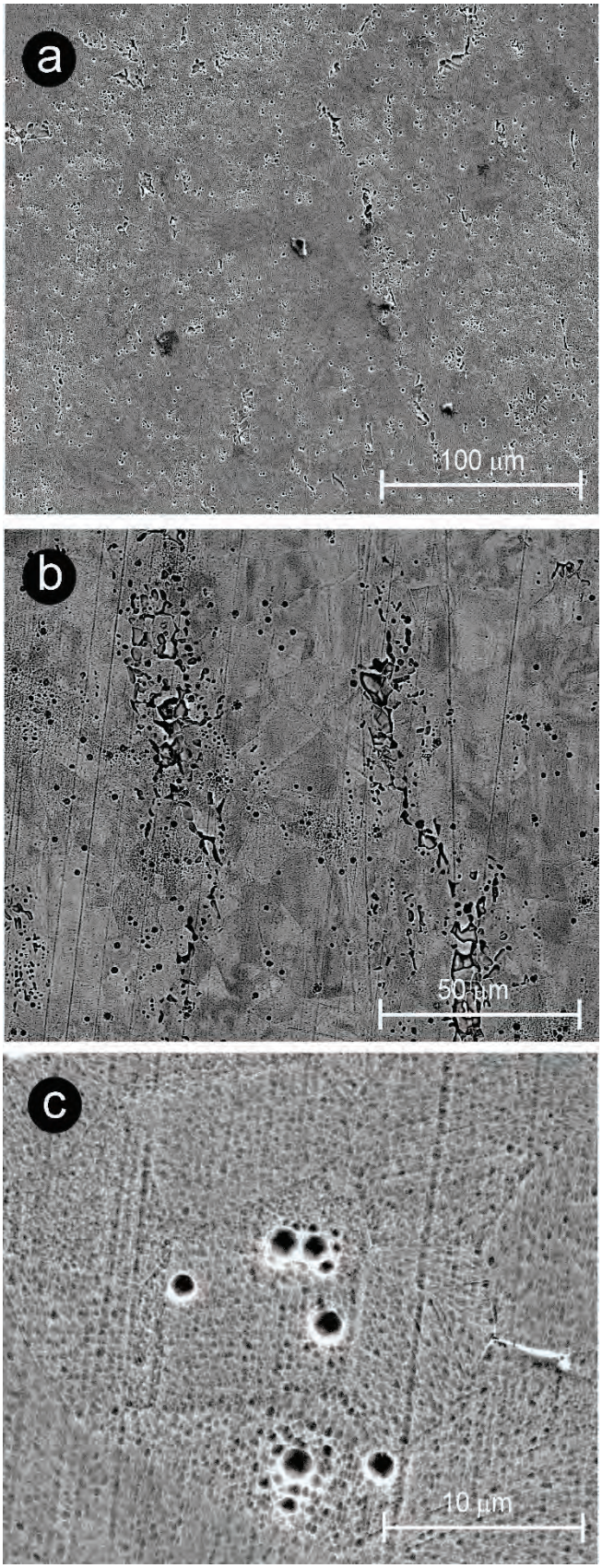

Fig. 4.3 SEM (secondary electron mode) pictures of the surface of 309S steel after the cyclic current-voltage experiment shown in Fig. 4.1

The magnification shown in picture (c) shows that the formation of pits is accompanied by a homogeneous corrosion revealing the grain structure of the steel. The attack does not seem to be crystallographic. The dissolution leaves a sponge-like structure. A closer look at the rounded pits shown in picture (c) suggests that these arise from an advanced growth of some of the small hollows constituting the surface pattern of the dissolving grain surface. The larger chain-like pits are certainly left after a stronger attack of boundaries of ferrite segregations.

Tab. 4.1 Surface elemental composition (at %) at different sites on the corroded area of 309S after the cyclic polarization in Q2 solution at 27°C, obtained by EDX

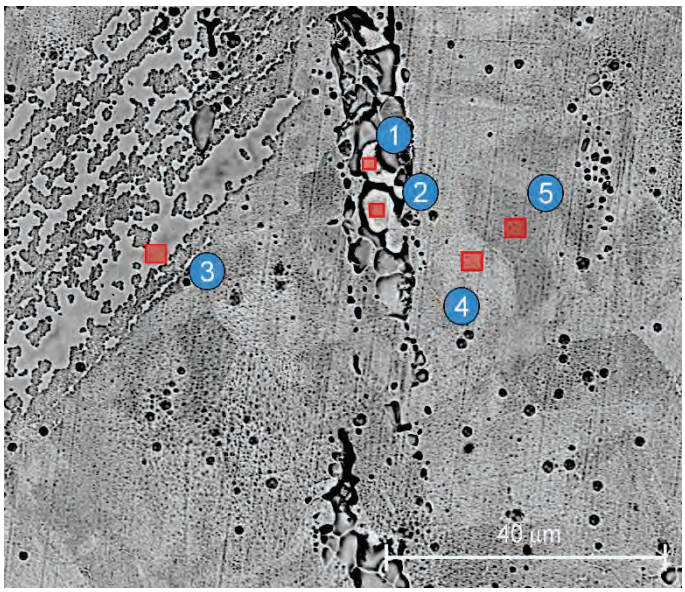

element	C-Kα	Si-Kα	**Cr-Kα**	Mn-Kα	**Fe-Kα**	**Ni-Kα**	Mo-Lα
point 1	14.8 ±0.8	0.9 ±0.1	**21.1 ±0.3**	0.9 ±0.3	**51.5 ±0.6**	**10.1 ±0.5**	0.2 ±0.1
point 2	8.6 ±0.9	0.8 ±0.1	**23.0 ±0.3**	1.0 ±0.4	**55.9 ±0.7**	**10.6 ±0.6**	0.2 ±0.1
point 3	20.9 ±0.8	0.6 ±0.1	**19.4 ±0.3**	0.9 ±0.3	**48.3 ±0.6**	**9.7 ±0.5**	0.1 ±0.0
point 4	8.5 ±0.8	0.7 ±0.1	**22.6 ±0.3**	1.2 ±0.2	**56.0 ±0.7**	**10.8 ±0.6**	0.2 ±0.1
point 5	8.7 ±0.9	0.8 ±0.1	**22.7 ±0.3**	1.1 ±0.2	**55.9 ±0.7**	**10.7 ±0.6**	0.1 ±0.1

The EDX analysis shown in Tab. 4.1 indicates that there are no considerable differences in the elemental composition at different characteristic sites of the corroded surface. The relative concentration of the main alloy components Cr, Fe and Ni remains practically the same and it is close to that of bulk. It is interesting to note, that different levels of carbon accumulation are measured at the different characteristic sites.

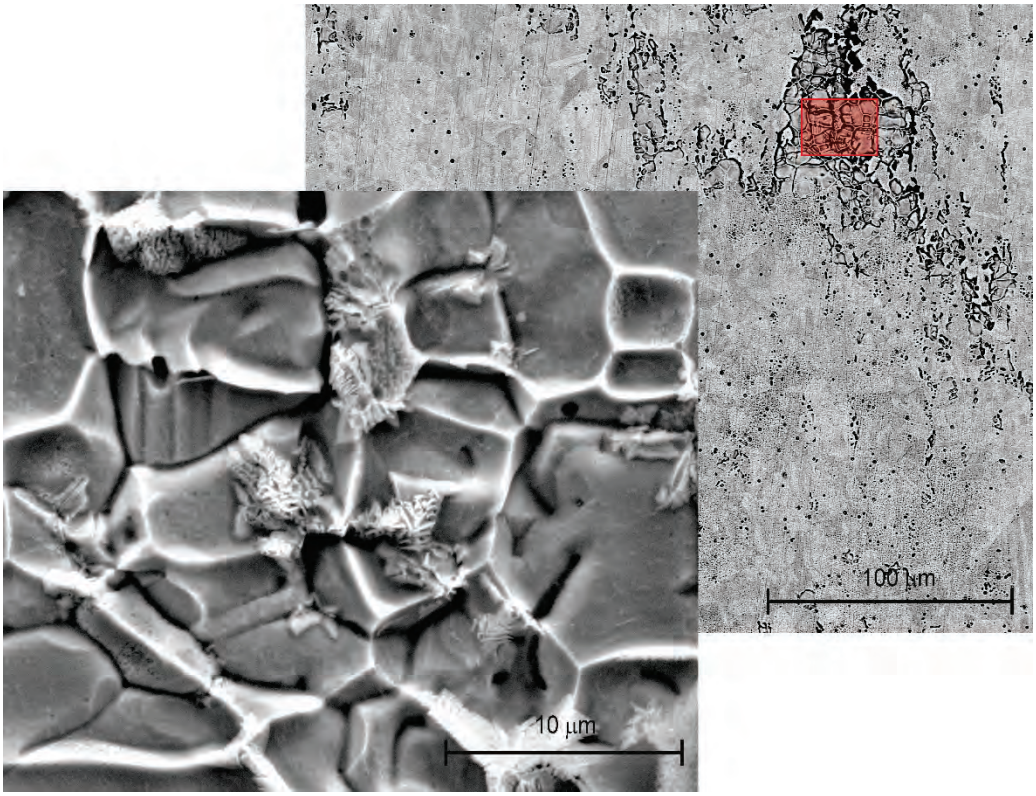

Fig. 4.4 SEM (secondary electron mode) pictures of the surface of 309S steel after the cyclic current-voltage experiment shown in Fig. 4.1

Fig. 4.4 shows a magnification of the region inside the chain-like pit. This picture brings out a grain structure, which differs from that of the alloy matrix. This corresponds certainly to the ferrite precipitate. The picture also shows curled-up tree-like structures. An EDX analysis performed at these structures yields at% C: 24.1, at% Cr: 28.4, at% Fe: 36.2, at% Ni: 6.3, at% Mn: 0.9, at% Si: 0.5, at% O: 2.9, at% V: 0.2 and at% Mo: 0.3. Thus, this Cr-rich structure may arise from the dissolution of Fe-rich phase of a ferritic structure which underwent a eutectic reaction.

Fig. 4.5 shows a series of SEM images giving an overview of the type of attack of 309S steel after cyclic scans in Q2 solution at 85 °C. Unlike the generalized type of attack observed at 27 °C, the appearance of large corroded surface patches of about 300 µm is observed. This type of attack resembles that observed after corrosion in Q3 solution at high pressures (see Fig. 3.19). A strong attack with the formation of elongated deep pits is visible. This is certainly a consequence of the more defective nature at the boundaries of the ferrite segregations. Fig. 4.5b shows a magnification outside the strong local attack. It is seen that the corroded surface left by the expansion of the corrosion patch presents a spongy structure with pores almost tenfold larger than those observed at 27 °C (compare Fig. 4.5b and Fig. 4.3c). Like the surface corroded at 27 °C, deep

rounded pits are formed at 85 °C. Fig. 4.5c shows one of them. An accumulation of corrosion products is visible inside the pit. In particular, the formation of tree-like Cr-rich deposits is visible in a magnification shown in Fig. 4.5d.

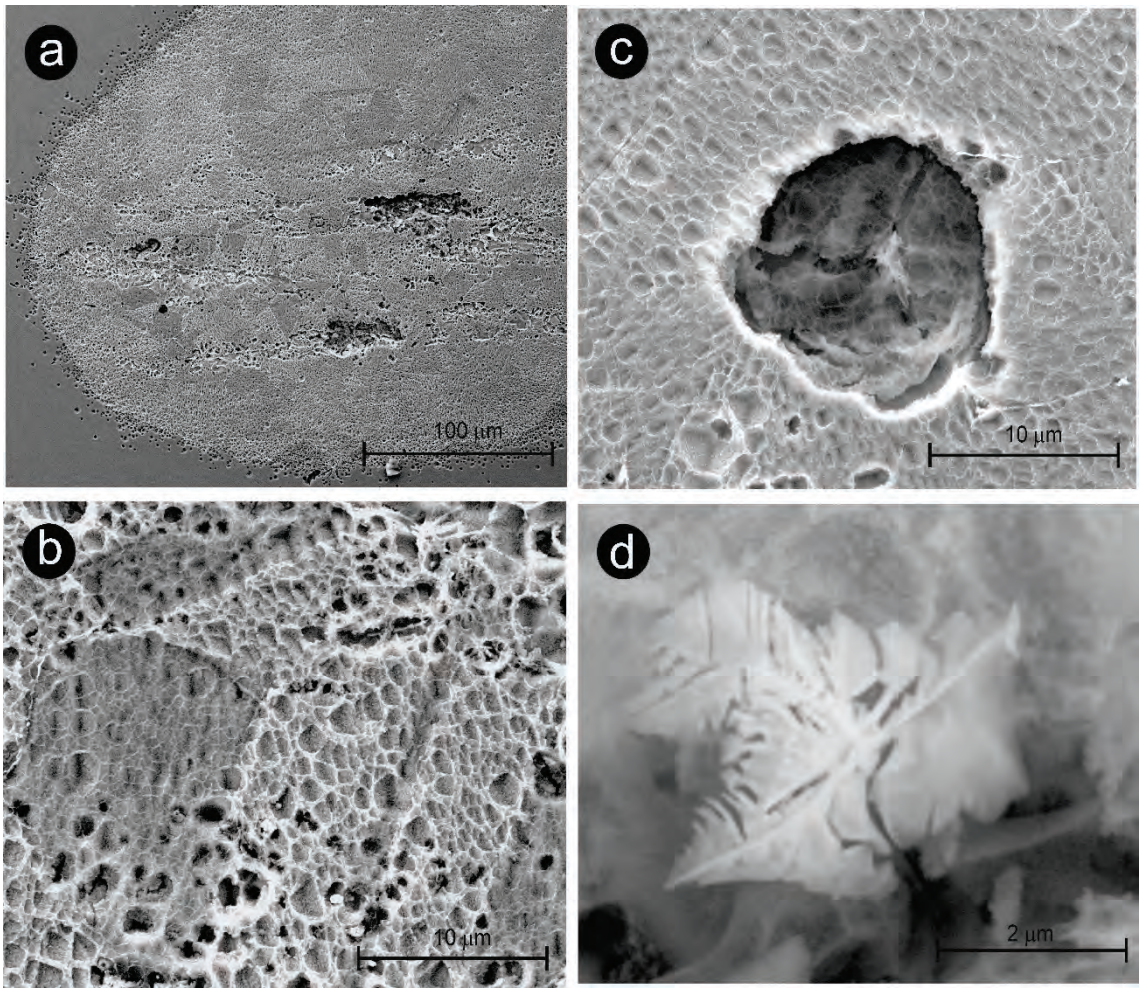

Fig. 4.5 SEM (secondary electron mode) pictures of the surface of 309S steel after the cyclic current-voltage experiment shown in Fig. 4.2

The EDX analysis performed on the attacked spongy-like surface (see Tab. 4.2) indicates an increase of the Cr content above that of bulk, particularly at the protruding white appearing deposits (points 2 and 3). The high concentration of oxygen, on the other hand, supports the identification of the white appearing deposits as precipitated oxides, certainly, $Cr(OH)_3$ or hydrated Cr_2O_3.

Tab. 4.2 Surface elemental composition (at %) at different sites on the corroded area of 309S after the cyclic polarization in Q2 solution at 85 °C, obtained by EDX

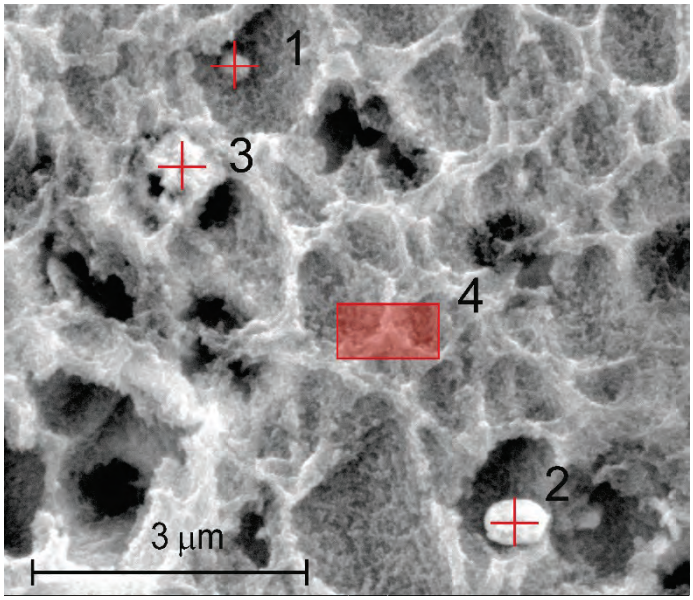

	O-Kα	Mg-Kα	Si-Kα	P-Kα	Cl-Kα	**Cr-Kα**	Mn-Kα	Fe-Kα	Ni-Kα	Mo-Lα
1	**10.7 ±0.8**	0.4 ±0.2	0.8 ±0.1	0.2 ±0.1	0.2 ±0.1	**27.2 ±0.5**	0.9 ±0.5	51.1 ±0.8	8.0 ±0.7	0.4 ±0.1
2	**28.1 ±0.7**	1.2 ±0.2	0.6 ±0.09	0.33 ±0.5	0.5 ±0.1	**29.1 ±0.4**	-	32.4 ±0.6	6.6 ±0.6	0.7 ±0.1
3	**15.6 ±1.4**	0.9 ±0.1	0.6 ±0.09	0.5 ±0.1	0.5 ±0.1	**37.9 ±0.5**	-	36.4 ±0.7	6.8 ±0.6	0.7 ±0.18
4	**17.8 ±0.7**	1.0 ±0.2	0.8 ±0.09	0.3 ±0.1	0.4 ±0.1	**22.6 ±0.4**	0.9 ±0.2	45.8 ±0.7	9.8 ±0.7	0.6 ±0.1

The formation of a dissolution barrier by precipitation of Cr-oxide explains the hysteresis observed in cyclic scans. The strong current noise, on the other hand, points out the weak adhesion of the film and the dynamic fluctuating ionic transport through the film. Beverskog and Puigdomenech /BEV 1999/ reported a thermodynamic study for the ternary system Fe-Cr-Ni at different temperatures.

The Pourbaix diagrams for the ternary system Fe-Cr-Ni calculated by Beverskog and Puigdomenech /BEV 1999/ throw more light on the corrosion mechanism. Due to the strong hydrolysis of Cr^{+3} injected into the solution during the birth of pits, a local acidification is expected, expressed by the reaction:

$$\mathbf{2\ Cr^{3+} + 6\ H_2O \rightarrow Cr_2O_3 \cdot 3\ H_2O + 6\ H^+} \qquad (4.1)$$

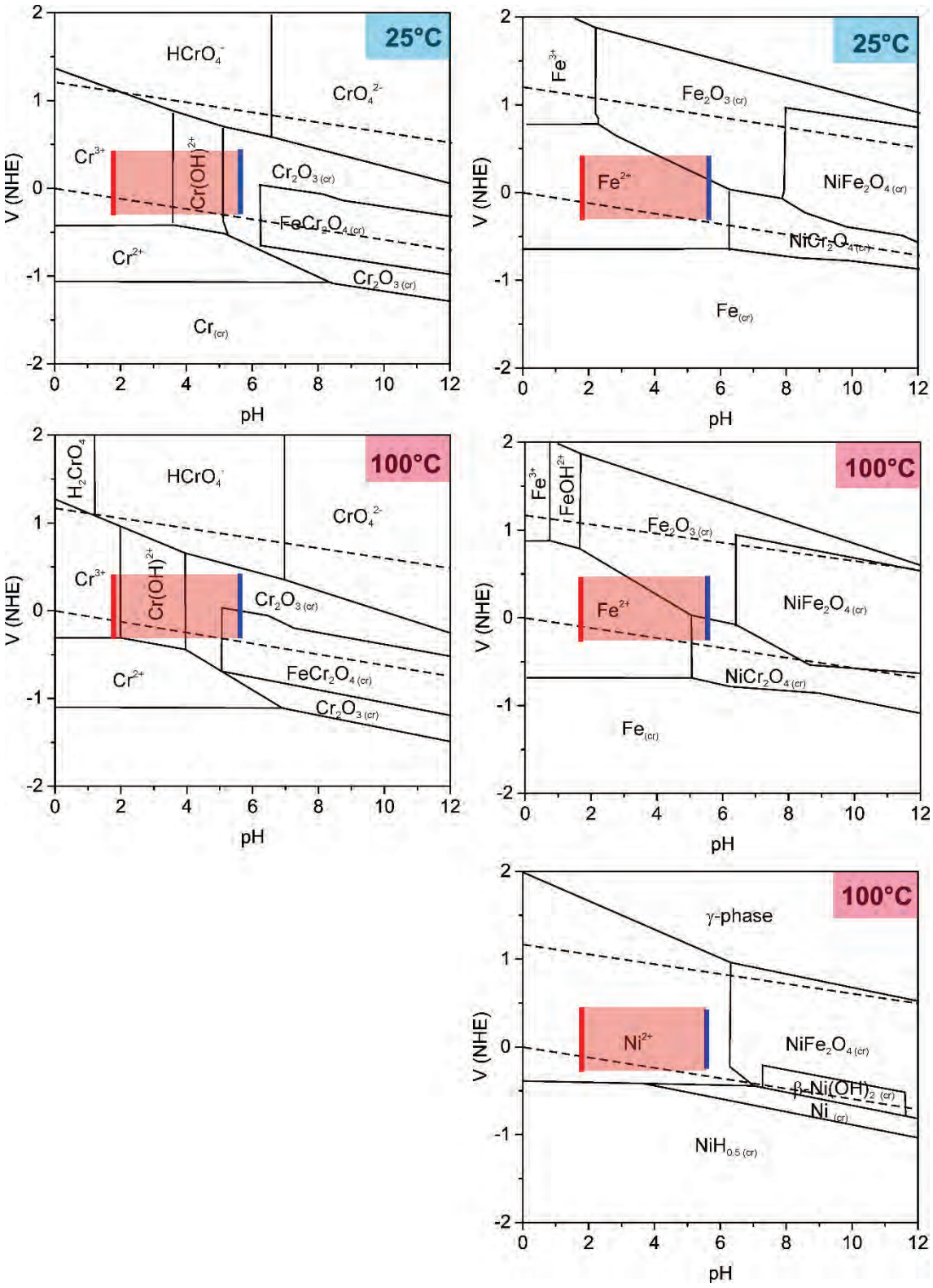

Fig. 4.6 Pourbaix diagrams for the ternary system Fe-Cr-Ni at 25 °C and 100 °C. [Fe(aq)] = [Cr(aq)] = [Ni(aq)] = 10^{-6} mol kg^{-1} (adapted from /BEV 1999/)

According with thermodynamic data listed in Tab. 4.3, a reaction enthalpy ΔH_r^0 = 3542.18 kJ mol^{-1} can be calculated for eq. (4.1). This value determines to a large extent the variation of the reaction constant with temperature as described by the thermodynamic relation (4.2).

Tab. 4.3 Formation enthalpy for various species at 298 K

species	ΔH_f^0 [kJ mol^{-1}]
H^+(aq)	0
H_2O (l)	-285.83
$Cr(H_2O)_6^{3+}$	-1999.1 /KIR 1999/
$Cr_2O_3 \cdot 3H_2O$	-2171.0 /KIR 1999/
Cr_2O_3	-1139.7 /KIR 1999/

$$\log \frac{K^0(T)}{K^0(T_0)} = -\frac{\Delta H_r^0}{R \ln(10)}\left(\frac{1}{T}-\frac{1}{T_0}\right) - \frac{1}{R\,T \ln(10)} \int_{T_0}^{T} \Delta_r C_{p,m}^0(T)\,dT + \frac{1}{R \ln(10)} \int_{T_0}^{T} \frac{\Delta_r C_{p,m}^0(T)}{T}\,dT \qquad (4.2)$$

Assuming a priori $\Delta_r C_{p,m}^0 \approx 0$, a value of log $K^0(T)/K^0(T_0)$ =103.96 can be calculated for the hydrated oxide. A value of log $K^0(T)/K^0(T_0)$ =109.06 is calculated for Cr_2O_3 (cr). The strong local acidification induced by hydrolysis in growing pits is represented by a red line in the Pourbaix diagrams in Fig. 4.6, which also refers to the voltage range swept during the polarization. The dissolution of steel is expected to produce Cr^{3+}, Fe^{2+} and Ni^{2+}. At low pH, the reduction of protons is expected at voltages lower than 0 V (NHE), i. e. V < -0.282 V (Ag/AgCl 1 M KCl). The accumulation of oxide would generate a barrier limiting further dissolution. The outward diffusion of protons and the neutralization of the attacked region is represented by the blue line in the Pourbaix diagrams. According to these diagrams, no $Ni(OH)_2$ can be stable under these conditions. At low temperatures, Cr_2O_3 and α-Fe_2O_3 are the expected predominating corrosion products. At temperatures near 100 °C, the stability is reduced by the formation of bimetallic oxides $FeCr_2O_4$, and $NiCr_2O_4$.

5 Surface spectroscopy analysis: XPS

The modification of the surface chemistry during the anodic attack was investigated by x-ray photoelectron spectroscopy (PES). This technique is based in the measurement of the kinetic energy of photoemitted electrons upon irradiation of the surface with x-ray. The method allows the identification of the chemical state or chemical environment of elements in a thin layer of several nm depth. This differs from the EDX technique based on the inverse phenomenon, i.e. the emission of x-ray by electron bombardment, embracing a depth of some μm. Because x-ray emission provides information about the core electronic structure, this technique can identify elements but not their chemical environment.

The core level spectroscopic lines of the different elements were deconvoluted using the software UNIFIT 2019. For the peak fitting, the convolution of the Lorentzian and Gaussian function (see equations 5.1 and 5.2), known as Pseudo-Voigt profile $V_p(E)$, was used.

$$\boldsymbol{L(E) = \left\{1 + \left[\frac{E-E_0}{\beta}\right]^2\right\}^{-1}} \quad (5.1)$$

$$\boldsymbol{G(E) = exp\left\{-ln\,2\left[\frac{E-E_0}{\beta}\right]^2\right\}} \quad (5.2)$$

$$\boldsymbol{V(E) = \eta\, L(E) + (1-\eta)\, G(E);} \quad \boldsymbol{0 < \eta < 1} \quad (5.3)$$

E: energy, E_0: peak energy, 2β: full width at half maximum. The Lorentzian distribution function accounts for the finite lifetime of the core level hole state during photoemission process. This distribution, in turn, is broadened by a Gaussian function accounting for the measurement process in the spectrometer. The background was fitted parallel to the peak fitting process. For this, the universal background description (Eq. 5.4) was applied.

$$\boldsymbol{B(E) = a + b\,E + c\,E^2 + d\,E^3 + e\,S(E) + f\,T(E)} \quad (5.4)$$

S(E): Shirley background, T(E): Tougaard background.

The binding energy scale was calibrated using well-established binding energies of elemental lines of pure metals (monochromatic Al Kα: Cu 2p3/2 at 932.62 eV, Au 4f7/2 at 83.96 eV) /SEA 1998/. Spectra of isolating surfaces were charge referenced to C 1s of adventitious carbon at 284.8 eV /MOU 1995/ (see discussion below). For the assignment of the peaks to chemical entities, the NIST data base was used mostly /NIS 2012/.

5.1 Surface attack at low temperatures and low pressure in Q3 solution

Fig. 5.1 shows a survey spectrum taken inside a large pit of a 309S steel sample after surface corrosion during a cyclic polarization in Q3 solution at 23 °C. Strong signals of O, C and Cr appear together with lesser strong signals of Fe, Mo and Cl. The Ni and S signals appear very weak.

The elemental quantification shown in Tab. 5.1 can be interpreted in terms of a surface Cr-rich iron oxide. The presence of Cl and S signals account for adsorbed Cl^- and SO_4^{2-} ions.

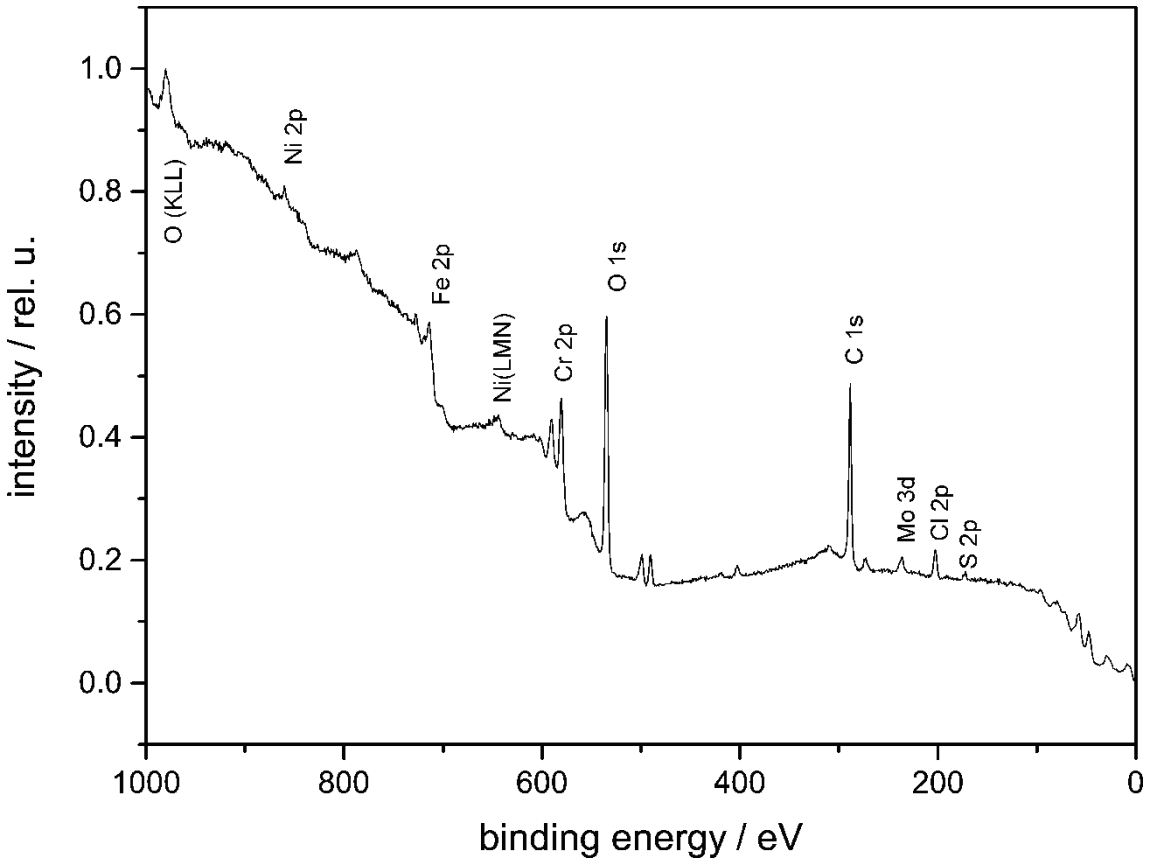

Fig. 5.1 Survey PES spectrum for the surface inside a large pit after a cyclic polarization in Q3 solution at 23 °C

Tab. 5.1 Elemental composition calculated from the spectrum shown in Fig. 5.1. Error: ± 10 – 20 %

element	C	N	O	S	Cl	Cr	Fe	Ni	Mo
at%	45.3	0.9	32.2	0.7	2.3	8.1	9.6	0.5	0.4

The carbon signal, which appears with a large intensity on the corroded sample is generally attributed to adventitious carbon /SIE 1967/, /SWI 1985/. The source of the carbon contamination upon exposure of samples to the air is not sufficiently clear and several interpretations were given (see discussion in the paper of Miller et.al. /MIL 2002/). /MIL 2002/ has observed that at the surface of pure iron samples exposed to a CO_2 atmosphere FeO and a patchy carbonaceous layer with an interfacial layer of some oxyhydrocarbons is formed. The carbon signal is used as a reference to correct deviations of the binding energy scale by charging of non-conducting surfaces. Greczynski and Hultman /GRE 2018/ have given advice that energy of adventitious carbon should be referred to vacuum and not, as usually, to the Fermi level of the sample, because this layer has no electrical contact to the sample.

Without disregarding possible carbon contaminations produced during the short contact of the sample with the air during extraction of samples from the reactor, it is important to remark the larger contribution of carbon released upon dissolution of austenitic phase. The nature of this later type of carbon was investigated by Ninomiya et.al. /NIN 2020/ using soft X-ray absorption technique on samples of low carbon steel. This technique allows to distinguish the carbon that arises from the solid solution from that formed by contamination. They have found out, that a layer of 3 nm consisting in contaminating carbon, iron hydroxide and iron oxide covers the surface of a mirror polished sample. On the other hand, the heat treatment increases the proportion of graphitic sp^2 in the bulk, suggesting that the alloying carbon consists in a mixture of sp^2 and sp^3 structures.

Diaz et.al. /DIA 1996/ were able to identify sp^2 and sp^3 components of the C 1s signal in amorphous carbon deposited by pulse layer evaporation of graphite. According to this study, the sp^2 and sp^3 lines appear at 284.4 ± 0.1 eV and 285.3 ± 0.1 eV, respectively.

Fig. 5.2 shows the C 1s core level spectrum taken on a spot inside the attacked surface. The signal deconvolution shows a main peak, assigned to sp^2 carbon, which was set at 284.8 eV (data obtained from calibrated spectrometer were shifted by ΔE: +1.17 eV to account for charging effects). A second peak at 285.9 eV, assigned to sp^3 carbon and a tiny peak at 288.6 eV assigned to C = O bounds /BEA 1992/ appear. The other element spectra were likewise corrected by charge.

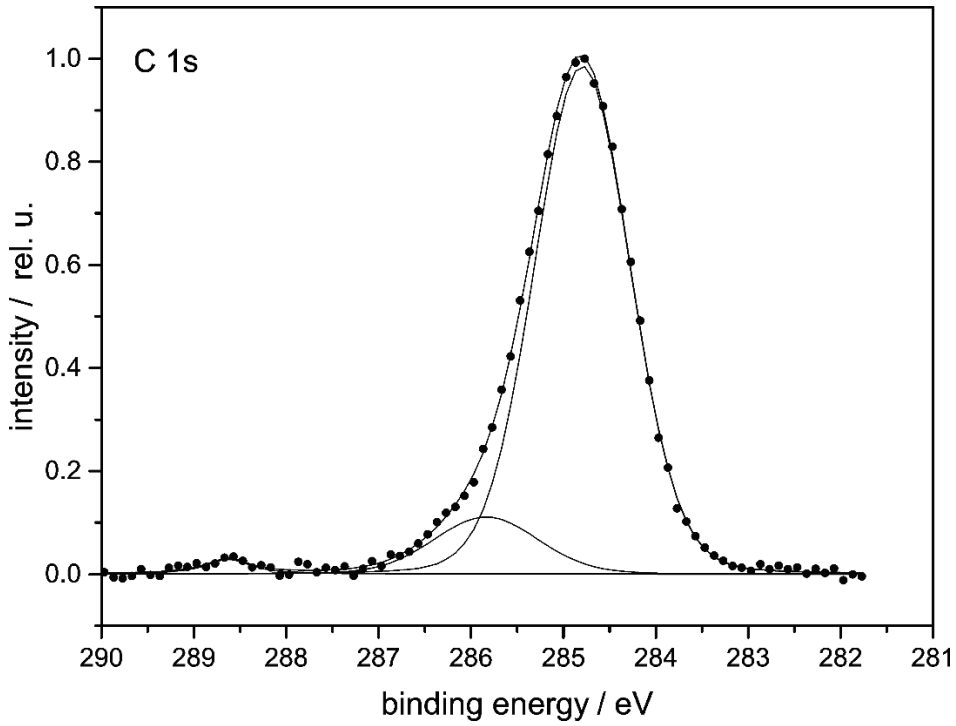

Fig. 5.2 C 1s core level signal for the surface inside a large pit after a cyclic polarization in Q3 solution at 23 °C

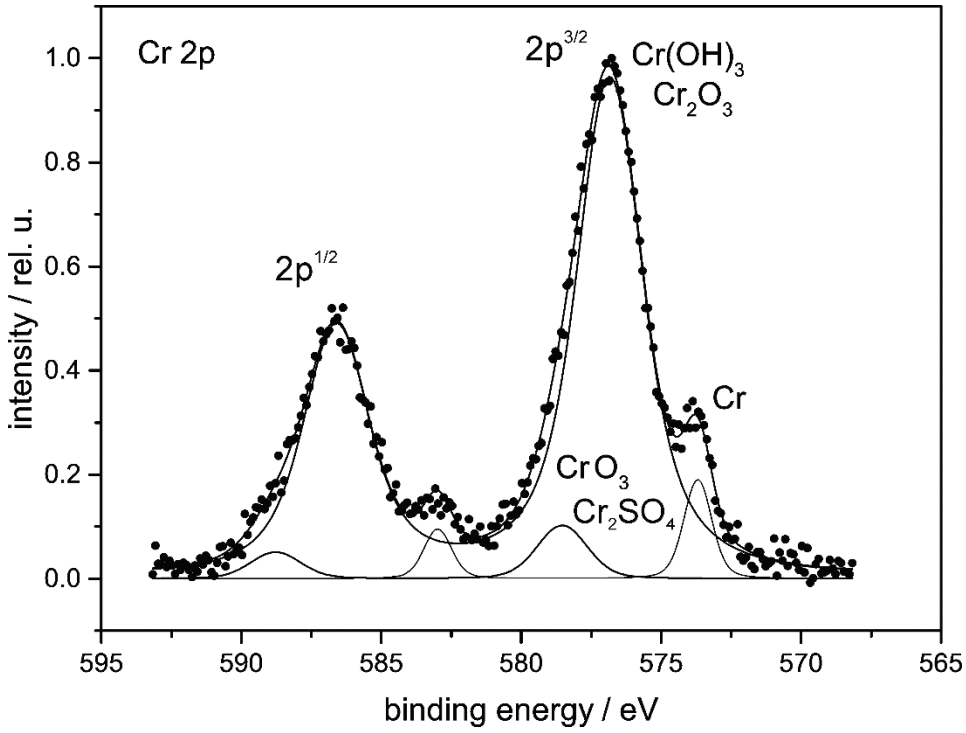

Fig. 5.3 Cr 2p core level signal for the surface inside a large pit after a cyclic polarization in Q3 solution at 23 °C

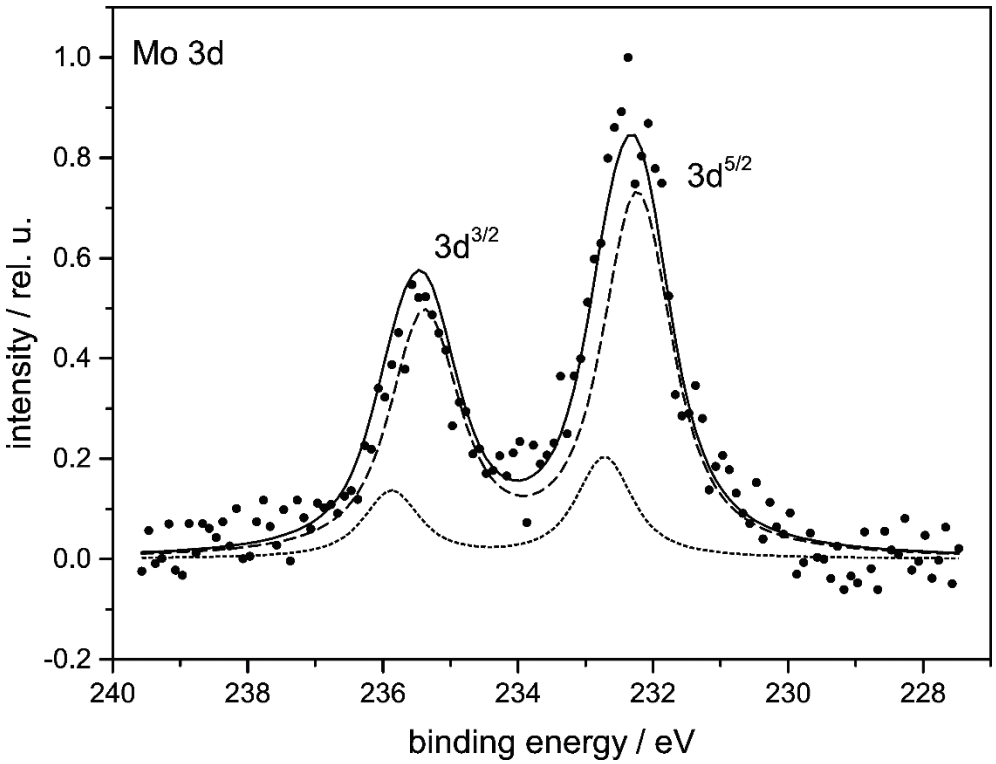

Fig. 5.4 Mo 3d core level signal for the surface inside a large pit after a cyclic polarization in Q3 solution at 23 °C

The Cr 2p core level signal was deconvoluted in three components. The $3d^{5/2}$ and $3d^{3/2}$ doublet were constrained to have 3:2 peak area ratios, equal FWHM and a peak separation of 3.15 eV. The first line with a $2p^{3/2}$ peak at 573.68 eV can be ascribed to Cr metal (rel. area $2p^{3/2}$: 0.043). The second one, which dominates, has a peak at 576.9 eV and can be assigned to chrome oxide (Cr_2O_3) (rel. area $2p^{3/2}$: 0.585). The third peak at 578.6 eV can be assigned to CrO_3 or to $Cr_2(SO4)$ (rel. area $2p^{3/2}$: 0.040)

The deconvolution of the core level spectrum for Mo (see Fig. 5.4) shows two components. The first and larger one, with a peak energy ($3d^{5/2}$) of 232.2 eV can be assigned, according to the NIST data base /NIS 2012/, to MoO_3. The second peak, shifted by +0.50 eV, can be ascribed to a non-stoichiometric oxide MoO_x.

The Cl 2p core level signal shown in Fig. 5.5 can be deconvoluted in two components. The $2p^{3/2}$ peak of the first component appears at 198.34 eV with a Gaussian FWHM of 1.03 eV and a Lorentzian one of 0.55 eV. This peak energy can be assigned to NaCl. The other component has a Gaussian FWHM of 1.91 eV and a Lorentzian FWHM of 0.1 eV. This type of distribution accounts for a high disorder with a wide distribution of bond lengths. The binding energy of the $2p^{3/2}$ peak appears at 199.08 eV. The Cl $2p^{3/2}$

lines of $FeCl_3$, $MoCl_2$ and $NiCl_2$ appears close to this energy. Thus, we can argue, that this part of the signal corresponds to M-Cl (M: metal cations) bond in a surface oxide partially broken by the penetration of Cl-ions.

The O 1s core level spectrum shown in Fig. 5.6 can be deconvoluted in three components: at 531.7 eV, 530.4 eV and 529.7 eV with relative areas of 0.76, 0.19 and 0.05 respectively. The first peak can be assigned to nickel and chrome hydroxides and to iron oxy-hydroxide. The other two peaks correspond to M-O bond in different possible oxides.

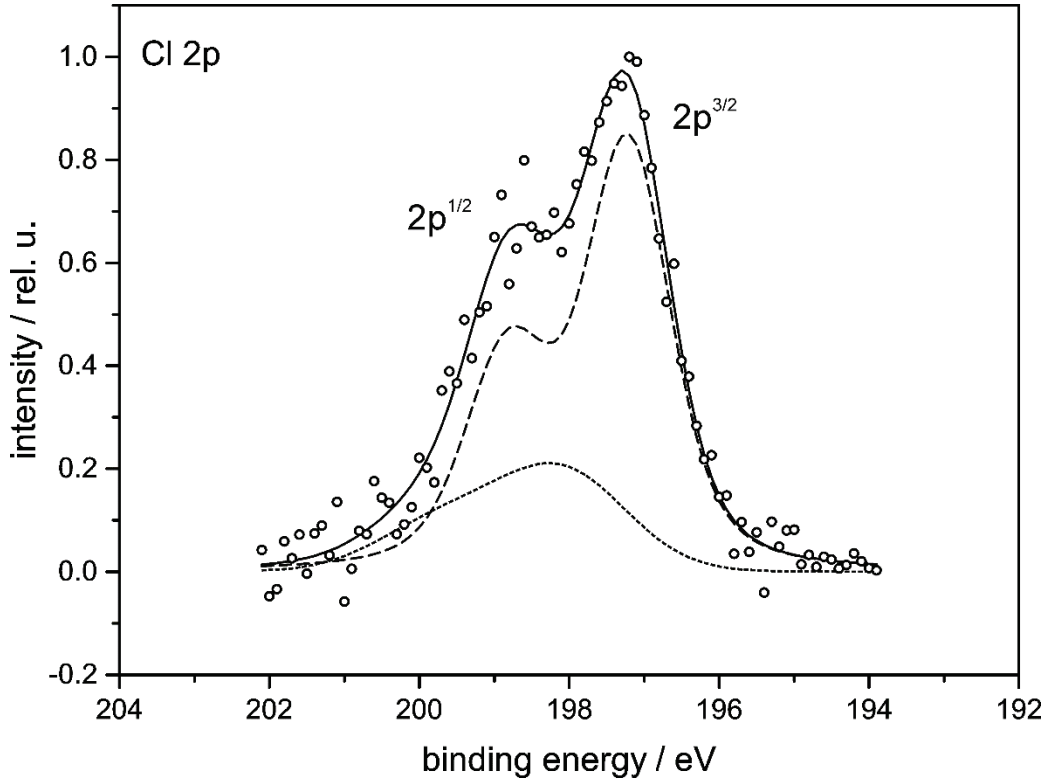

Fig. 5.5 Cl 2p core level signal for the surface inside a large pit after a cyclic polarization in Q3 solution at 23 °C

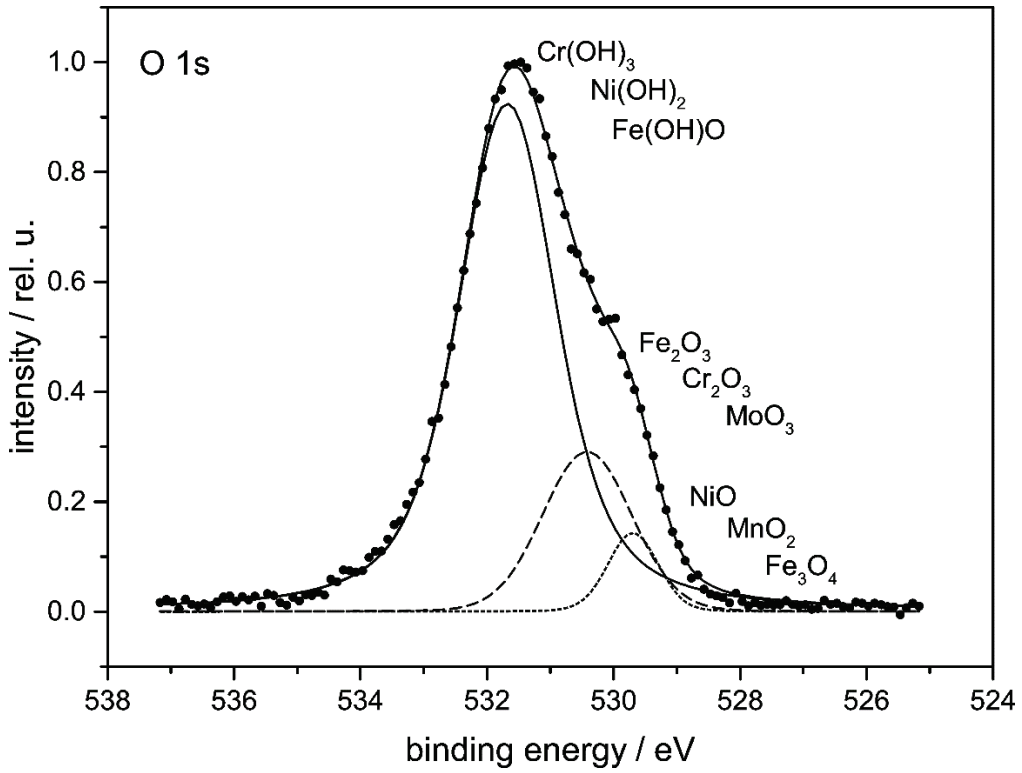

Fig. 5.6 O 1s core level signal for the surface inside a large pit after a cyclic polarization in Q3 solution at 23 °C

Fig. 5.7 shows a deconvoluted Fe 2p core level spectrum obtained inside a large pit. This can be fitted introducing 5 components. The corresponding peak energies for the $2p^{3/2}$ line are listed in Tab. 5.2. The line asymmetry for the first component was taken as a variable, assuming a priori, that this corresponds to the signal of metallic iron. Comparing the Cr 2p (Fig. 5.3) and Fe 2p spectra (Fig. 5.7), it can be seen that the intensity ratio I_{oxide}/I_{metal} is 1.03 for iron and 14.18 for Cr. This result let infer that the bottom of the hollow pit is covered by a patchy oxide and that the Cr oxidizes preferentially, leaving a Fe-rich alloy.

The $2p^{3/2}$ line at 168.6 eV in the S 2p spectrum shown in Fig. 5.8 can be assigned to Na_2SO_4 and $FeSO_4$.

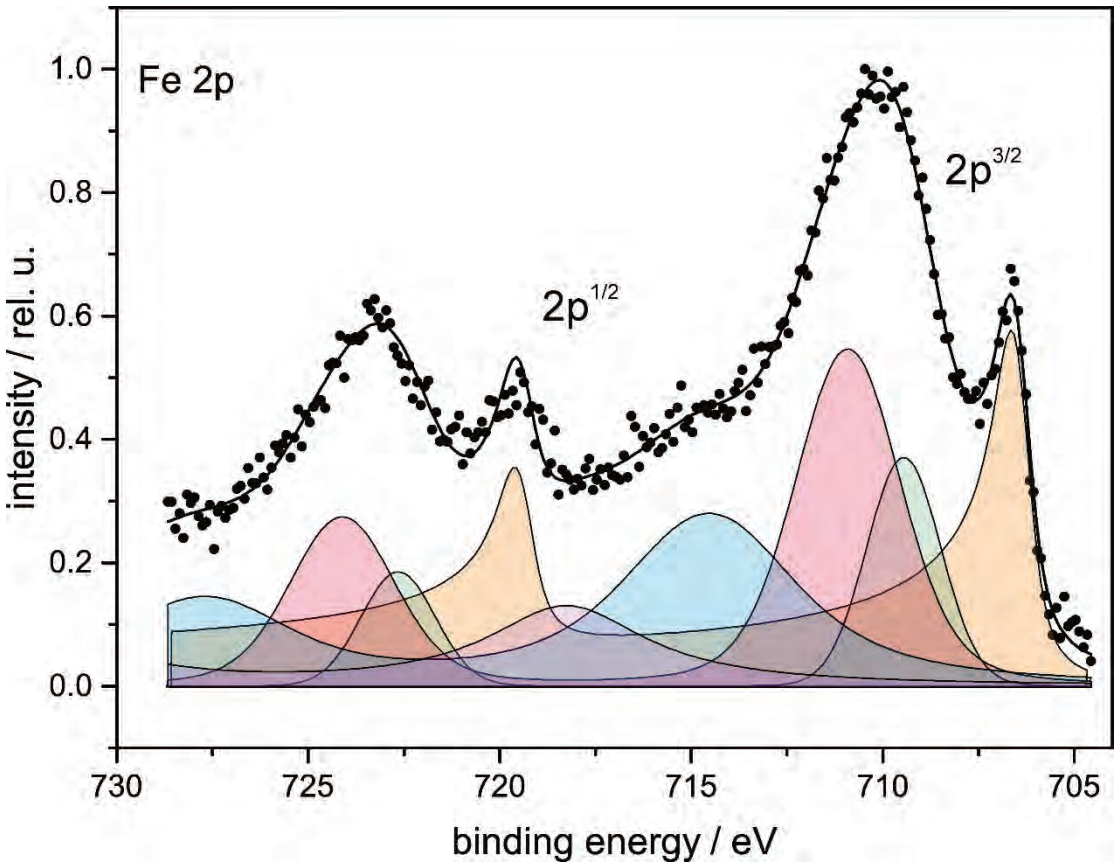

Fig. 5.7 Fe 2p core level signal for the surface inside a large pit after a cyclic polarization in Q3 solution at 23 °C (spectrum corrected by charge ΔE: +1.46 eV)

Tab. 5.2 Assignments of deconvolution components for the Fe 2p core level spectrum shown in Fig. 5.7

E $2p^{3/2}$ / bar(*relative area*)	**Assignments**
706.6 (asymmetry: 0.374) (*0.231*)	Fe metal
709.5 (*0.073*)	FeO
710.9 (*0.166*)	Fe_2O_3, Fe(OH)O
714.5 (*0.160*)	satellite Fe(II)
718.3 (*0.074*)	satellite Fe(III)

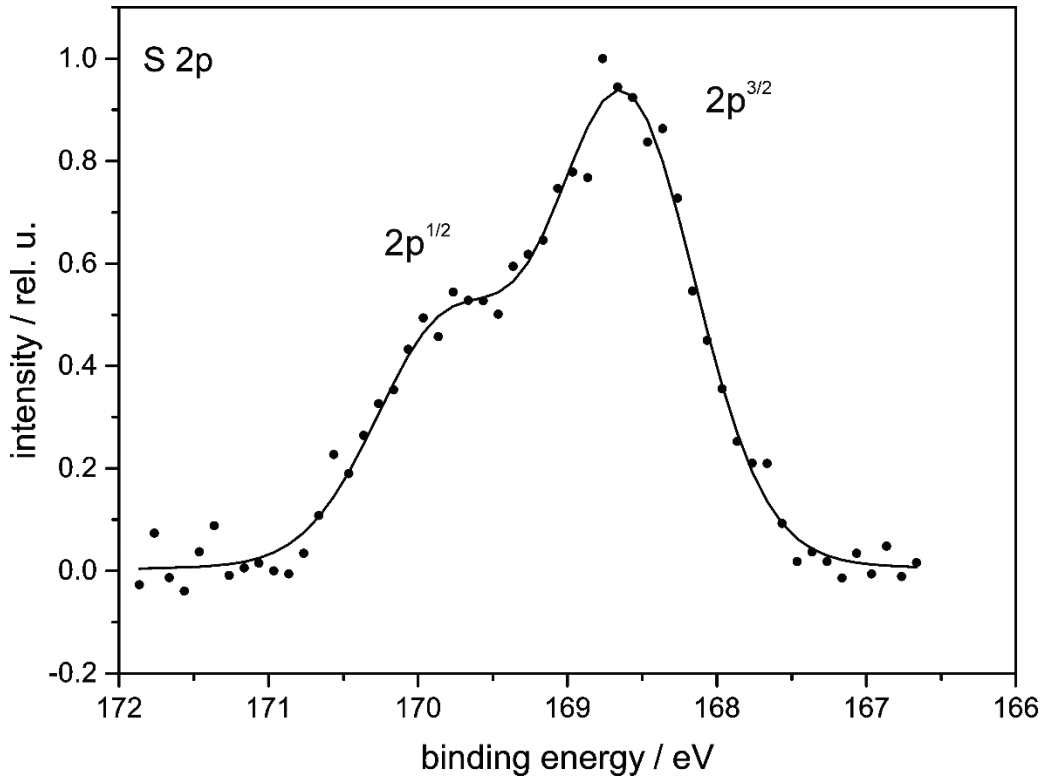

Fig. 5.8 S 2p core level signal for the surface inside a large pit after a cyclic polarization in Q3 solution at 23 °C (spectrum corrected by charge ΔE: +1.46 eV)

The deconvolution of the Fe 2p core level spectrum for point of analysis outside the attacked surface shows that the signal can be fitted using 5 components as in Fig. 5.7. The corresponding energies for the $2p^{3/2}$ are listed in Tab. 5.3. The spectrum indicates a similar surface chemical composition as that at the bottom of the pit. The ratio of FeO to Fe_2O_3 of 0.44 at the bottom of pit changes to 0.68 on the non-corroded surface. The ratio of Fe metal to iron in the oxide, on the other hand, decreases from 0.96 to 0.24 at the non-attacked surface.

Tab. 5.4 presents a surface elemental composition of the non-corroded part of the sample in comparison with that at the bottom of the pit. It is interesting to note, that S and Cl are also detected at the native oxide before the attack. The amount of Cl increases by 7 times inside the pit, whiles the amount of S practically does not change. The relation at% O / (at% Fe + at% Cr) varies from 2.24 in the uncorroded surface to 1.81 in the pit. These results support the assumption of a dissolution of the oxide with exposition of the metal surface during the attack.

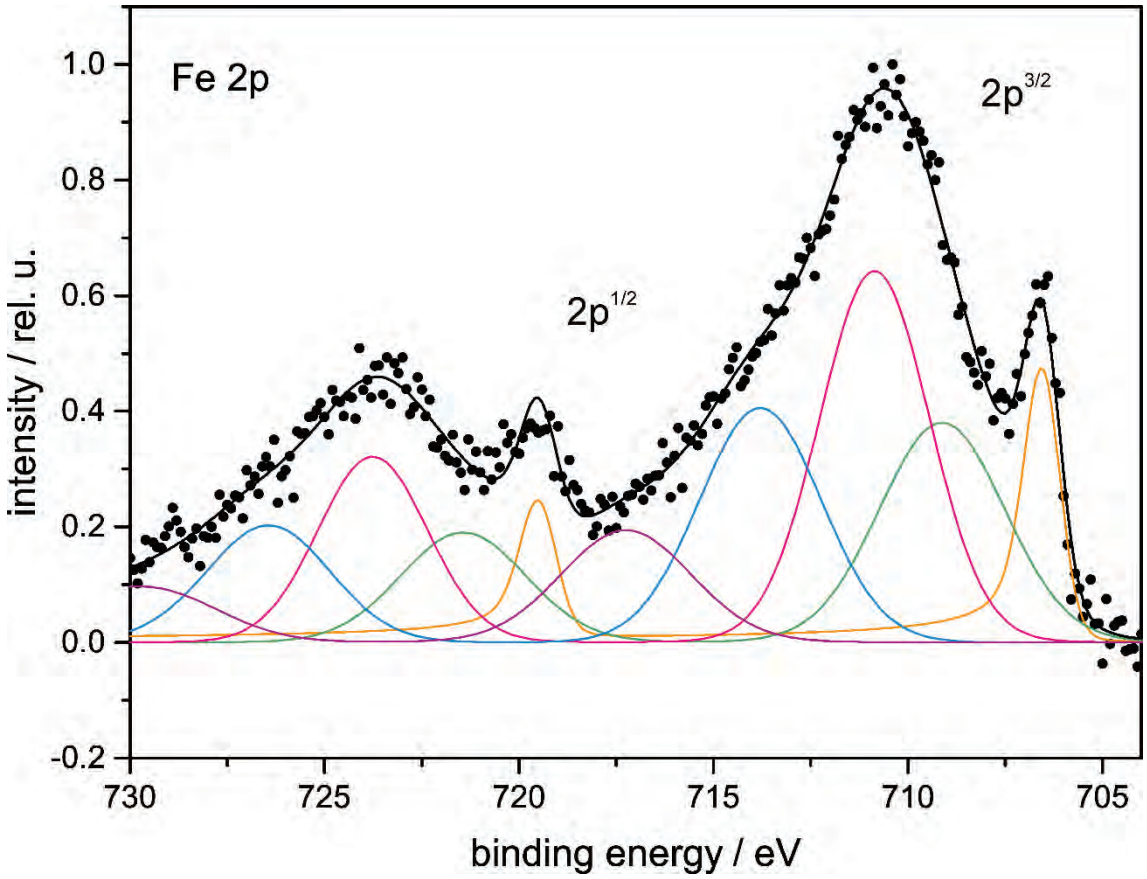

Fig. 5.9 Fe 2p core level signal for the surface outside pits after a cyclic polarization in Q3 solution at 23 °C (spectrum corrected by charge ΔE: +1.3 eV)

Tab. 5.3 Assignments of deconvolution components for the Fe 2p core level spectrum shown in Fig. 5.9

E $2p^{3/2}$ / eV (*relative area*)	**Assignments**
706.5 (asymmetry: 0.139) (*0.086*)	Fe metal
709.2 (*0.144*)	FeO
710.9 (*0.212*)	Fe_2O_3, Fe(OH)O
713.8 (*0.149*)	satellite Fe(II)
717.3 (*0.077*)	satellite Fe(III)

Tab. 5.4 Elemental composition calculated from a survey spectrum taken outside the corroded area. Error ± 10 – 20 %. Number in parentheses: values for the corroded area

element	**C**	**N**	**O**	**S**	**Cl**	**Cr**	**Fe**	**Ni**	**Mo**
at%	60.2 (45.3)	1.4 (0.9)	26.0 (32.2)	0.5 (0.7)	0.3 (2.3)	4.8 (8.1)	6.8 (9.6)	- (0.5)	- (0.4)

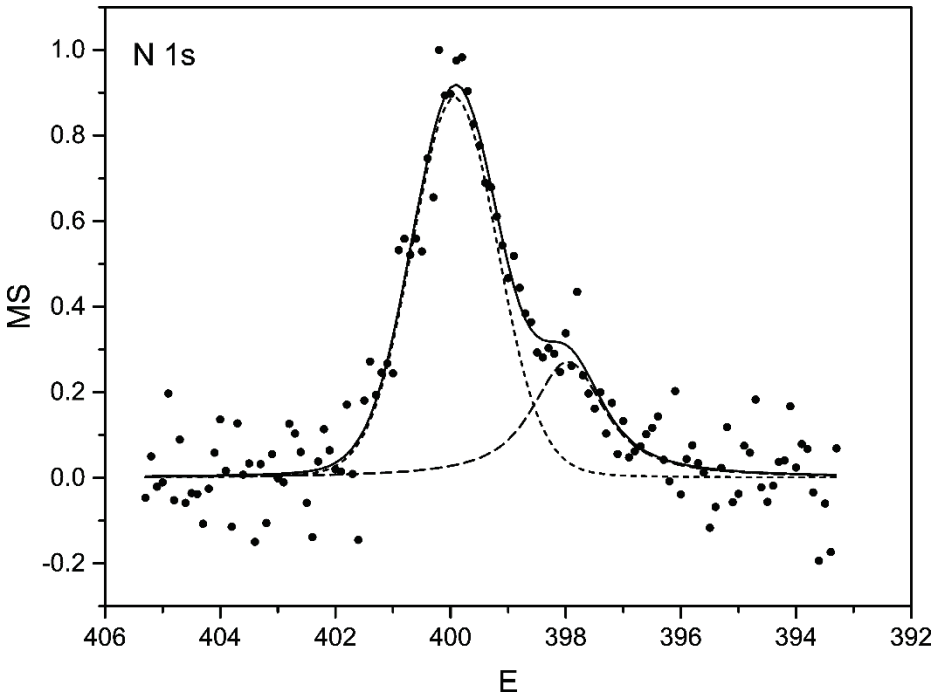

Fig. 5.10 N 1s core level signal for the surface outside pits after a cyclic polarization in Q3 solution at 23 °C (spectrum corrected by charge)

Fig. 5.10 shows the deconvoluted N 1s core level signal from the non-attacked surface. Two components can be distinguished: a large signal at 399.9 eV and a smaller one at 398.0 eV. Baba et. al. /BAB 2002/ have found that N in austenitic steels is dissolved in the form of NH_3. According to these authors, the release of NH_3 provides a strong repassivating effect. In fact, the large N 1s signal observed in the uncorroded surface may be ascribed to NH_3 /NIS 2012/. The second, smaller peak can be assigned to Si_3N_4.

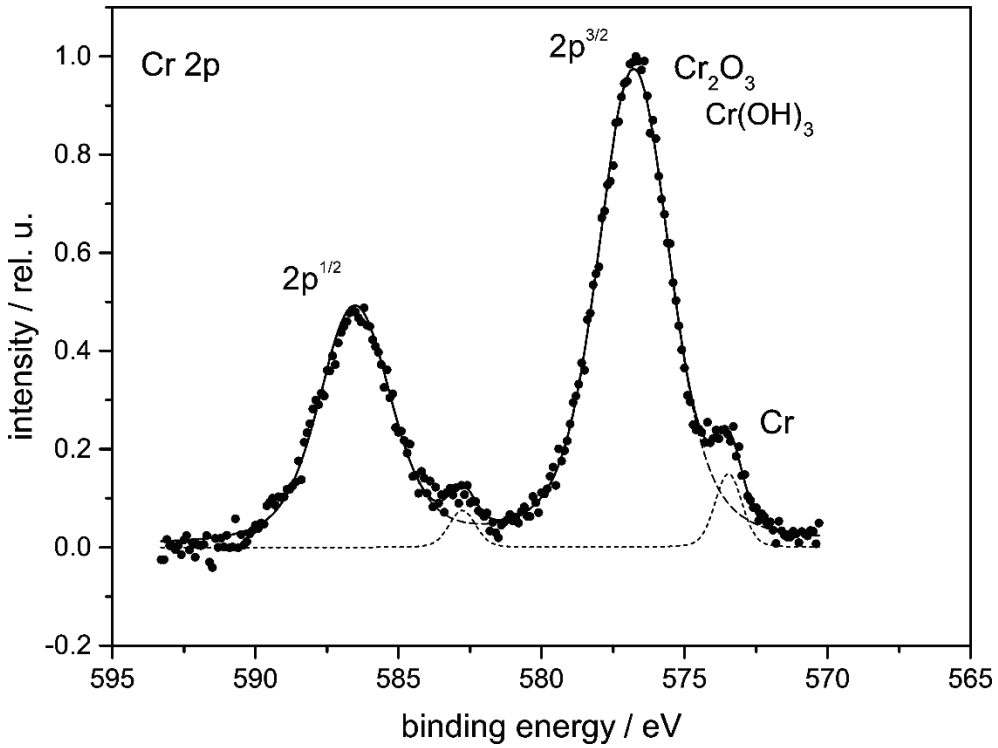

Fig. 5.11 Cr 2p core level signal for the surface outside pits after a cyclic polarization in Q3 solution at 23 °C (spectrum corrected by charge)

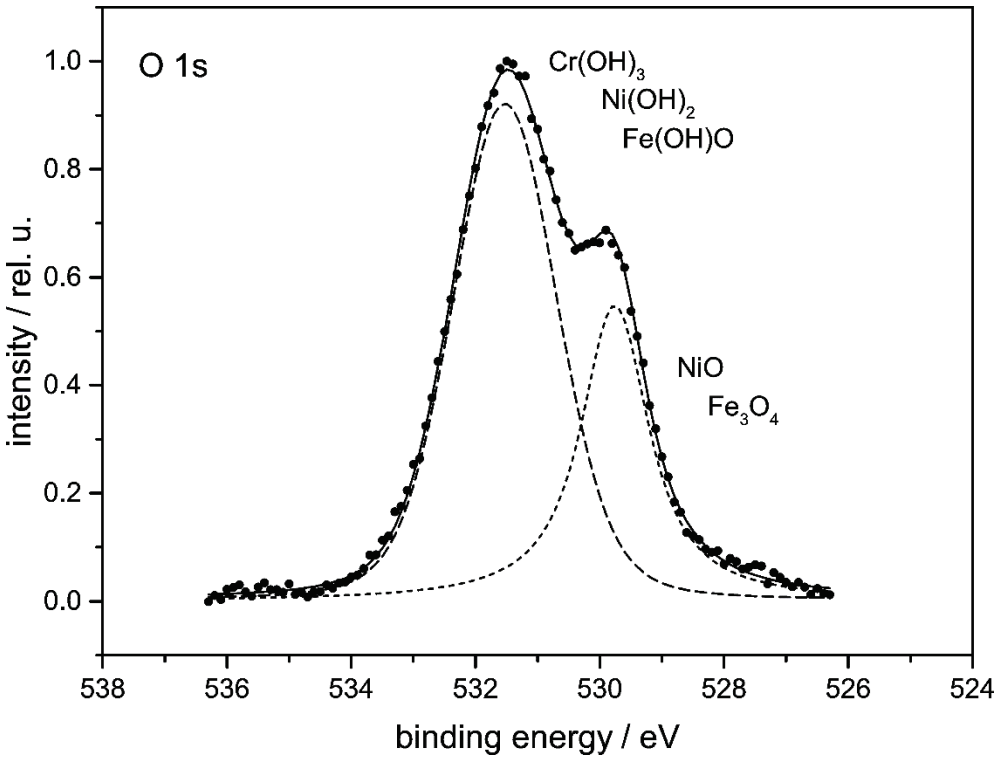

Fig. 5.12 O 1s core level signal for the surface outside pits after a cyclic polarization in Q3 solution at 23 °C (spectrum corrected by charge)

The deconvolution of the Cr 2p core level signal on the non-attacked surface (Fig. 5.11) shows a main peak at 576.7 eV, which can be assigned to Cr_2O_3. But, the close binding energy reported for $Cr(OH)_3$ does not let to distinguish in which proportion both compounds are. The smaller peak, at 573.4 eV corresponds to Cr metal. The spectrum differs from that taken in the attacked surface region (Fig. 5.3) just only in the presence of a third peak at 578.6 eV. The corresponding O 1s core level signal shown in Fig. 5.12 let infer that $Cr(OH)_3$ is rather the predominating surface compound. The O 1s lines for Cr_2O_3 and $Cr(OH)_3$ are separated by about 1 eV /NIS 2012/.

In comparison with the O 1s spectrum for the attacked surface (Fig. 5.6), that outside the pit (Fig. 5.12) does not show a third peak at 530.4 eV. The assignment of this later embraces the compounds Fe(OH)O, MoO_2, Fe_2O_3 and MoO_3. The absence of Ni and Mo in the survey spectrum lets infer, that the surface outside the pit is covered by a mixed Cr-Fe oxide constituted by hydrated Cr_2O_3 ($Cr(OH)_3$), Fe_2O_3, FeO and Fe(OH)O.

5.2 Surface attack at high temperature and high pressure in Q3 solution

Fig. 5.13 shows the Mo 3d core level spectrum obtained inside the large pit shown in Fig. 3.19. The signal can be deconvoluted in two components with $2p^{5/2}$ energies at 228.5 eV and 229.8 eV, which can be ascribed to MoO and MoO_2 respectively. Only a weak signal with a large dispersion was obtained outside the pit. The presence of chloride could be detected by the Cl 2p signal in Fig. 5.14. The signal can be fitted with only one line at 198.9 eV, which can a priori be ascribed to NaCl and/or $FeCl_2$. It is probable, however, that the signal arises from a chemical environment represented by FeO_xCl_y. An assignment to NaCl can be excluded, since characteristic NaCl crystals were not visible in the corresponding SEM images.

Fig. 5.15 shows the Cr $2p^{3/2}$ core level signal for a site inside the pit, which could be deconvoluted in three lines at 574.3 eV, 576.2 eV and 577.5 eV. They can be assigned to Cr metal, Cr_2O_3 and $Cr(OH)_3$ respectively. This composition differs from that measured on the surface around the pit, where two lines at 573.9 eV and 576.7 eV, corresponding to Cr metal and Cr_2O_3 respectively can be obtained from the signal deconvolution. It can be noted that the Cr_2O_3 predominates in the non-attacked surface. In the pit, this signal vanishes whereas those of the free metal surface and of $Cr(OH)_3$ increases. This result can be related with the dissolution of the native oxide during the corrosion process.

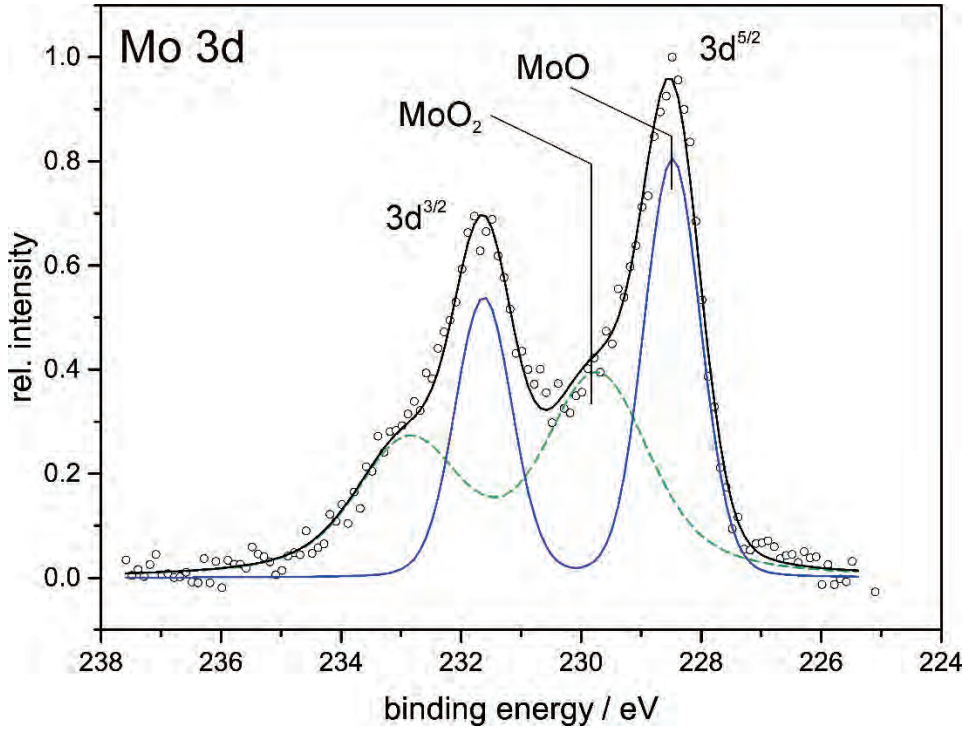

Fig. 5.13 Mo 3d core level signal for the surface inside corroded area after the anodic polarization 6 shown in Fig. 3.17 in Q3 solution at 80 °C and 50 bar

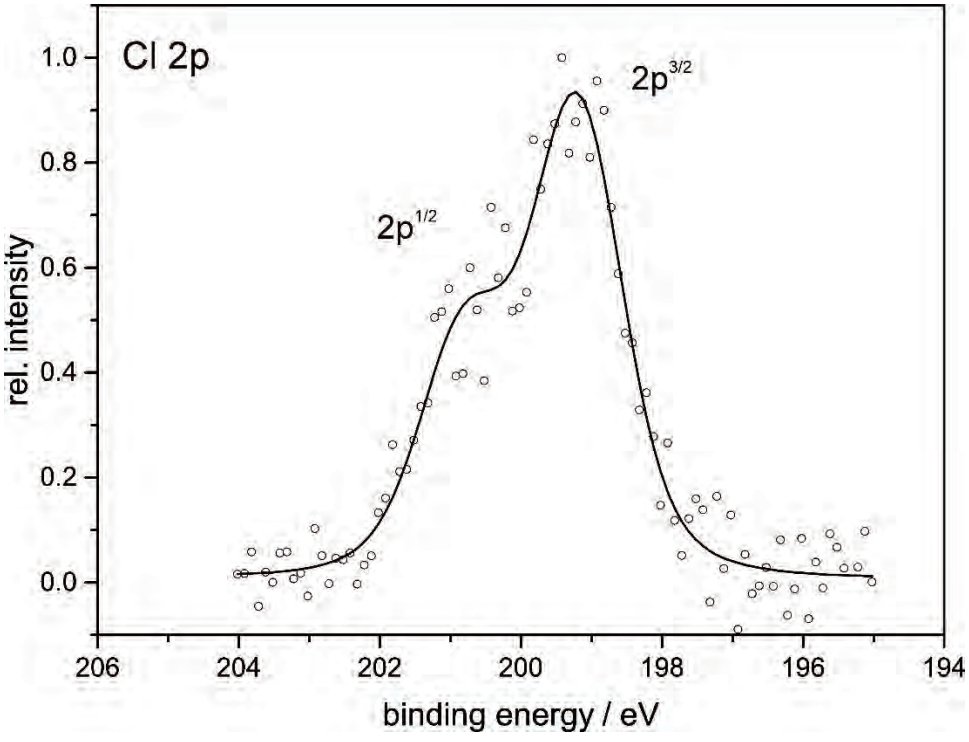

Fig. 5.14 Cl 2p core level spectrum for the surface inside corroded area after the anodic polarization 6 shown in Fig. 3.17 in Q3 solution at 80 °C and 50 bar

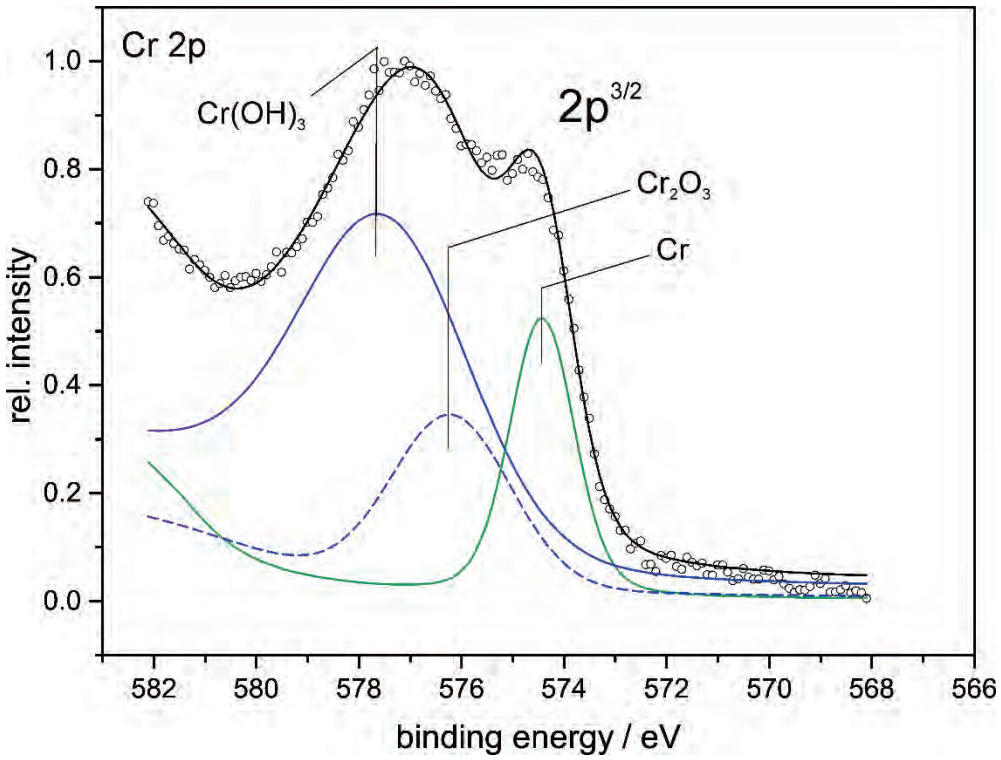

Fig. 5.15 Cr 2p core level spectrum for the surface inside corroded area after the anodic polarization 6 shown in Fig. 3.17 in Q3 solution at 80 °C and 50 bar

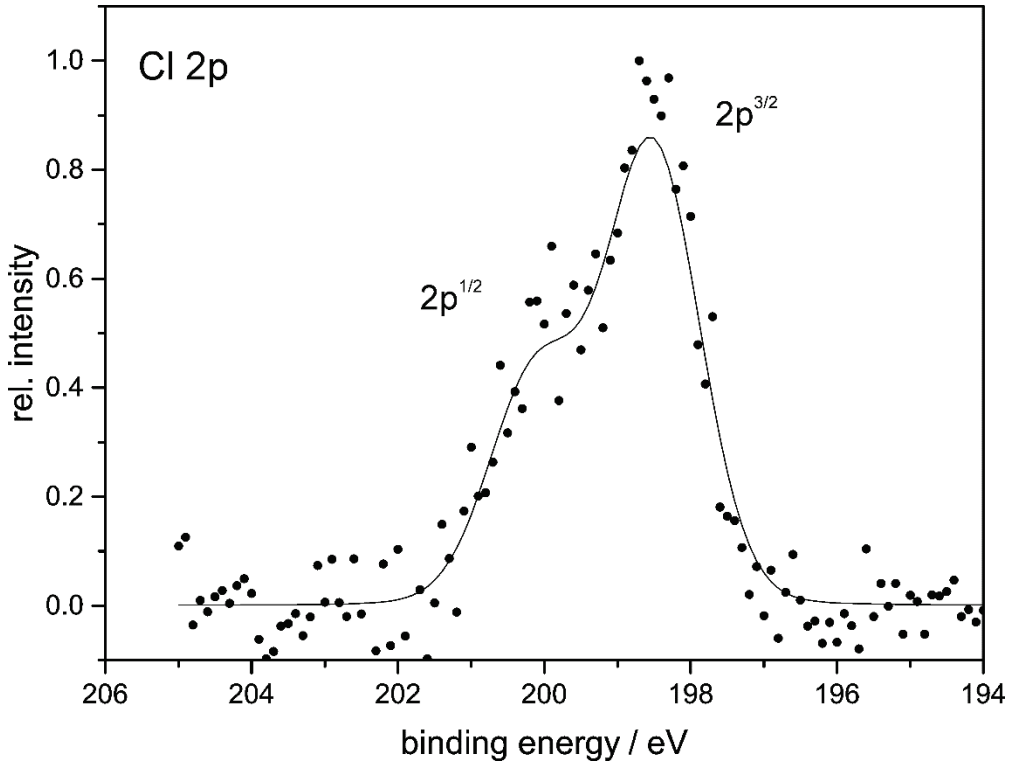

Fig. 5.16 Cl 2p core level spectrum for the surface outside the corroded area after the anodic polarization 6 shown in Fig. 3.17 in Q3 solution at 80 °C and 50 bar

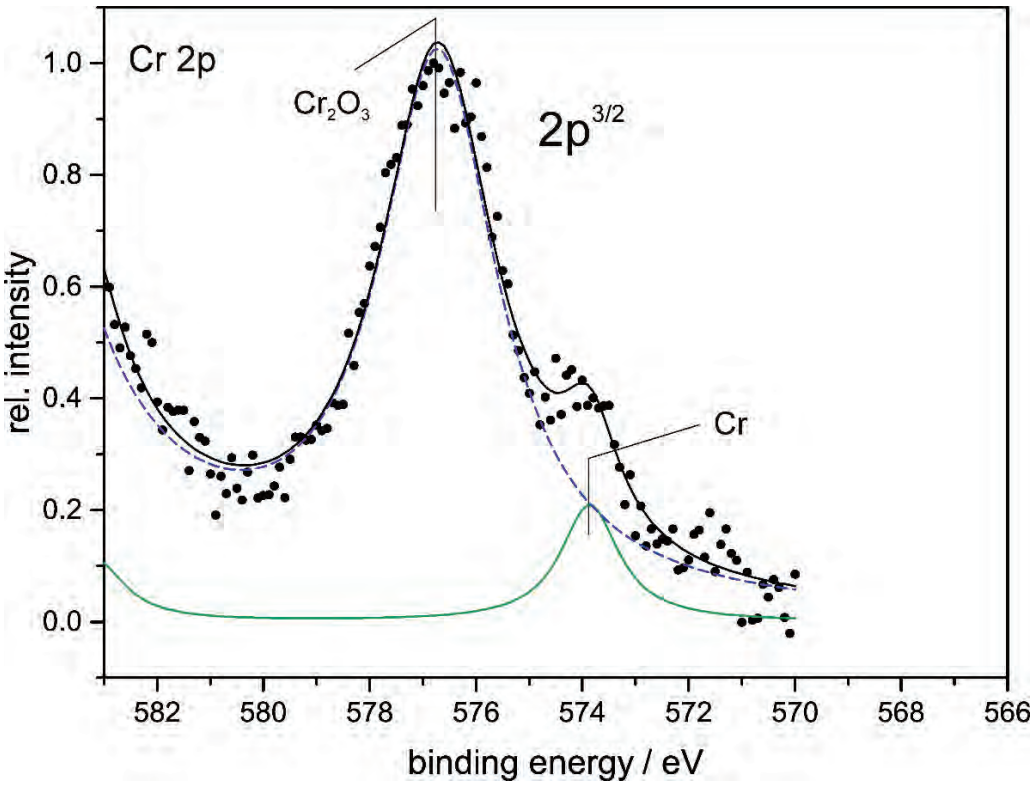

Fig. 5.17 Cr 2p core level spectrum for the surface outside corroded area after the anodic polarization 6 shown in Fig. 3.17 in Q3 solution at 80 °C and 50 bar

The Cl 2p signal measured outside the pit indicates that chloride is also present at the oxide film around the attacked region. The large scattering of the signal let fit the data with just only one line at 198.5 eV. According to /NIS 2012/ this binding energy corresponds to that for NaCl. Inasmuch as no rests of NaCl crystals could be observed on SEM images, the assignment of this signal is somewhat difficult.

6 Temporal corrosion experiments

The low voltage scan shown in Fig. 6.1 indicates a continuous stochastic breakdown-repassivation process accounted by frequent current spikes. The frequency of them decreases with current level. It is interesting to note, that the process seems to be independent of the potential scan. This fact suggests that some kind of stability of the passive layer is acquired with time.

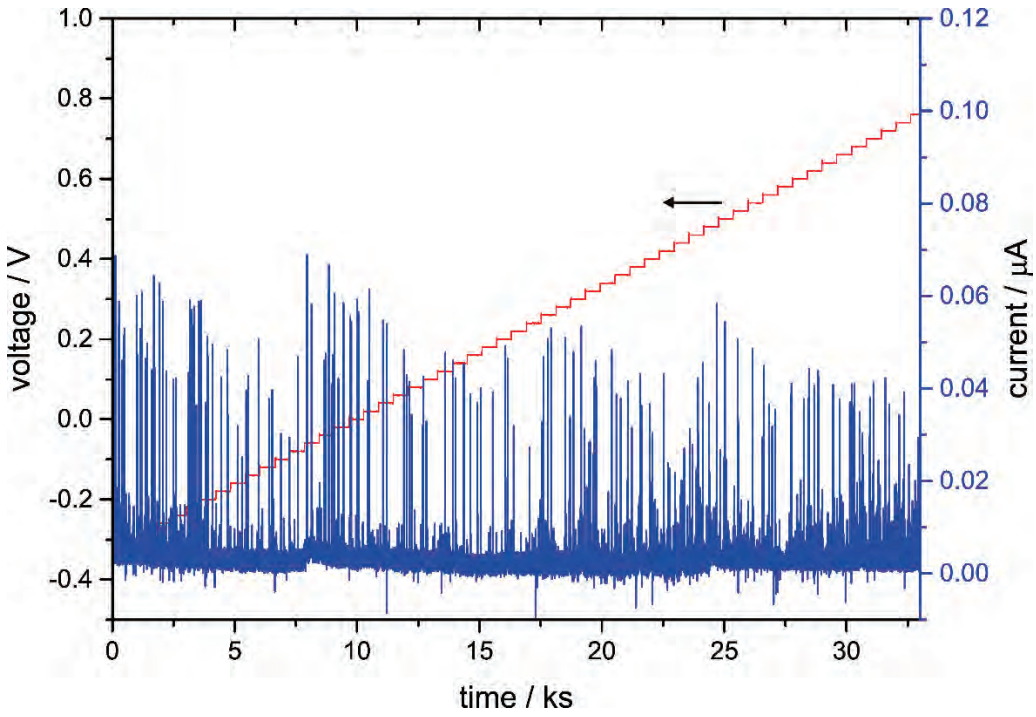

Fig. 6.1 Temporal evolution of current with a slow staircase voltage scan (step: 20 mV each 10 min) of 309S steel in Q3 solution at 30 °C and 5 bar. V_i = OCP (open circuit potential)

The temporal behavior of current changes drastically at 80 °C as shown in Fig. 6.2. It can be observed that the anodic dissolution of steel is activated as the voltage is set higher than 0.073 V. This value, however, is more positive than the mean breakdown potential observed in the cyclic polarization experiments: V=-0.25 V, see Fig. 3.2. This indicates that some repassivation is favored by a long time resting at potentials sufficiently cathodic respective the breakdown potential. The current pattern is characterized by a tooth-like course with superposed current spikes without a clear dependency of voltage. The square oscillations of current are probable caused by a modulation of the dissolution process by the formation of a regulating salt film.

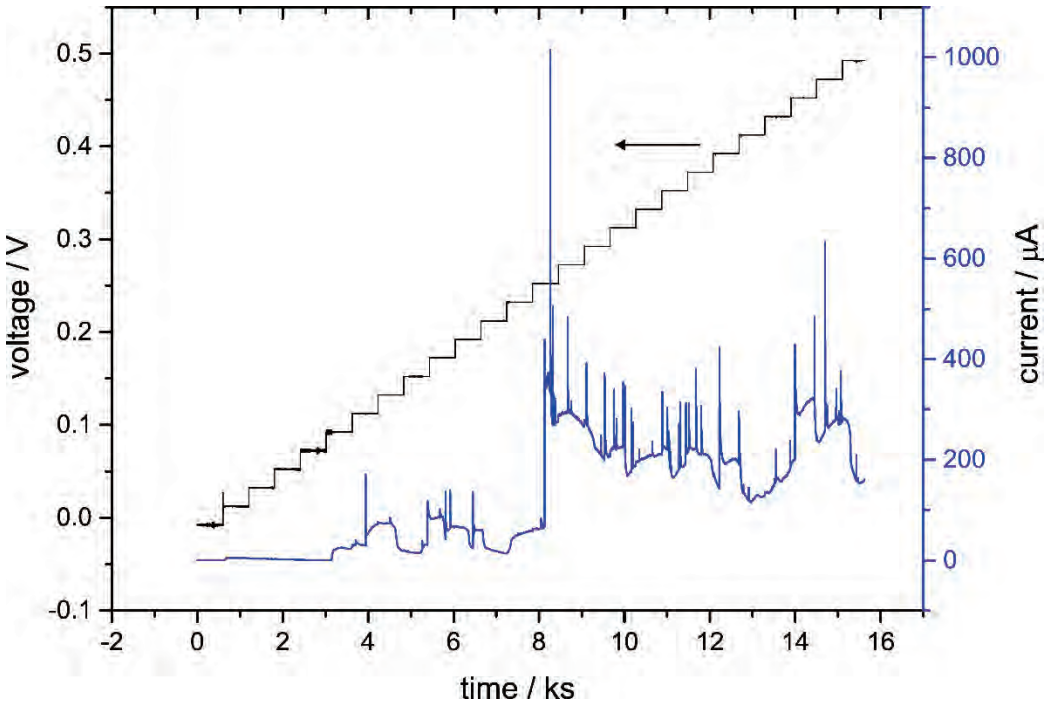

Fig. 6.2 Temporal evolution of current with a slow staircase voltage scan (step: 20 mV each 10 min) of 309S steel in Q3 solution at 80 °C and 5 bar. V_i = OCP (open circuit potential)

Fig. 6.3 shows the temporal evolution of the corrosion potential (OCP) of 309S steel at the extremes of the investigated temperature and pressure ranges. It can be noted, that very different courses appear for several samples with identical preparation. This is a consequence of the stochastic nature of the localized attack and the large influence of surface defects on the passivity of the surface. At low temperatures, the OCP reaches values between 0.2 V and 0.3 V in one of the samples, indicating a clear passivity. In another sample, this tendency is interrupted by an OCP decrease to -0.2 V, thus indicating an activation of the surface by formation of pits. Nevertheless, there is a clear tendency of them to repassivate, driving the OCP again in the passive region. At 80 °C, the OPC decreases to the activation region and no sign of repassivation can be discerned. Different samples differ only in the course form. In addition, no clear influence of pressure can be observed at this temperature.

Fig. 6.4 and Fig. 6.5 show different SEM images of the surface of two samples of steel after their immersion in Q3 solution at 80 °C and 5 bar during 24 h (they correspond to the green curves in Fig. 6.3). Contrasting Fig. 6.4 with Fig. 6.5, it is evident that the different temporal evolution of the OCP is reflected in the morphology and chemistry of the attack.

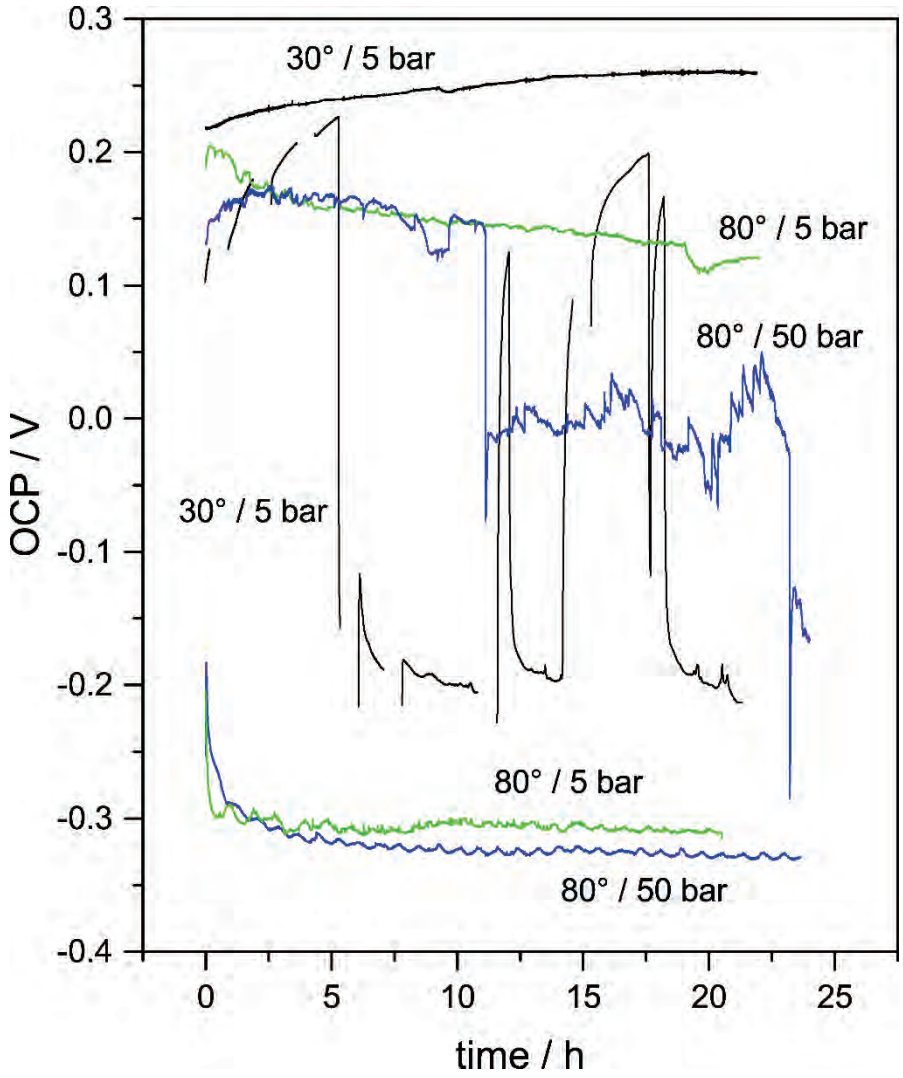

Fig. 6.3 Temporal evolution of the open circuit potential (OCP) of 309S steel in Q3 solution at different temperatures and pressures

In both cases, the low magnification SEM images in Fig. 6.4a with Fig. 6.5a show the presence of pits. But a higher density of them is observed in Fig. 6.5). It can be noted that they appear along the polishing lines (see Fig. 6.4b). In the case of Fig. 6.5b, the rather large amount of accumulated corrosion products does not let distinguish the substrate.

The SE (secondary electron) SEM image shown in Fig. 6.4c lets discern a rather homogeneous film on which small platelets can be distinguished. The surface of the sample shown in Fig. 6.5 is characterized by the presence of corrosion film on which snow-like deposits are dispersed (see Fig. 6.5d and f). The presence of an underlying fractured film indicates that it consisted in a highly hydrated product.

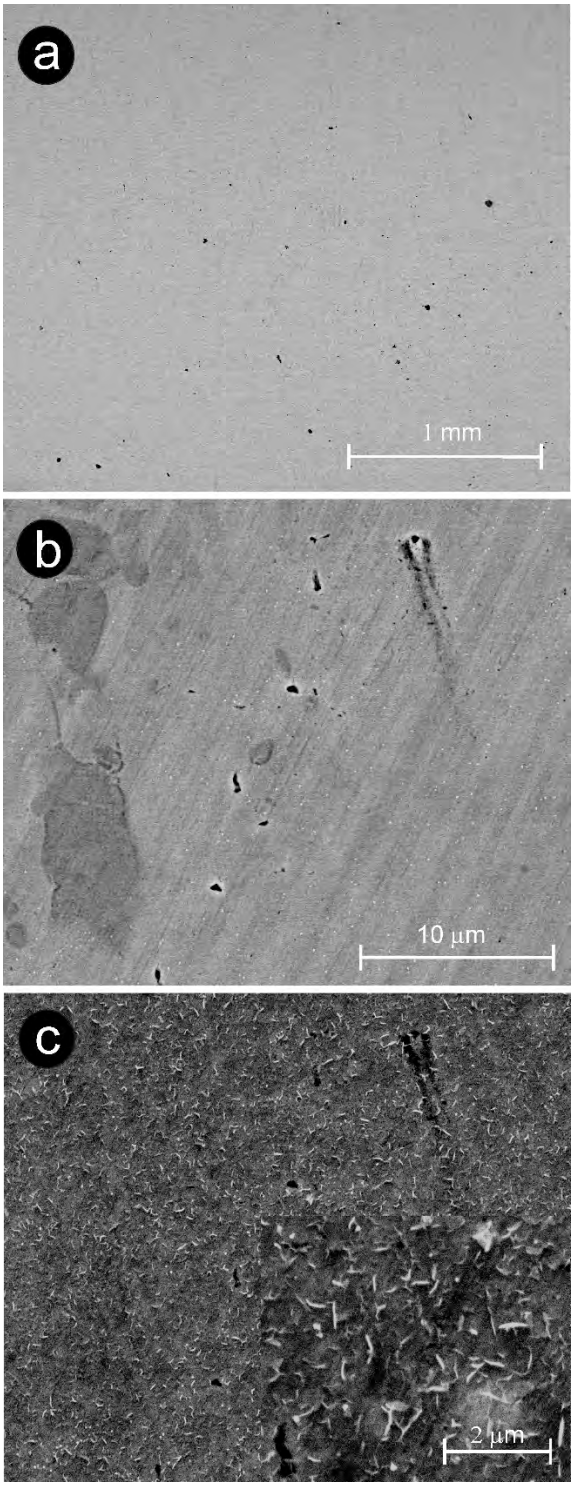

Fig. 6.4 SEM images at different scales showing the surface of 309S steel after immersion in Q3 solution at 80 °C and 5 bar during 24 h. a) and b) height mode; c) secondary electron (SE) mode

Fig. 6.5b shows the presence of some white appearing areas. Fig. 6.5c and e show a magnification of them, where it can be seen, that the center consists of a spot free from corrosion products. A concentric radial area around the central spot with exclusion of the

snow-like deposits can be distinguished. This is characterized by a particulate, rather closed deposit.

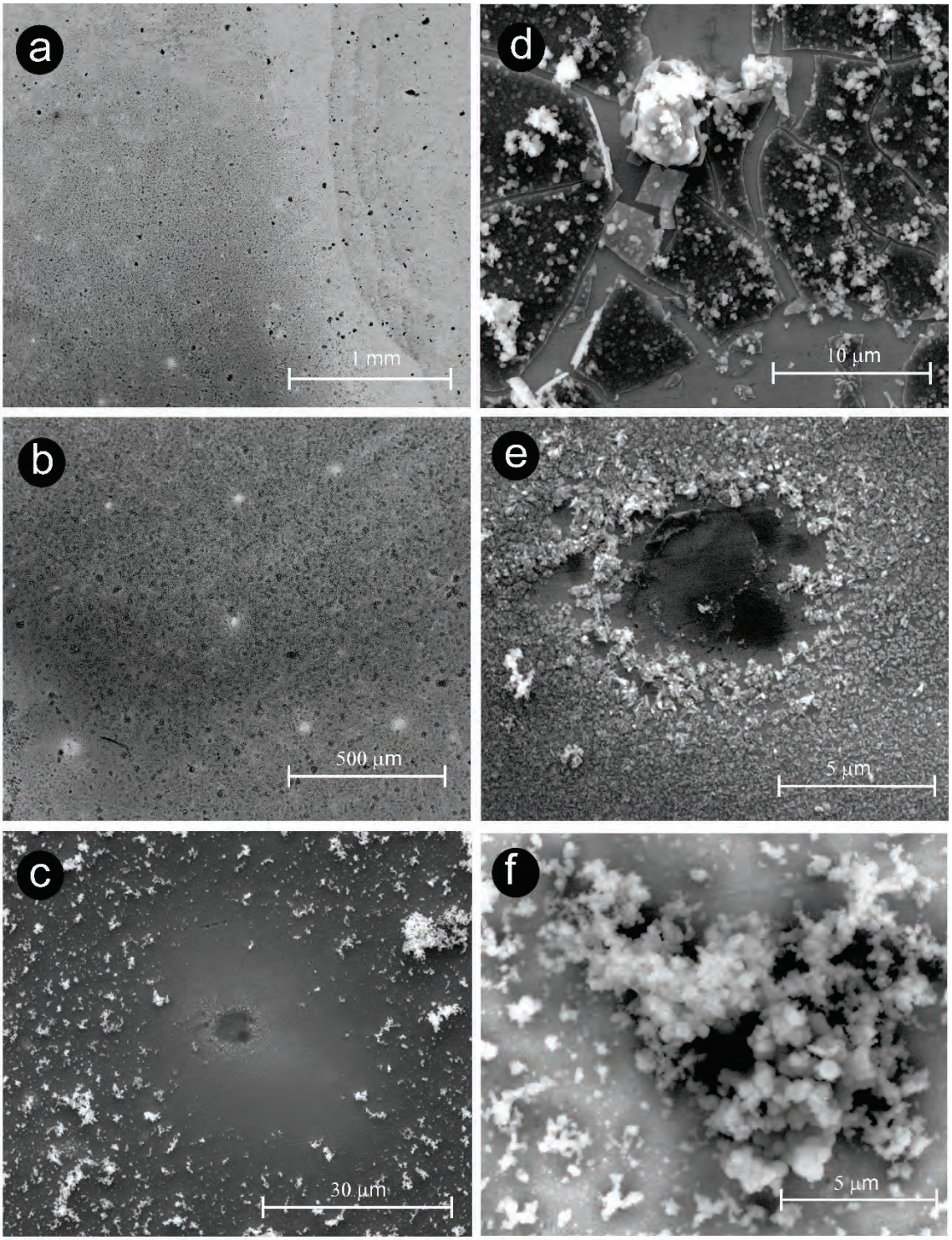

Fig. 6.5 SEM images at different scales showing the surface of 309S steel after immersion in Q3 solution at 80 °C and 5 bar during 24 h. a) and b) height mode; c), d), e) and f) secondary electron (SE) mode

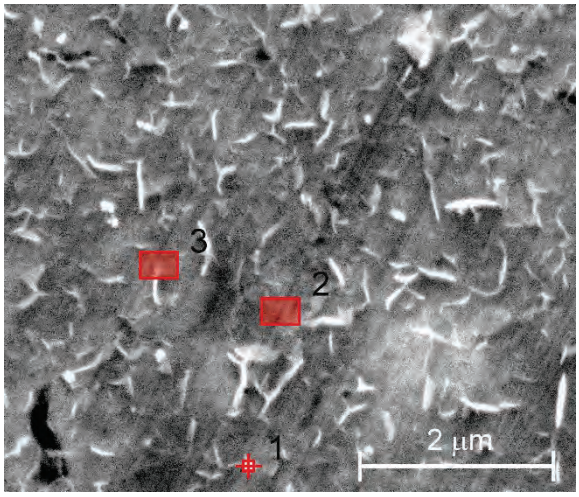

element	O-Kα	Mg-Kα	Si-Kα	S-Kα	Cr-Kα	Mn-Kα	Fe-Kα	Ni-Kα	Mo-Lα
point 1	11.1 ±2.2	1.0 ±0.2	0.8 ±0.1	1.2 ± 0.3	21.6 ±0.6	1.1 ±0.3	51.1 ±1.1	10.1 ±1.0	
point 2	13.3 ±0.9	0.9 ±0.2	0.7 ±0.2	-	21.5 ±0.7	1.2 ± 0.4	51.9 ± 1.3	10.4 ±1.2	
point 3	7.2 ±4.3	1.0 ±0.2	1.0 ±0.1	-	30.9 ±0.5	-	53.5 ±1.0	6.2 ± 0.7	0.2 ± 0.1

Tab. 6.1 Surface elemental composition (at %) at different points of the corroded 309S steel in Q3 solution at 80 °C and 5 bar after 24 h, obtained by EDX

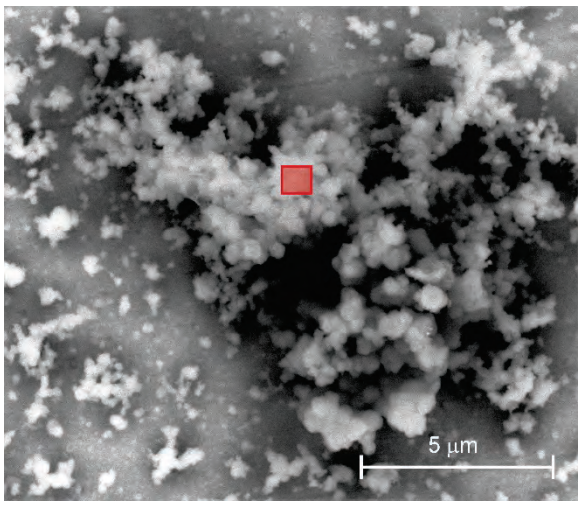

O-Kα	Na-Kα	Mg-Kα	Si-Kα	S-Kα	Cl-Kα	Ca-Kα	Cr-Kα	Fe-Kα	Ni- Kα
58.4 ±1.3	1.1 ±0.5	4.8 ±0.4	0.6 ± 0.1	2.1 ±0.1	1.1 ±0.3	0.4 ±0.1	7.0 ±0.3	21.4 ±0.8	2.8 ±0.7

Tab. 6.2 Surface elemental composition (at %) at snow-like corrosion deposit on 309S steel in Q3 solution at 80 °C and 5 bar after 24 h, obtained by EDX

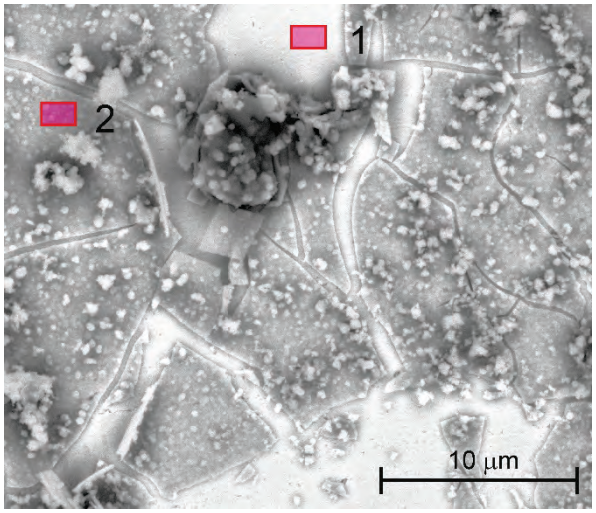

element	C-Kα	O-Kα	Si-Kα	S-Kα	Cl-Kα	Cr-Kα	Mn-Kα	Fe-Kα	Ni-Lα
point 1	9.6 ±1.6	-	0.8 ±0.2	-	-	22.6 ±0.9	1.3 ±0.5	54.6 ±1.8	11.0 ±1.6
point 2	-	25.0 ±0.5	0.6 ±0.1	0.6 ±0.1	0.5 ±0.1	21.3 ± 0.5	0.9 ± 0.3	43.1 ±1.0	7.9 ±0.9

Tab. 6.3 Surface elemental composition (at %) at different sites on the corroded area of 309S steel immersed in Q3 solution at 80 °C and 5 bar after 24 h, obtained by EDX

The relative high concentration of O in point 1 and 2 listed in Tab. 6.1 indicates the presence of a surface oxide. Taking the basic atomic relation for the alloy bulk Cr/Ni: 1.930 and Fe/Ni: 4.662 and assuming that Ni is not part of the oxide, we can subtract the part of Cr and Fe signals arising from substrate:

%at M(oxide) = %at M (total) - (M/Ni) at% Ni (6.1)

Following this reasoning, we obtain a concentration of at% Cr: 2.1 and at% Fe: 4.0, which for the assumed composition of $Cr(OH)_3$ + Fe_2O_3 yields a concentration of at% O 12.5, very close to that calculated from quantitative EDX. With the same procedure, a composition of at% Cr 18.9 and at% Fe 24.5 for point 3 can be calculated. Thus, these small particles could be ascribed to released σ-phase.

The elemental composition obtained on the snow-like deposits shown in Tab. 6.2 can be interpreted in terms of a mixed oxide constituted by $Cr(OH)_3$ + Fe_2O_3 + $Ni(OH)_2$. The presence of Na, Ca, Cl and S signals, is an evidence of the presence of some rests of salt retained in the formed oxide.

The relative high concentration of oxygen measured on the fragmentary film observed in Tab. 6.3 (point 2) let identify it with an oxide film. Subtracting the signal of the underlying bulk by eq. (6.1), a composition of at% Cr: 6.0 and at% Fe: 6.1 is obtained. Thus, the at% O calculated assuming a mixed oxide $Cr(OH)_3$ + Fe_2O_3 is close to that measured. The uncovered area (point 1) shows an elemental composition close to that of the bulk. Here, an interesting large amount of C appears, which otherwise is not seen in the oxide covered areas.

7 Impedance experiments

Impedance measurements were performed on surfaces after corrosion attack in order to obtain more information about the dissolution and repassivation process in the pits. But, before starting with the discussion of the results, it would be convenient to briefly review the fundamentals of this technique. This method consists in the application of an additional alternating voltage of amplitude ΔV and frequency ω over the polarization voltage V_0 on the corroding system: i.e. $V(t) = V_0 + \Delta V \sin(\omega t)$. Assuming a linear behavior of the system, the measured current response can be expressed as $j = j_0 + \Delta j \sin(\phi + \omega t)$, where j_0 is the polarization current. ϕ and Δj are the phase shift angle and the current amplitude respectively (see Fig. 7.1a).

The impedance of the system is defined as $Z(\omega)=V(t)/j(t)$ and can be expressed in a more convenient way as a vector given by (for more details see /MAC 1987/):

$$\boldsymbol{Z(w)} = \left(\frac{\Delta V}{\Delta j}\right) \boldsymbol{e^{j\phi}} = \left(\frac{\Delta V}{\Delta j}\right) \boldsymbol{\cos\phi} + \boldsymbol{i}\left(\frac{\Delta V}{\Delta j}\right) \boldsymbol{\sin\phi} = \boldsymbol{Z'(\omega)} + \boldsymbol{i}\, \boldsymbol{Z''(\omega)} \qquad (7.1)$$

where $(\Delta V/\Delta j)$ is the modulus and ϕ is the phase angle (see Fig. 7.1b). The vector can also be written as the complex number $Z' + i\, Z''$. The representation of the impedance as a Z'' vs. Z' plot is known as Nyquist diagram. The imaginary part is commonly shown as $-Z''$ to let appear the capacitance responses at the first quadrant of the diagram.

The electrochemical impedance behavior $Z(\omega)$ of a particular corroding system as that shown in (a) can be represented by an electric equivalent circuit as shown in Fig. 7.1c: this includes resistances, capacitances and complex impedance elements representing transport and adsorption processes. The anodic dissolution in the pits can be represented by a parallel R_aC_a circuit, describing the electron transfer reaction of a resistivity R_a occurring through the double layer of a capacitance C_a. This appears in the Nyquist diagram as a semicircle at high frequencies. At lower frequencies, the impedance is dominated by transport processes represented by the element Z_a. The part of the surface covered by the oxide can be also represented by a parallel $R_{oxide}C_{oxide}$ circuit that reflects the ionic current inside the oxide in the dielectric material. This behavior appears as a large semicircle as represented in Fig. 7.1e. The electric circuits for the pit (active area) and the oxide covered surface (passive area) are connected in parallel to the electrolyte resistance. In general, $R_{oxide} >> R_a$ and $C_{oxide} << C_a$. Therefore, as the total impedance is given by $Z_T = 1/(Z_a^{-1} + Z_{oxide}^{-1})$, the lower impedance will

dominate the total response and thus, the onset of pitting can be detected by the characteristic shape of the impedance diagram for the activated state.

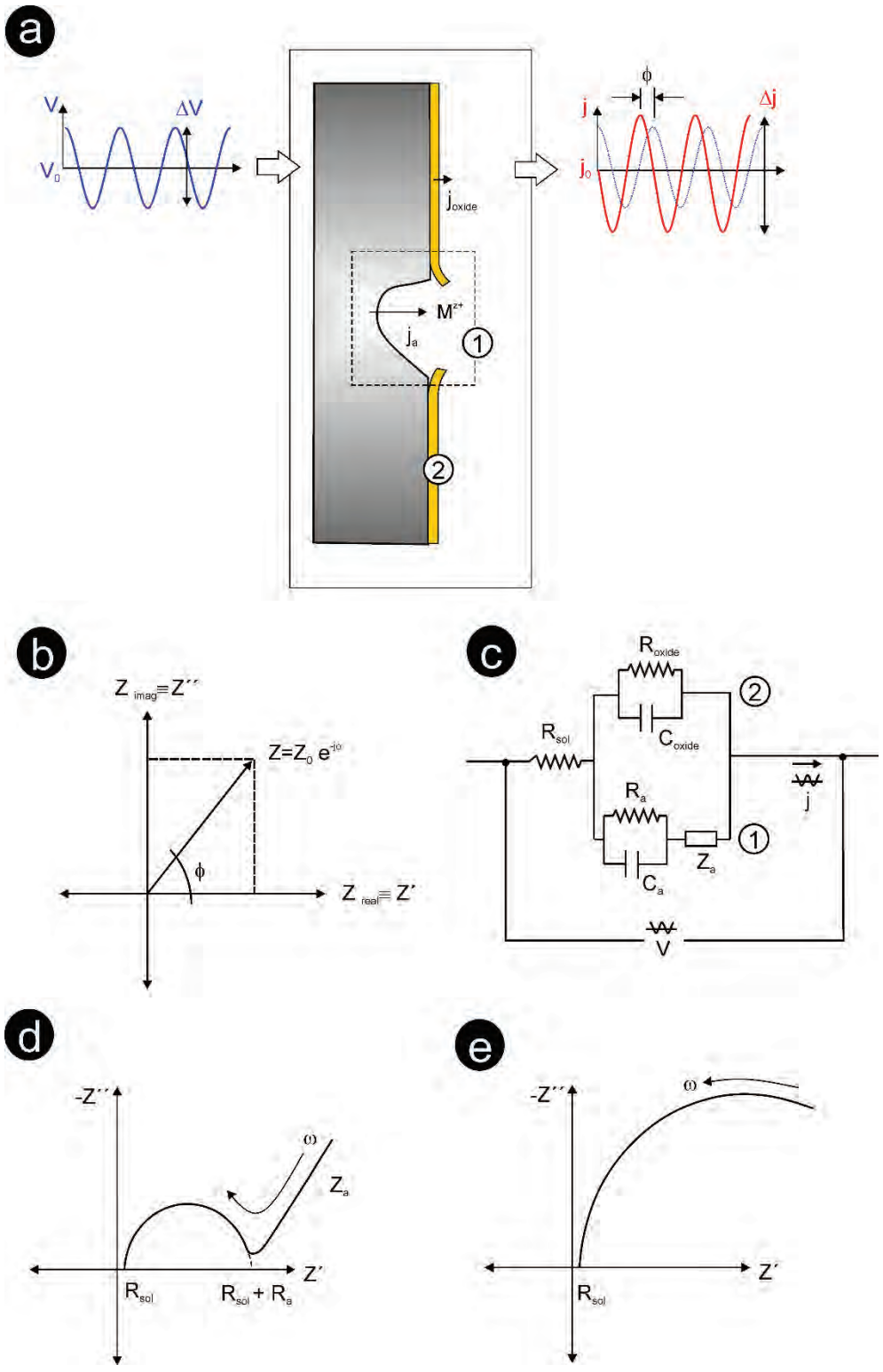

Fig. 7.1 Principle of the electrochemical impedance technique used here: see text

Fig. 7.2 shows a series of Nyquist plots measured after the cyclic polarization shown at the top-left corner of the figure. It can be seen, that at -0.25 V < V < -0.1 V, the impedance behavior can be represented by a parallel RC-circuit, characteristic for a passivated surface. Resistances of 200 kΩ and 140 kΩ can be estimated at -0.25 V and -0.2 V by an extrapolation of the semicircle to the real axis respectively. At -0.1 V, the resistance drops to about 6 kΩ. It can be noted that at low frequencies the resistance decreases from 6 kΩ to 2.3 kΩ by an almost constant imaginary Z´´ component. This effect can be ascribed to the slow expansion of the attacked area with time, made visible by the longer time intervals spent for measurements at low frequencies.

At voltages V > -0.1 V, the behavior of active pits is reflected. It is characterized by two Nyquist loops which can be described by two in series connected RC-units (parallel). The first one, at high frequencies describes the interfacial dissolution process. The second one, at lower frequencies describes the transport behavior controlled by corrosion precipitates. It can be seen, that at the low frequency limit, the second semicircle is distorted by a decrease of the real impedance Z´ towards lower values. This fact is again a consequence of the growth of the active area with time. The linear course at the beginning of the second loop following a relation $Z''/Z' \approx 1$ suggests a diffusion-controlled process (Warburg-type impedance).

Fig. 7.3 shows the Nyquist plots of 309S steel obtained at different voltages after a cyclic polarization at 80 °C. In this case a unique semicircle is denoting a parallel RC-circuit with a decrease of the electrode resistance at low frequencies. Unlike the impedance results at 30 °C, a second loop indicating a diffusion-controlled process is absent.

The impedance diagrams measured after a cycling polarization indicate in general that repassivated pits become again active and grow further as the potential is driven to values more positive than the repassivation potential. These observations support the assumption of the formation of a salt film on the pits, hindering the regeneration of the protective oxide.

Fig. 7.4 exemplifies the temporal modification of the real part of the impedance at low frequencies as 1/Z´ for the particular case of an experiment at -0.2 V performed after the cyclic polarization of 309S steel in Q3 solution at 80 °C and 6 bar as shown in Fig. 7.3. The value of Z´ attained at low frequencies corresponds to the polarization resistance $R_{pol} = (\partial J/\partial V)^{-1}$, i.e. the inverse of the slope of the current-voltage curve (J: electrode current). The polarization resistance is given by $R_{pol} = r_{pol} / A_{pit}$, where A_{pit} is the actual area of the pit. Since r_{pol} [Ω cm^{-2}] is a specific variable depending on the dissolution kinetics, the measured resistance R_{pol} is inversely proportional to the attacked area and thus, $1/Z´_{pol} \propto A_{pit}$.

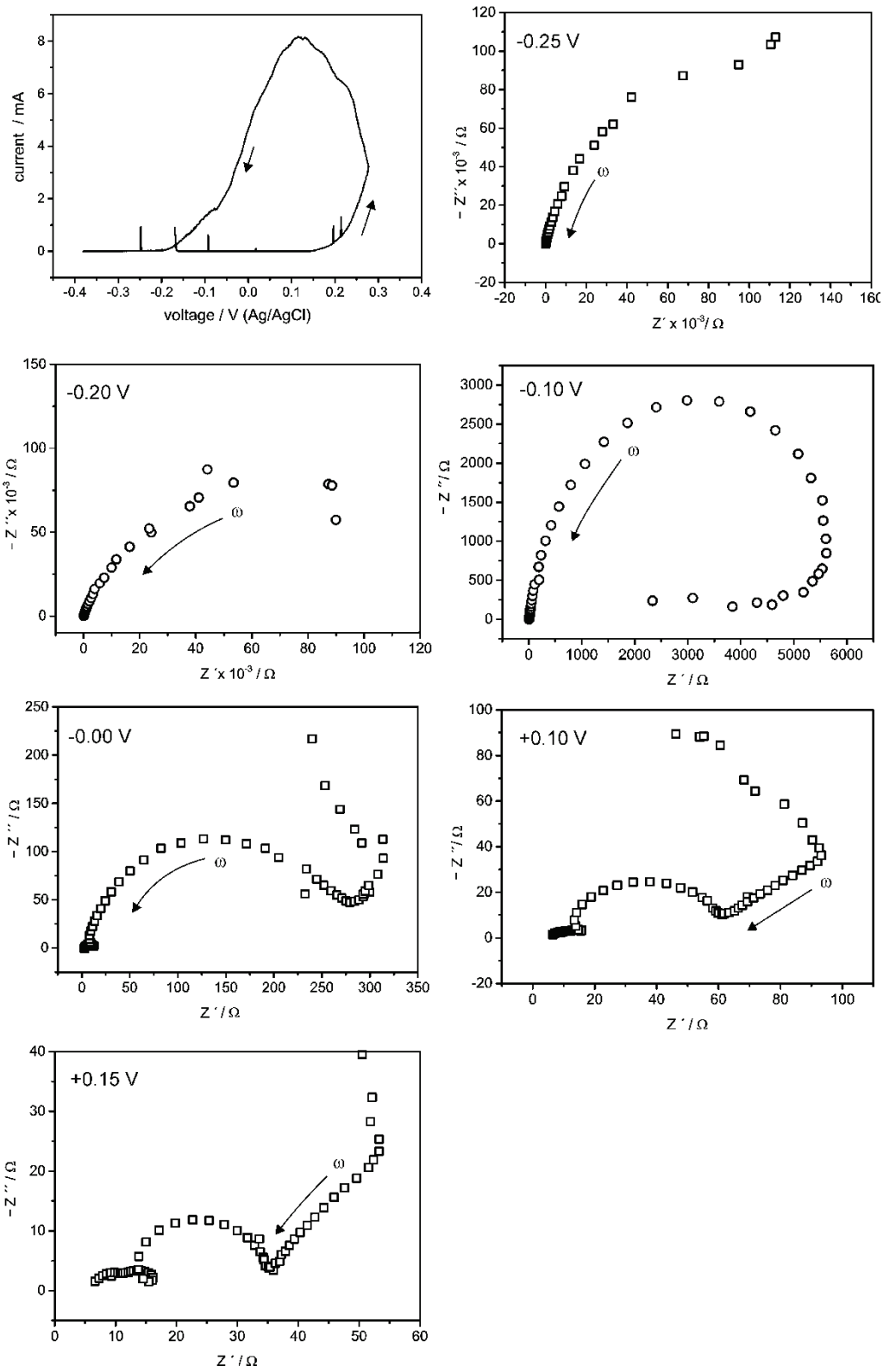

Fig. 7.2 Nyquist plots obtained at different potentials after a cyclic polarization of 309S steel in Q3 solution at 30 °C and p = 6 bar (current-voltage curve shown at the top-left corner: scan rate 1 mV s^{-1}). Frequency range: 1 MHz – 30 mHz. Amplitude: 10 mV

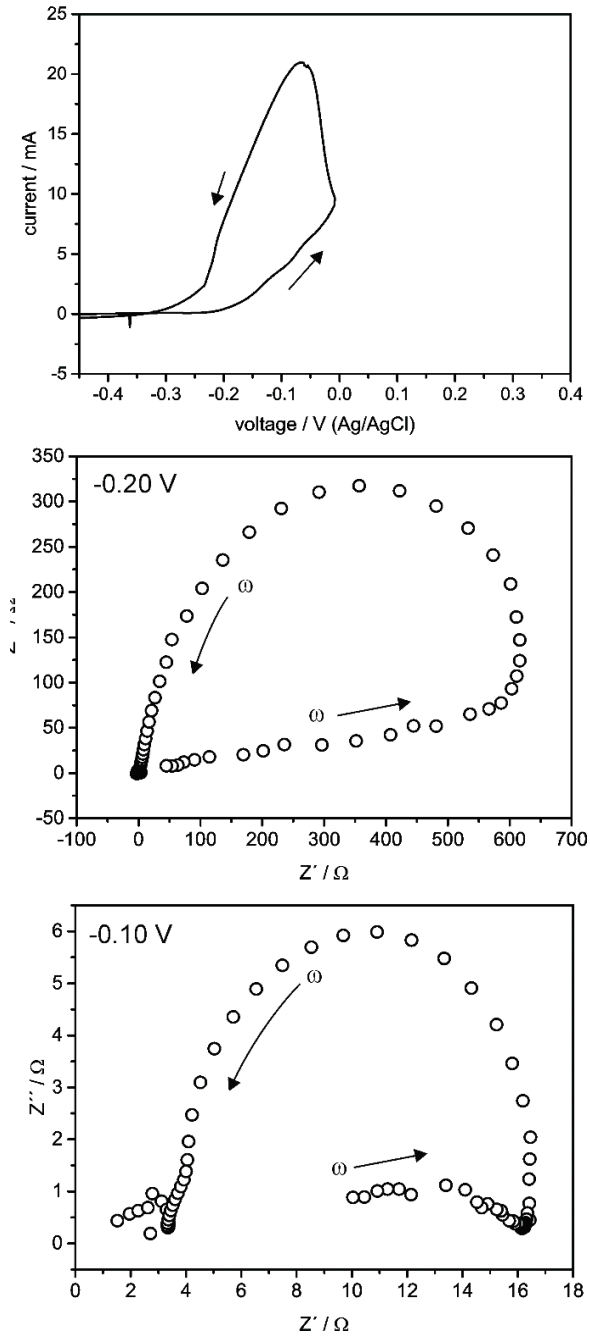

Fig. 7.3 Nyquist plots obtained at different potentials after a cyclic polarization of 309S steel in Q3 solution at 80 °C and p = 6 bar (current-voltage curve shown at the top-left corner: scan rate 1 mV s^{-1}). Frequency range: 1 MHz – 30 mHz. Amplitude: 10 mV

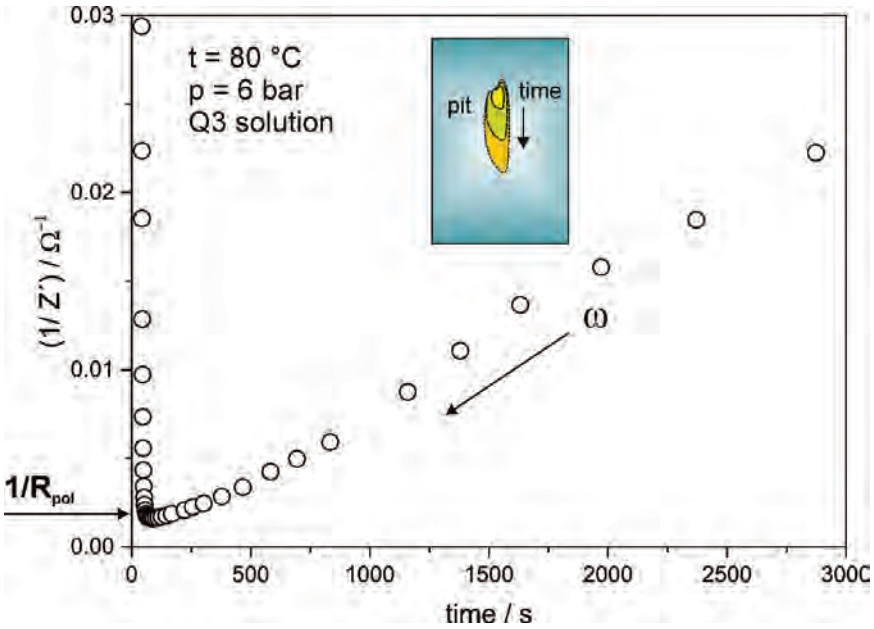

Fig. 7.4 Exemplary temporal variation of the inverse of real impedance at the low frequency region measured at -0.2 V after a polarization cycle as shown in Fig. 7.2

The shape of the Nyquist loop allows identifying the passive or active state of the surface as shown for instance in the temporal variation of the corrosion potential in Fig. 7.5. The voltage-time curve shows that the circuit potential oscillates between an anodic potential region of +0.2 ± 0.05 V and a cathodic one of -0.2 ± 0.05 V. The former corresponds to a passive surface state which is characterized by a unique semicircle with a large polarization resistance (a, b and c). As the surface is driven in the active potential region, the Nyquist diagrams show a closing of the loops with a polarization resistance of some kΩ with decreases along the Z´-axis at the low frequency region. This, in turn, is a clear indication of the growth of the attacked area.

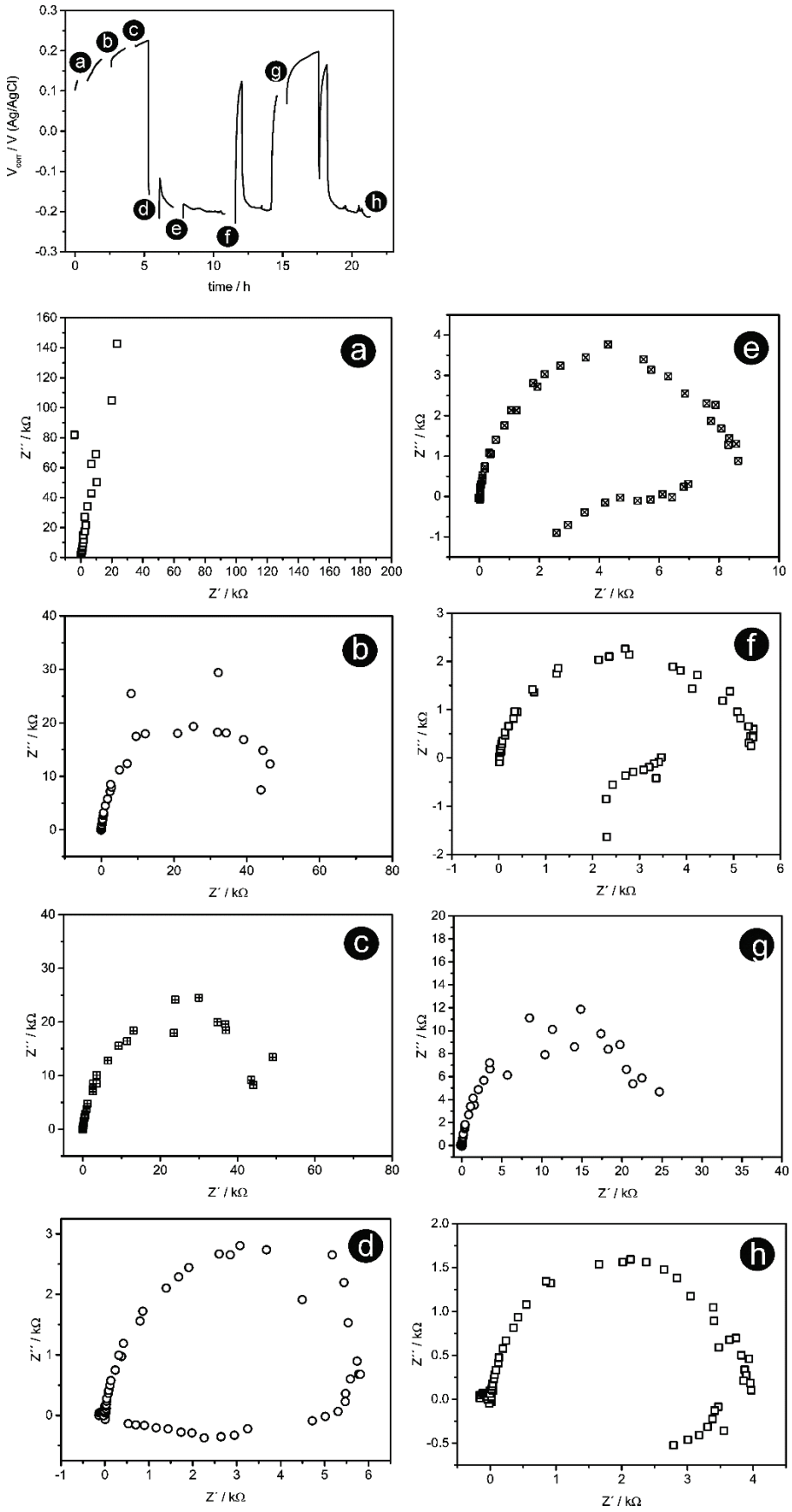

Fig. 7.5 Nyquist plots performed at the corrosion voltage at regular time intervals withing a 24 h test in Q3 solution at 30 °C and 6 bar

8 Synchrotron photoelectron spectroscopy experiments

The aim of these experiments is to obtain an overview of the surface chemical changes triggering the initiation of the metal dissolution at localized sites and the subsequent grows of the corroded surface. In this sense, the surface distribution of alloying elements Cr, Ni and Mo and their chemical states in the surface oxide define the susceptibility to the breakdown of the passive state assisted by chloride /BAR 2014/, /REN 2007/, /MCI 2003/, /NAT 2002/, /KAG 2003/.

The first stages of the passive-active transition of stainless steel 309S in standard representative geological brines Q3 and Q2 was investigated in an electrochemistry cell made of glass, which is directly attached to the SoLiAS and flooded with N2 to avoid additional contamination (in-system approach). Fig. 8.1 shows a layout of the cell. Electrochemical experiments consisted of low polarization scans of mechanically mirror-polished samples of stainless steel AISI 309S. The sample was introduced in the cell and brought face down in contact with electrolyte to form a meniscus. The potential scan was stopped after each of the polarization points to capture the surface changes during the passive-active transition. After electrochemical runs, samples were washed with deaerated water and dried with a nitrogen stream. The sample was transferred to the measuring UHV chamber through a buffer chamber flooded with nitrogen. Spectroscopic measurements based on synchrotron radiation SR-PES were performed using tunable x-rays as provided by BESSY II. The UHV analysis system SoLiAS has been recently modified for an easy attachment to the UE56-2/PGM-1 beamline operated in the energy range from 60 to 1200 eV. This allows to adjust the surface sensitivity to distinguish between surface or more bulk related effects which can be only done at the synchrotron BESSY II. The high energy resolution of the SR-PES technique allows a better deconvolution of core level spectra of the alloy elements and a more precise identification of surface corrosion products. This is particularly important for iron, since closely overlapping spectral lines cannot be adequately deconvoluted in spectra obtained by conventional XPS equipment. The SoLiAS end-station is designed to combine both, analysis and preparation within an in-system approach that allows performing SR-PES and electrochemistry experiments without exposure to ambient oxygen (see Fig. 8.2).

The surface chemical investigations are complemented with spatially resolved spectroscopic measurements at the X-PEEM-Microscope attached to the UE49_PGM-beamline. This surface technique, with a spatial resolution of 30 nm is an ideal tool for resolving the metallographic micro-structure. The field-of-view of PEEM facility can be

varied from 25 μm to 3 μm, which matches with the average dimensions of grains. Samples have been prepared following the same sequence as that applied in the SoLiAS-experiments. This technique allows connecting the surface chemistry, as previously investigated in the SoLiAS facility, with lateral micro-structure by its element selective investigation by means of chemical maps (XAS) at different stages of the passive-active transition. The microscope is equipped with a docking system that allows the transfer from the electrochemical cell to the microscope in an anoxic atmosphere.

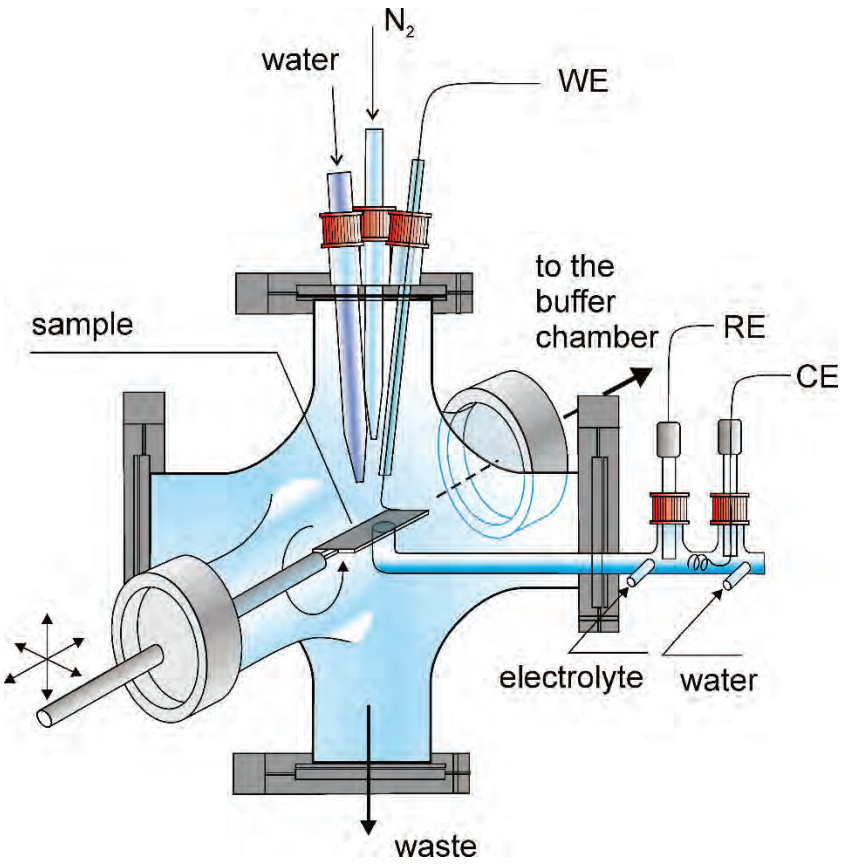

Fig. 8.1 Schematic representation of in-system cell used for corrosion experiments at SoLiAs equipment

Fig. 8.3 shows the Fe 2p core level spectra taken before and after the electrochemical polarization. As already shown in Fig. 5.7, the iron spectrum can be deconvoluted using 5 components. The asymmetry of the Fe metal line was left free in the fitting process. Before the corrosion experiment, the component lines appear at 707.21 eV, 709.52 eV and 711.09 eV. They can be assigned to Fe metal, FeO and Fe_2O_3/Fe(OH)O respectively. The lines at 713.91 and 718.30 eV correspond to the satellites for Fe(II) and Fe(III) respectively. The intensity relation $I(Fe_2O_3)/I(Fe)$ is 1.17.

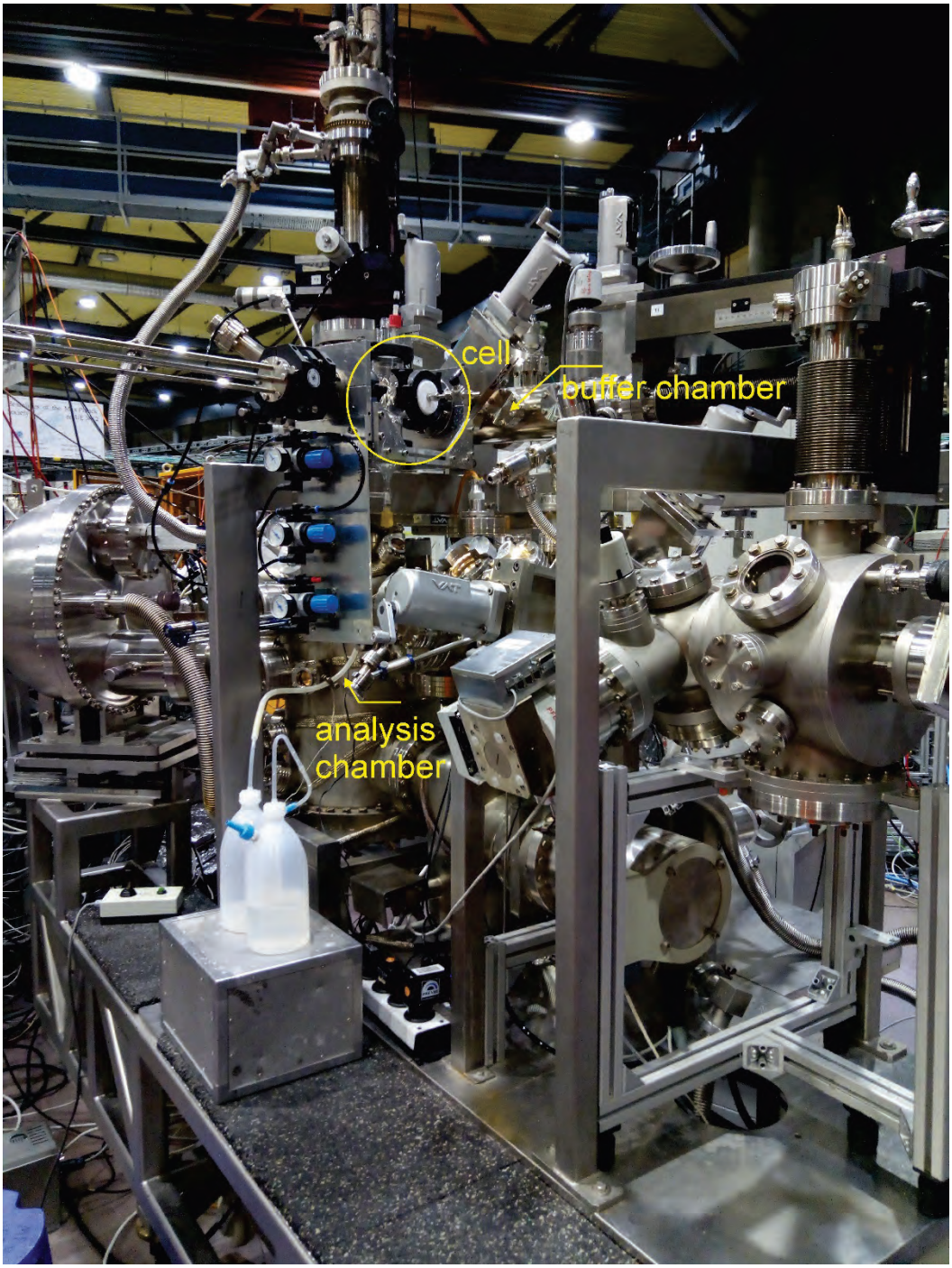

Fig. 8.2 Photography showing the SoLiAS equipment at Bessy II, Adlershof, Berlin

The deconvoluted Fe2p core level spectrum after the anodic polarization shows a very similar composition as before. But the peaks of Fe_2O_3 and FeO show a shift ΔE: -0.47 eV and a relation I(Fe_2O_3)/I(Fe) of 0.99. The ratio I(Fe_2O_3)/I(FeO) is 3.64 before and after the corrosion experiment.

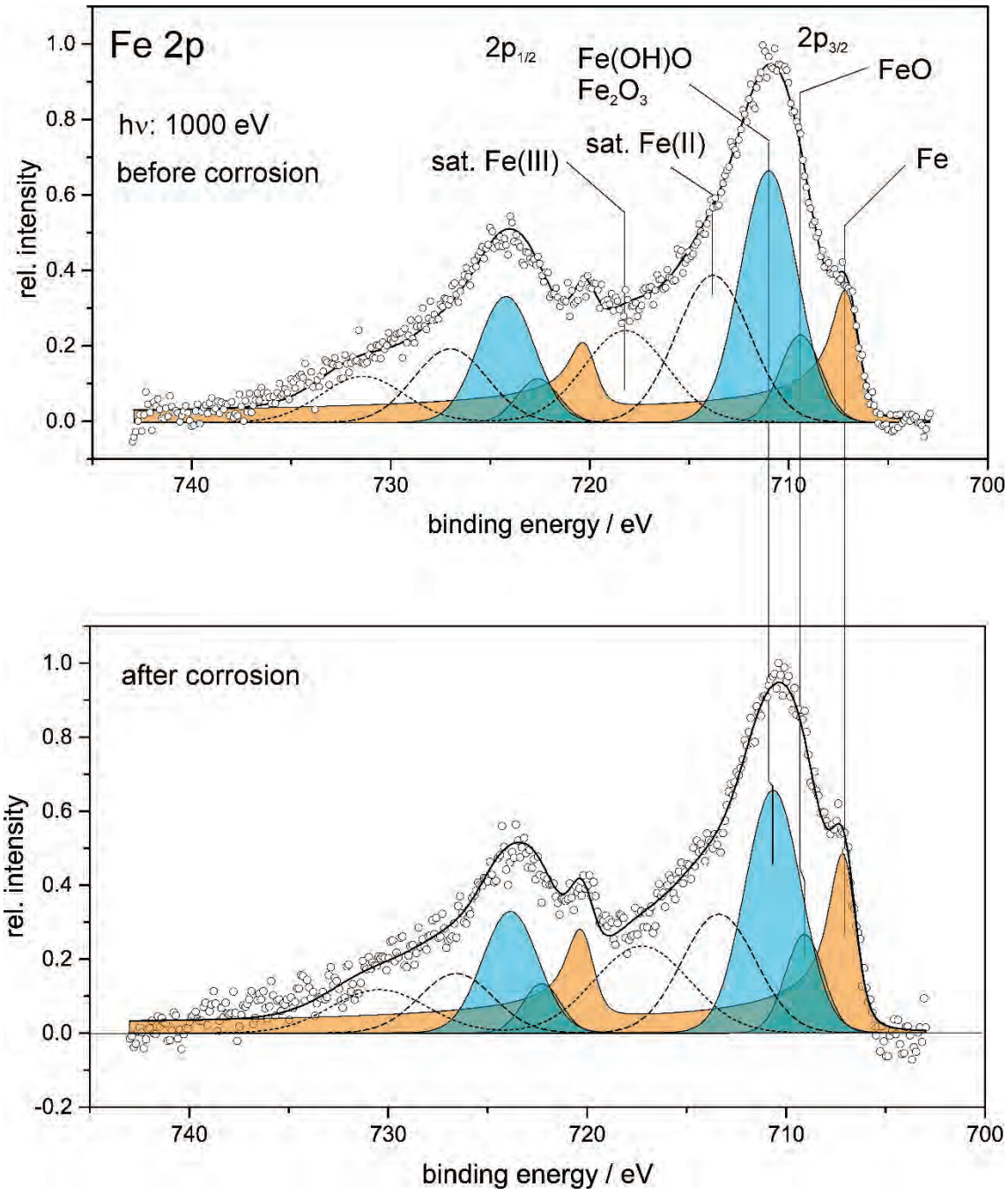

Fig. 8.3 Fe 2p core level spectra of the 309S surface before and after the polarization experiment. Excitation energy: 1000 eV

The shift of oxide peaks cannot be explained in terms of charging effect since that for the peak of metal Fe remains unchanged. This change should rather be a consequence of structural changes in the oxide. This is reflected in the change of the FWHM (full width at half maximum) of the Gaussian distribution from 2.34 and 3.19 for FeO and Fe_2O_3 respectively before corrosion to 1.98 and 2.91 after corrosion. Thus, the reduction of the degree of structural disorder and the increase of the metal signal let infer a partial dissolution of the oxide with a preferential attack of the stressed bonds.

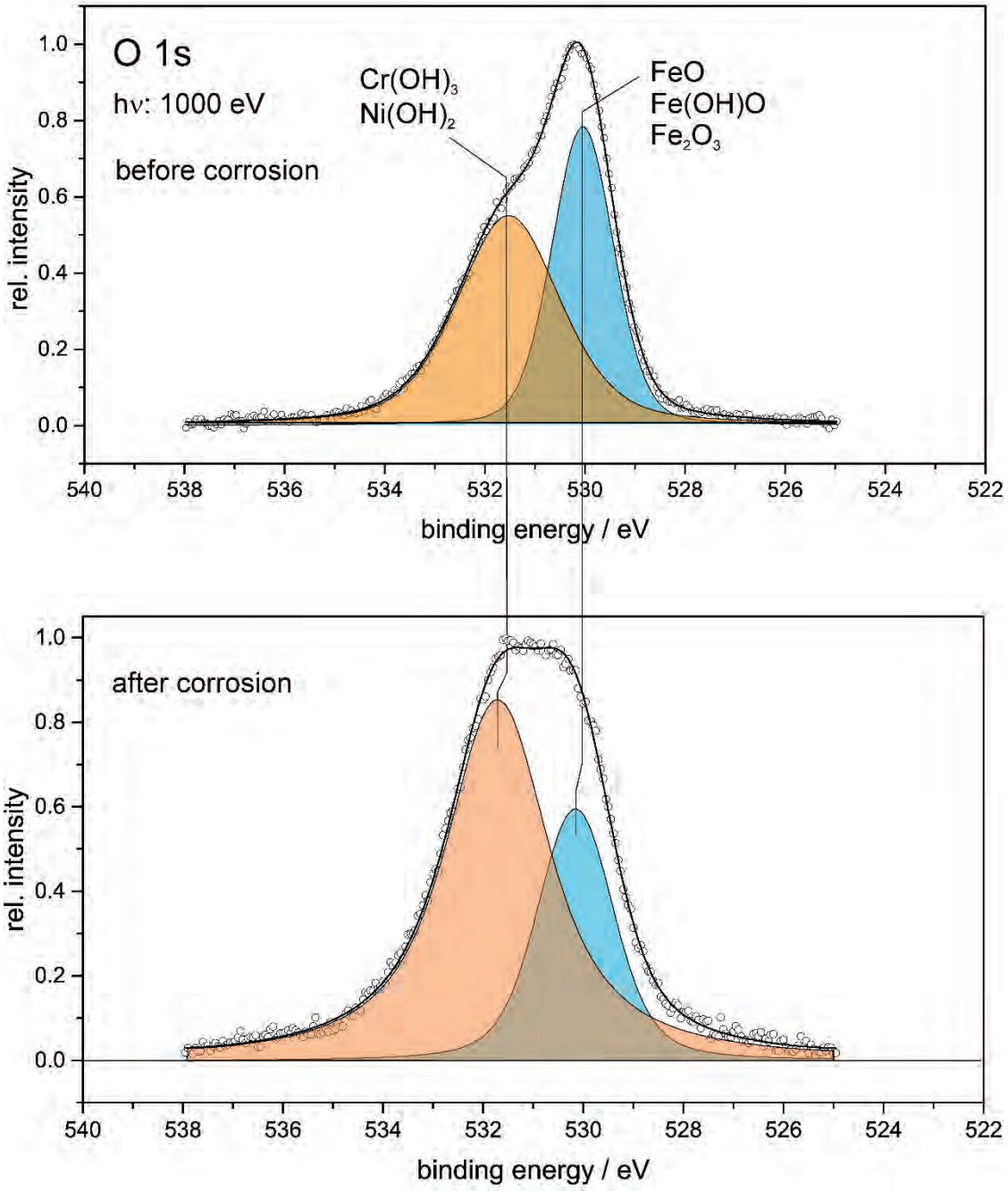

Fig. 8.4 O 1s core level spectra of the 309S surface before and after the polarization experiment. Excitation energy: 1000 eV

Fig. 8.4 shows the changes of the O 1s core level signal for hν:1000 eV. The signal can be deconvoluted in two components. Before corrosion, these are at 531.57 eV and 530.05 eV and can be ascribed to Cr-hydroxide and Fe-oxides respectively. The assignment to Ni-hydroxide is indicated for the sake of completeness, because the Ni 2p signal is very weak, as seen later. After corrosion, a shift ΔE of about +0.2 eV is observed. This is rather related to a change of bonding structure than to changes of the

chemical environment of oxygen. It is interesting to note, that the ratio of $I_{Cr\text{-}hydrox.}$ / $I_{Fe\text{-}oxides}$ changes from 0.81 to 2.24 during the anodic polarization. This indicates a growth of the oxide film by oxidation of Cr.

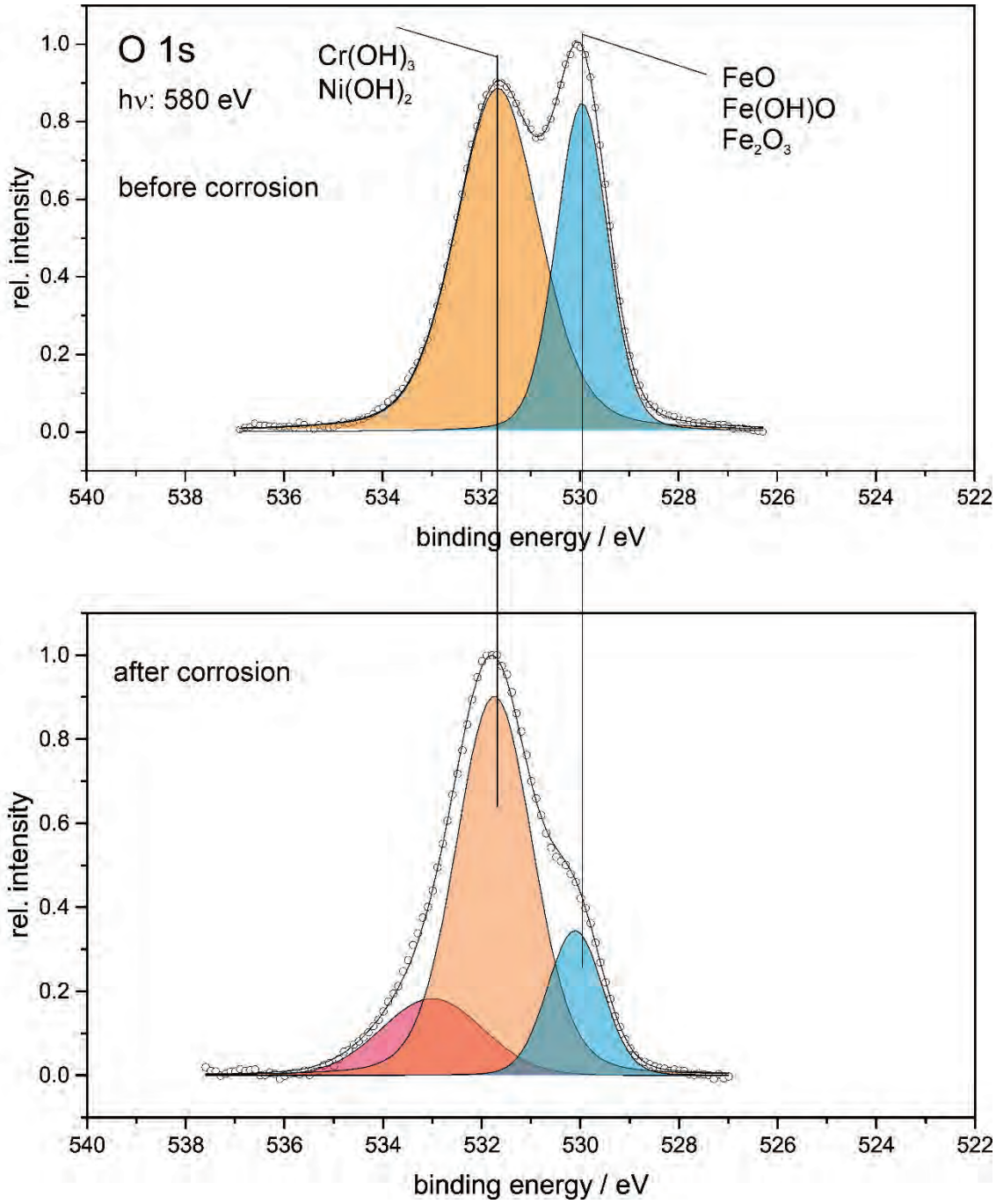

Fig. 8.5 O 1s core level spectra of the 309S surface before and after the polarization experiment. Excitation energy: 580 eV

Fig. 8.5 shows the O 1s core level signals before and after the anodic polarization at hν = 580 eV. A kinetic energy of excited electrons of about 48 eV ensures a maximal surface sensitivity /SEA 1998/ and the obtained information corresponds to the

outermost atomic layers of the oxide film. The signal before corrosion can also be deconvoluted in two lines assigned to Cr-hydroxide and Fe-oxides. The intensity ratio of Cr-hydroxide to Fe-oxide increases from 1.74 to 3.74 after the corrosion process. After anodization, a third line appears at 533.00 eV. This can be ascribed to water bounded to the oxide film.

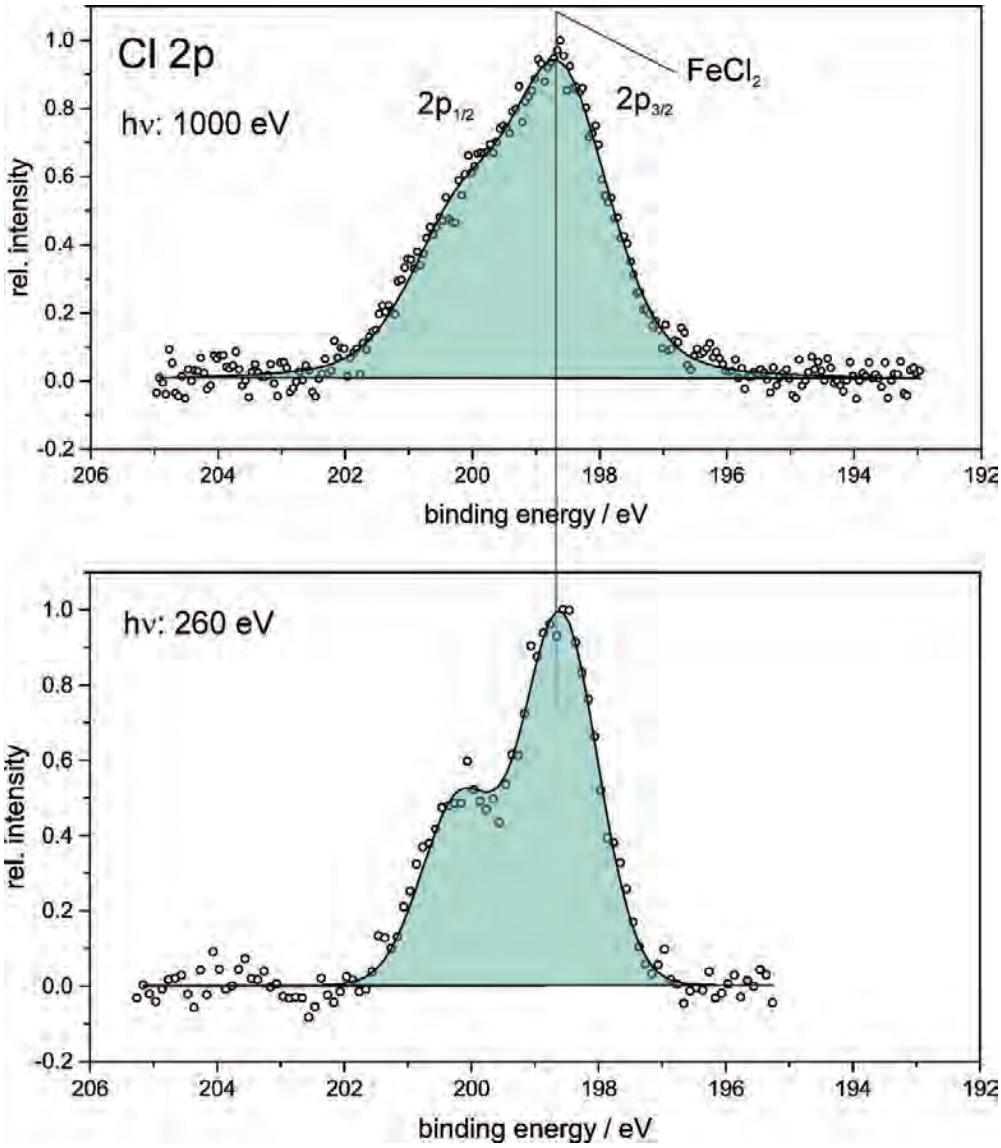

Fig. 8.6 Cl 2p core level spectra of the 309S surface after the polarization experiment at different excitation energies

The Cl 2p core level signal shown in Fig. 8.6 clearly indicates penetration of chloride into the oxide film after the anodic polarization. The $2p^{3/2}$ line appears at 198.62 eV. According to the NIST data base /NIS 2012/ this signal can be assigned to $FeCl_2$. This binding energy also matches with that assigned to NaCl. This, however, seems to be improbable, since the sample was abundantly rinsed with pure water after the

polarization experiment. At this point, it is important to note, that the chemical shift of the element signal reflects its chemical environment. Thus, the signal could arise from the Fe-Cl bonds formed in the oxide. The signal at hν: 1000 eV provides information about the bulk of the thin oxide film whereas that at hν: 260 eV, just only from the outermost part of it. Thus, the broader peak at hν: 1000 eV indicates a higher structural disorder.

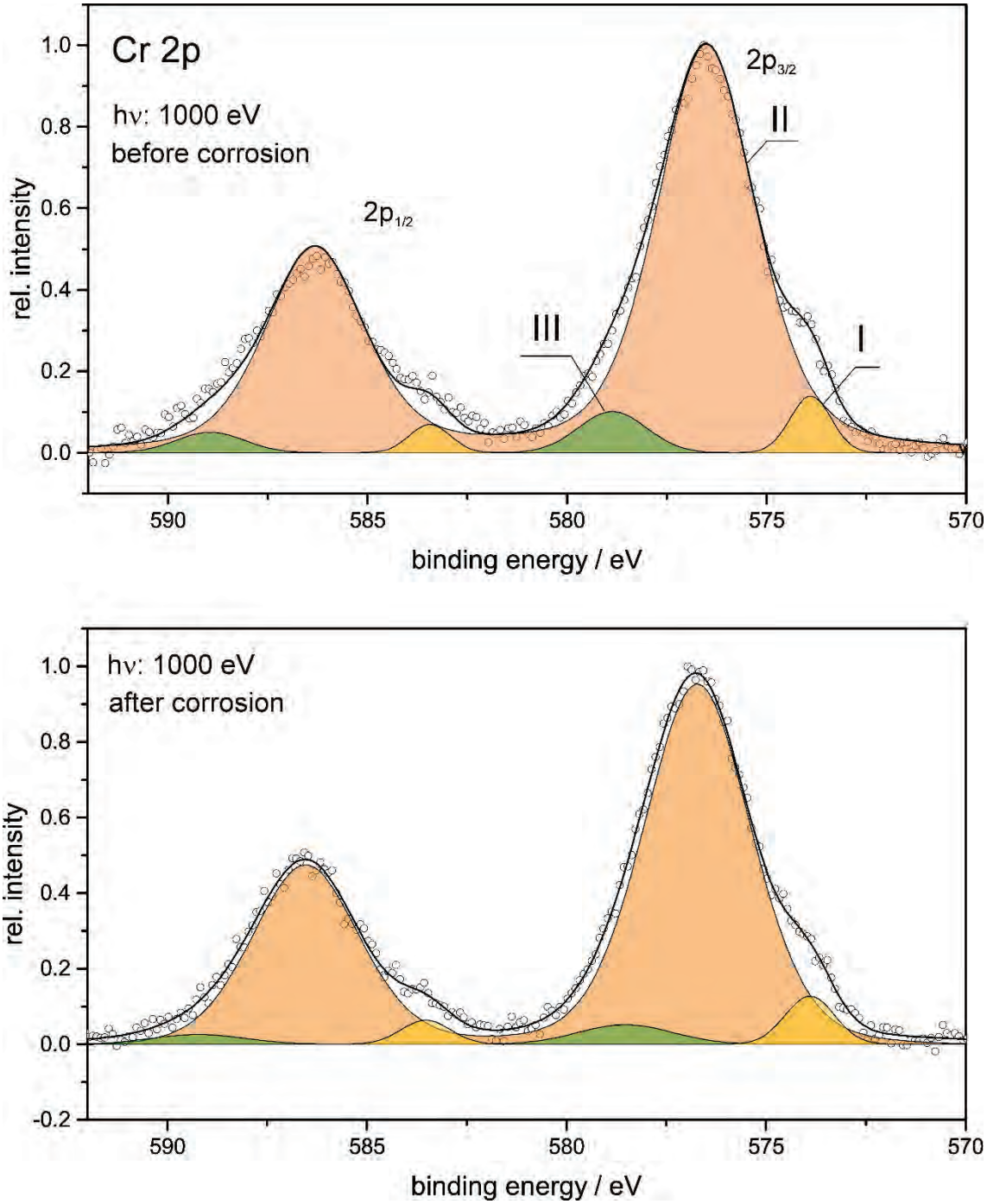

Fig. 8.7 Cr 2p core level spectra of the 309S surface before and after the polarization experiment. Excitation energy: 1000 eV

The Cr 2p core level signal before and after the corrosion experiment is shown in Fig. 8.7. The signal can be deconvoluted in three lines, the $2p^{3/2}$ of which are: I: 573.88 eV, II: 576.52 eV and III: 578.82 eV. The line I can be assigned to Cr metal. The line II matches with the reported binding energy for Cr_2O_3. The line III can be assigned to CrO_3.

The binding energy of 576.52 eV for Cr $2p^{3/2}$ of peak II is between the value assigned to Cr_2O_3 (576.1 eV) and that for $Cr(OH)_3$ (577.4 eV). The corresponding binding energy of O 1s for Cr_2O_3, on the other hand, is about 530.1 eV, i.e. 0.5 eV lesser than that observed, and which is closer to that assigned to $Cr(OH)_3$ or Cr(OH)O. This result lets infer a disordered oxide structure with -OH terminal bonds. In addition, the Cr $2p^{3/2}$ binding energy of peak II can be associated with a mixed $Fe_xCr_{3-x}O_4$ oxide, as reported by Allen et.al. /ALL 1989/.

Fig. 8.8 shows the Cr 2p core level spectra for a surface sensitive excitation energy of 630 eV. The spectra before and after the corrosion experiment can be deconvoluted in two lines. Peak I at 575.90 eV and Peak II at 577.10 eV. The former can be assigned to Cr_2O_3 or to $FeCr_2O_4$. The latter can be assigned to $Cr(OH)_3$.

Further information about the chemical environment of Cr at the outermost part of the surface is provided by the Cr 3s core level spectra shown in Fig. 8.9. Before corrosion, the spectrum can be deconvoluted in three components, from which peak I and II, appearing at 74.16 eV and 74.94 eV, predominates. The former can be assigned to Cr metal. The latter represents Cr(III), whose chemical environment can be described by $FeCr_2O_4$, $CrCl_3$ and Cr_2O_3. After the corrosion experiments, the signal of Cr metal vanishes and a peak III appears at 76.42 eV. The chemical shift ΔE: +1.28 eV between peak II and III is similar to the $2p^{3/2}$ shift of $Cr(OH)_3$ respective Cr_2O_3. This suggests that peak III corresponds to the oxidation of Cr metal sites by formation of Cr-OH bonds.

Fig. 8.10 shows the Mo 3d and S 2s core level spectra before and after the corrosion experiments for $h\nu$: 1000 eV. The double peaks $3d^{5/2}$ and $3d^{3/2}$ of molybdenum appear superposed to the 2s signal of sulfur. For Mo, $3d^{5/2}$ lines appear at 227.59 eV and 231.55 eV before the corrosion experiment. The former can be ascribed to Mo metal. The latter is between the binding energies reported for MoO_2 (229.60-230.00 eV) and MoO_3 (232.20 – 232.40 eV). Thus, it is probable that this signal corresponds to a disordered oxide (Lorentzian FWHM of 2.53) constituted by a mix of Mo(IV) and Mo(VI).

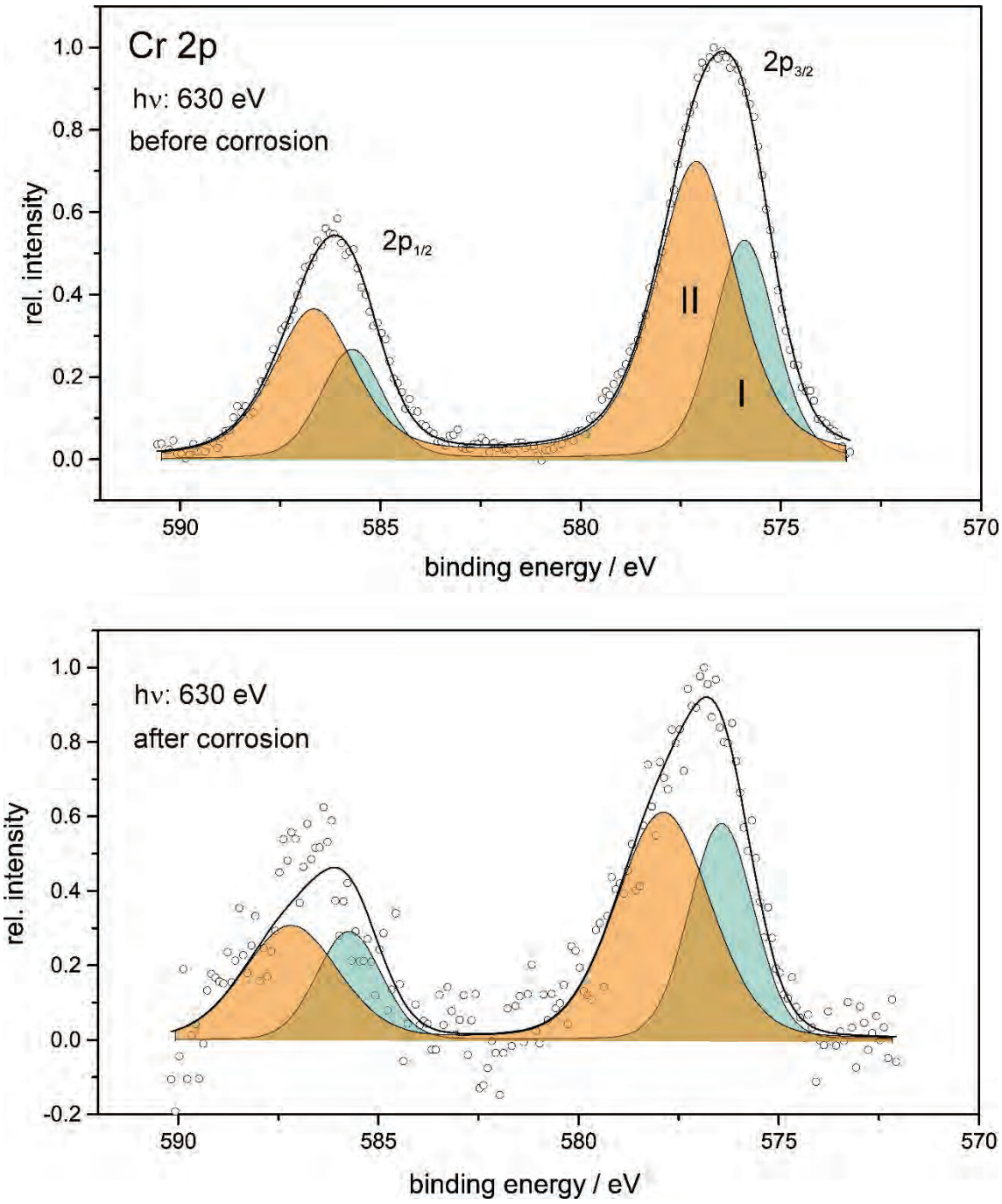

Fig. 8.8 Cr 2p core level spectra of the 309S surface before and after the polarization experiment. Excitation energy: 630 eV

The spectrum shows the superposition of a single peak at 228.85 eV which can be assigned to elemental S. After the polarization experiment, a predominating Mo 3d signal at 229.76 eV ($3d^{5/2}$) appears, indicating the growth of an oxide film constituted by Mo(IV). At the same time, an increase of the relative amount of Mo metal is also observed.

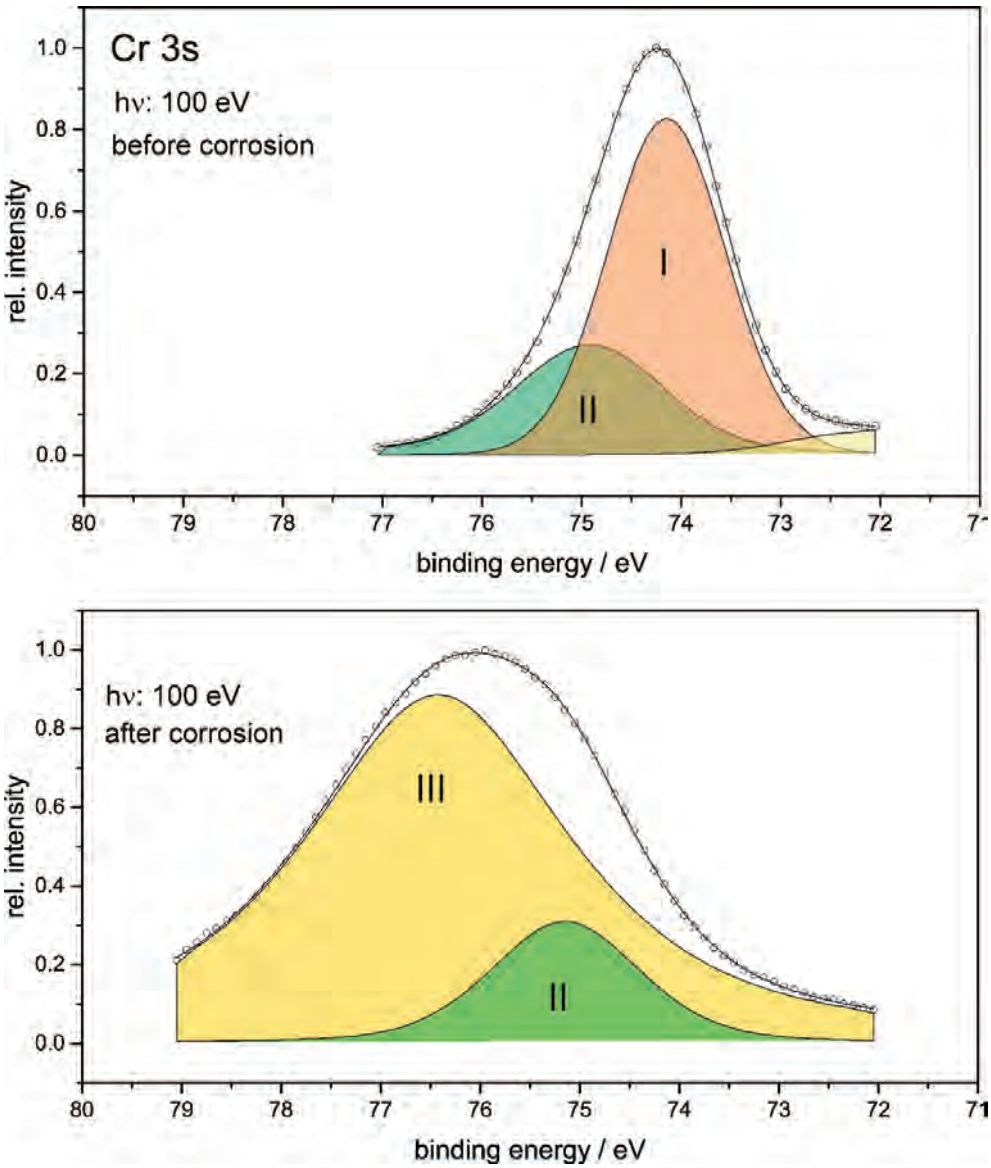

Fig. 8.9 Cr 3s core level spectra of the 309S surface before and after the polarization experiment. Excitation energy: 100 eV

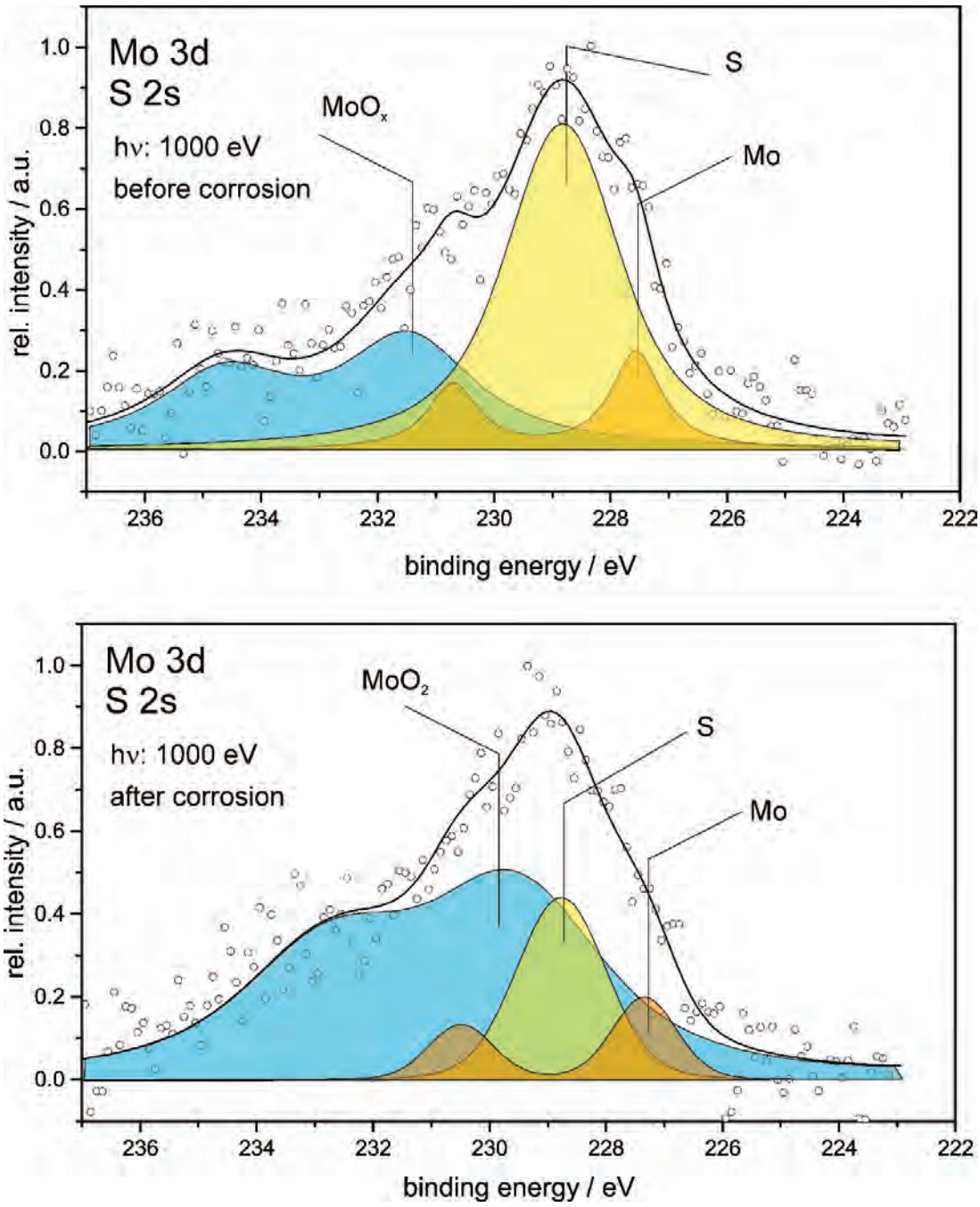

Fig. 8.10 Mo 3d and S 2s core level spectra of the 309S surface before and after the polarization experiment. Excitation energy: 1000 eV

The spectra measured at hν: 300 eV let get a deeper insight into the first atomic layer of the surface. Only a sulfur signal with 2s peaks at 229.69 eV and 231.39 eV can be measured. They can be ascribed to elemental S and an oxidized form, such as SO_4, respectively. The presence of sulfate was also reported in a recent investigation of Wang et.al. /WAN 2020/.

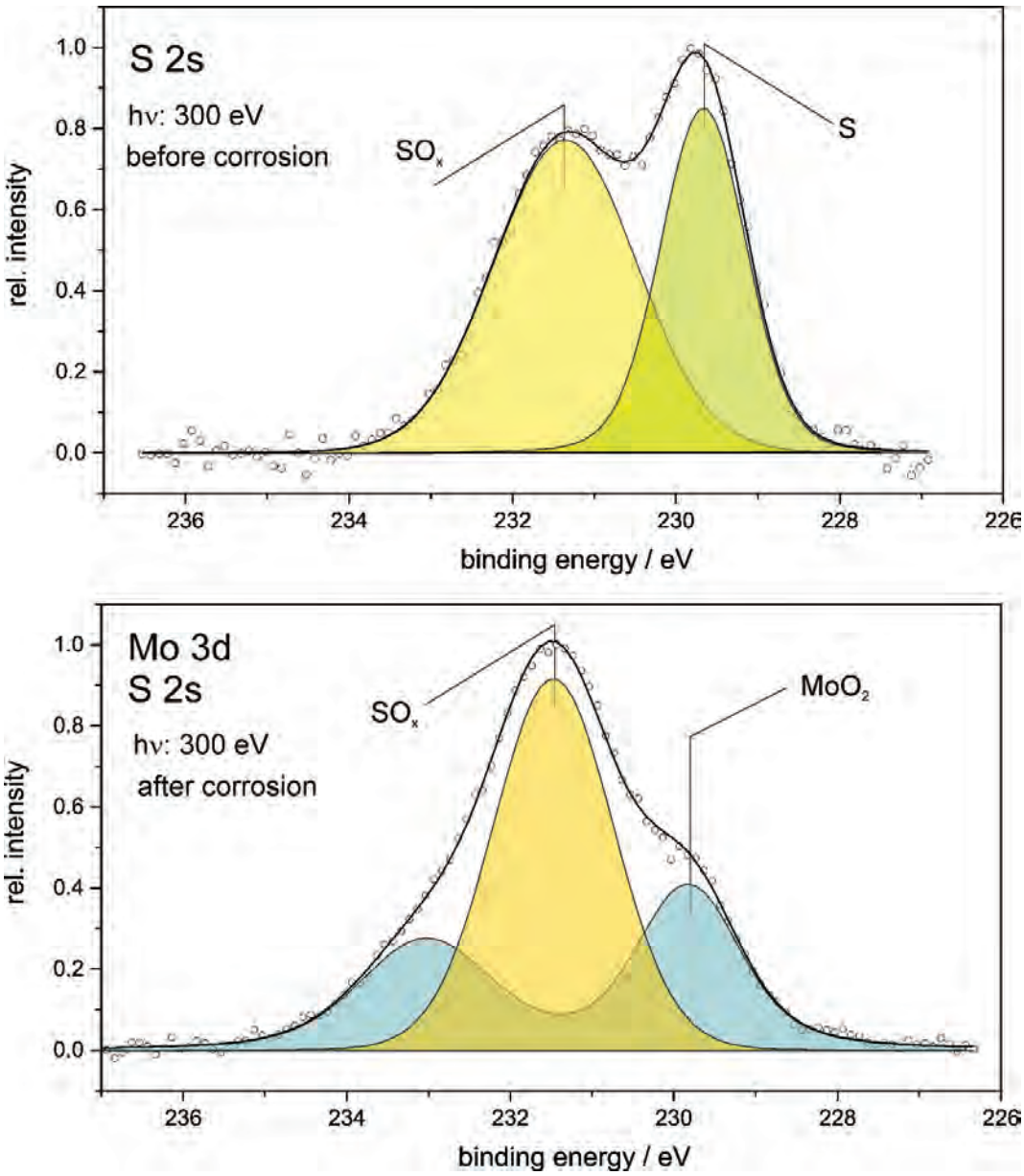

Fig. 8.11 Mo 3d and S 2s core level spectra of the 309S surface before and after the polarization experiment. Excitation energy: 300 eV

After the anodic polarization, only the 2s signal of oxidized sulfur appears together with the Mo 3d signal at 229.83 eV ($3d^{5/2}$), assigned to Mo(IV) oxide. The S 2p spectrum, on the other hand, can be deconvoluted in three components at 168.24 eV, 168.78 eV and 169.33 eV, i.e. shifted by +0.54 eV. These lines cannot strictly be ascribed to pure sulfate salts, because we are dealing with adsorbed anions. Thus, the different binding energies correlate with the different chemical environments of S in the mixed oxide.

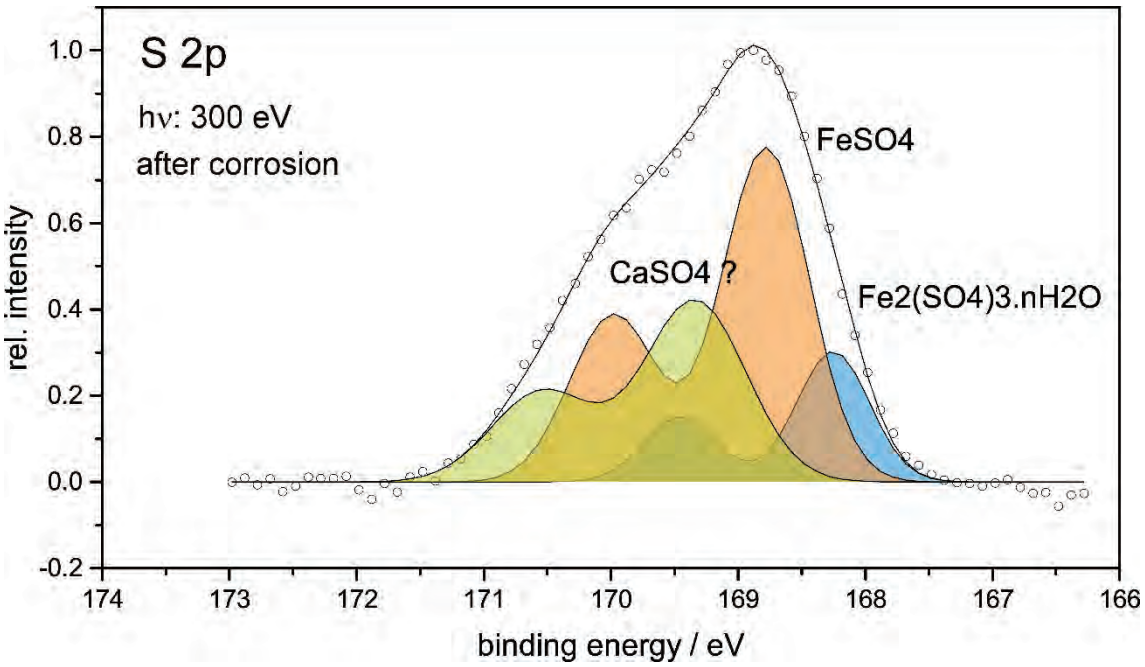

Fig. 8.12 S 2p core level spectra of the 309S surface after the polarization experiment. Excitation energy: 300 eV

9 Corrosion model

Fig. 9.1a depicts a graphical representation of the corrosion mechanism of steel 309S in Q3 solution, derived from the experimental evidence and thermodynamic calculations. The concentration of chloride and the solution acidity plays an essential role in the steel attack. The corrosion process starts with the nucleation of pits, i. e. with the breakdown of the native oxide film, involving the adsorption and penetration of chloride anions into the oxide. This generates a rupture of the oxide structure and the opening of a highly conductive site. At this point, the metal gets in contact with the solution at a very large anodic overpotential. As revealed by spectroscopic studies, sulfate anions play a decisive role hindering the nucleation of pit. It can be supposed that SO_4^{2-} and Cl^- compete for adsorption sites on the oxide surface, retarding the nucleation of pits. The large concentration of chloride and the absence of sulfate in Q2 solution hinders the passivation of steel.

Thermodynamics predicts that for an almost neutral pH of 5 to 6, Cr_2O_3, Fe^{2+}, Fe_2O_3 and Ni^{2+} should be the main corrosion products arising from a growing pit (see Fig. 4.6). Mo exerts a reinforcing effect on the passivity of steel. But it does not play any essential role on the growing of already nucleated pits. The formation of the chromium and iron oxides arises from the hydrolysis of Cr^{3+} and the oxidative hydrolysis of Fe^{2+} injected into the solution by the anodic reaction (eq. 9.1-2).

$$\mathbf{Cr^{3+}\ (aq) + 3\ H_2O \rightarrow Cr(OH)_3\ (s) + 3\ H^+\ (aq)} \qquad (9.1)$$

$$\mathbf{2\ Fe^{2+}\ (aq) + 3\ H_2O \rightarrow Fe_2O_3\ (s) + 6\ H^+ + 2\ e^-} \qquad (9.2)$$

These reactions generate a strong local acidification of the pit, which maintains its activity. The large surface concentration of Cr^{+3}, Fe^{2+} and Ni^{2+} induces an increase of the Cl^- concentration at the surface necessary to maintain the neutrality. Due to the almost saturated concentration of NaCl, it is plausible that the local increase of chloride concentration brings about the precipitation of a NaCl film. This effect was predicted by thermodynamic calculations using a data base for concentrated electrolytes (Pitzer concept) /MUN 2018/.

The higher density of oxides precipitated close to the surface induces a gravity drag of the acidified solution (Fig. 9.1b). This induces a corroding front moving downwards, where the metal degradation starts with a typical crystallographic type of attack. With progress of corrosion, the formation of a salt film brings about a leveling effect on the surface morphology by control of the ionic transport.

On applying large pressures, the drag effect is hindered by pressing the highly hydrated corrosion products against the pit surface and the acidified solution is propelled radially by a pressure induced drag.

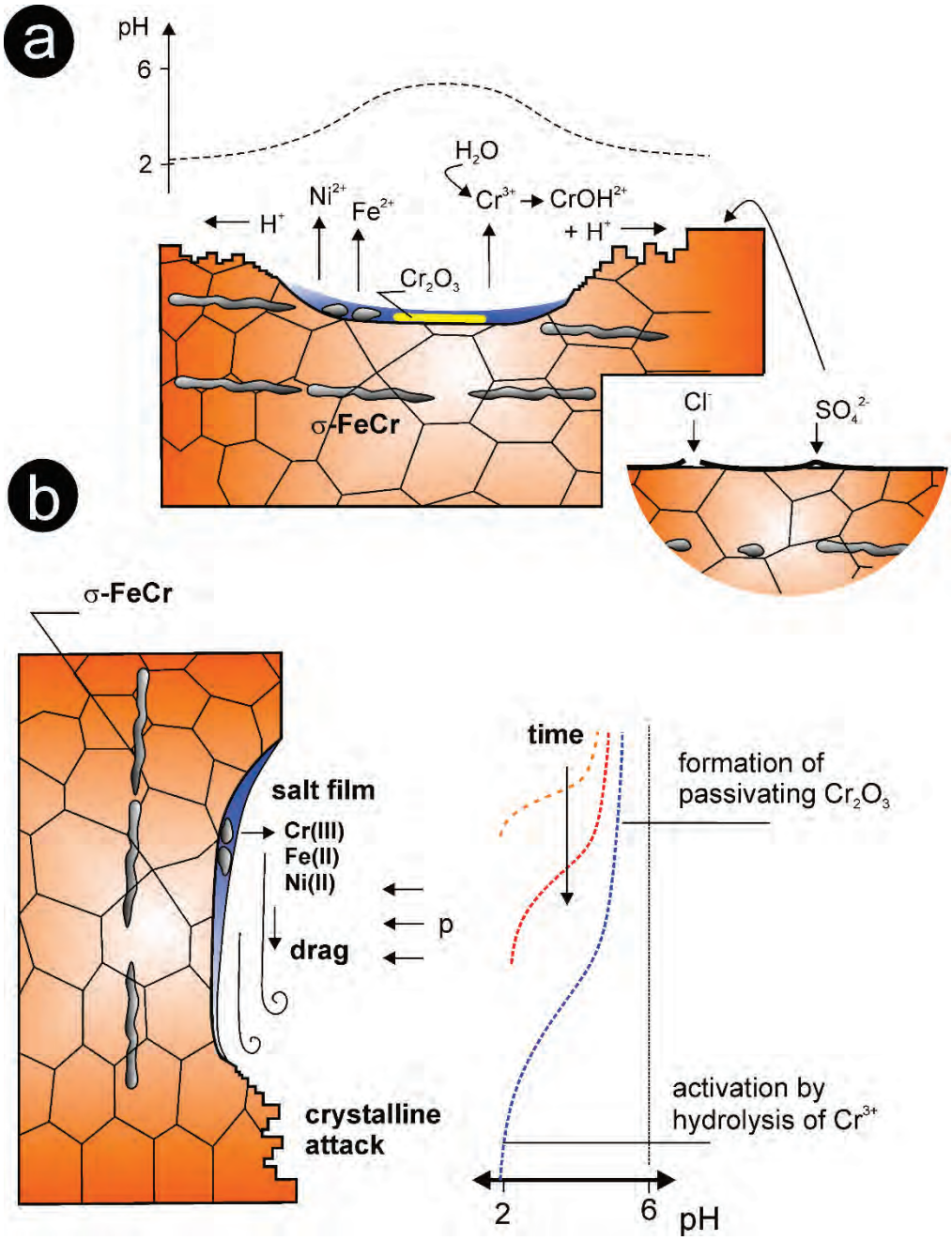

Fig. 9.1 Schematic depicting the main features of the corrosion mechanism of steel 309S in geological brines

The continuous accumulation of Cr-oxide during corrosion has a self-inhibiting effect. As the metal dissolution rate decreases, the local pH increases, and a series of other oxides start to precipitate. The spectroscopic analysis indicates the presence of Fe_2O_3, $FeCr_2O_4$, MoO_2 and hydrated Cr_2O_3. This result is in part in line with thermodynamic predictions.

The large anodic currents developed with the onset of pitting in the polarization experiments are limited by ionic transport by the salt film deposited on the surface. This leads to a leveling effect which reveals the grain structure of the austenitic matrix of the steel, with a larger concentration of Ni and Fe. The pits develop a semispherical shape releasing the ferritic phase, which dissolves slowly due to its large Cr/Fe ratio.

10 Conclusions and outlook

The aim pursued with the realization of the part A of the KORSO-project was to gain a significantly improved understanding of the metallic corrosion of the final metal barrier in high-level radioactive waste container concepts under conditions as close as possible to those prevailing in salt rock repositories. It is assumed, that after about 30 years the near environment of the containers reaches temperatures near 80 °C accompanied by a consumption of oxygen enclosed during the sealing process and an increase of the humidity to values close to condensation /KIN 2017/. These environmental conditions are expected to hold, at least for the next 500 years. Inasmuch as stainless steel 309S constitutes the last barrier in the German container concepts, the degradation process upon contact with saline solutions under these conditions, presupposes a prior fail of the outer and inner vessels of the container.

Combined electrochemical studies and chemical and morphological surface analysis have shown that stainless steel 309S is susceptible to localized dissolution, provided the surface potential reaches a value more positive than the breakdown potential. This potential is characterized by a rupture of the passive film and the nucleation of small pits, where conditions for a further dissolution and expansion of the attacked area are generated. In the pit, the steel surface, free of protecting oxide is exposed to a large concentration of chloride and a low pH generated by hydrolysis of dissolved ions. This study has shown that the oxidation of Cr to Cr^{3+} ions is largely responsible for the strong local acidification caused by its hydrolysis to the hydrated form of Cr_2O_3.

In potential controlled experiments, it was observed, that the breakdown and the re-passivation potentials decrease almost linearly with the temperature in the Q3 solution. The former is largely dependent of the presence of surface defects found commonly in scratches produced during mechanical polishing or at exposed sharp edges. This explains the large scattering observed in the determination of this value. The latter depends on the chemical environment generated during the anodic dissolution process and thus, this value is more reproducible. The potential range between breakdown and repassivation potential is considered as metastable, i.e. once a pit is nucleated, its growth cannot be stopped. The passive region vanishes at temperature close and higher than 80 °C. Thus, the re-passivation potential can be considered as the limit value for corrosion protection: these are -0.20 V (Ag/AgCl 1 M KCl) at 20 °C and -0.35 V (Ag/AgCl 1 M KCl) at 80 °C.

The effect of pressures up to 50 bars was analyzed. It was found that pressure exerts a large influence on the pit nucleation process, shifting the breakdown potential towards more anodic values. This is probably caused by a compression of the corrosion products generated in the early birth of a pit, sealing the site of the oxide rupture. This, in turn provides certain additional protection. Pressure, on the other hand, does not exert any passivating effect once the pit has started to grow. Only different morphological evolution of the pit during growth were found at low and high pressures. In the former case, the drag of solution produced by falling of dense corrosion products released in vertical samples generates an almost linear and vertical growth of pits leaving stripes of corroded material. In pressured solutions, however, the growth of pits is rather radial and the possibility of formation of deep pits is more probable. The corrosion course in Q3 solution is condensed in Fig. 9.1.

In Q3 (NaCl-saturated) solutions the stabilization of pits is promoted by the formation of a salt film hindering the rebuilding of the oxide. The ohmic-control established by the salt film, on the other hand, introduces a leveling effect in the dissolution process. As a result, the lateral growth with formation of hollow pits is favored.

Although the present study contributes to the knowledge of the corrosion of stainless steel 309S in concentrated geological brines, it gives rise to new questions necessary to be investigated. In real conditions, the surface of containers is exposed to differentiated chemical environments given by different degrees of humidity, different local salt composition, different hydrological pressures and internal stress, especially in welding regions. The formation of almost spherical pits may result in stress concentration points for the container material under tensile stress. This, in turn can lead to the onset of stress corrosion cracking and thus, to the failure of the barrier. Another important factor is the creation of half-cell elements originated by different electrochemical activities of the phases of the steel, different humidity grades or stress gradients. They may be harmful for the stability of the container under mechanical stress. In fact, stainless steel 309S is without doubt susceptible to undergo localized corrosion in contact with concentrated geological brines.

This work shows that the corrosion resistance of austenitic steel 306S is not large enough to withstand the conditions that would develop after a failing of container in a salt rock disposal. Temperatures higher than 80 °C cause the vanishment of passivity. The concentration of stress in growing pits, on the other hand, has bad consequences on the wall integrity and the induction to stress corrosion cracking is an additional critical factor

that should be still investigated. This factor would just lead to an acceleration of the rupture of the barrier.

The hydrolysis reaction of dissolved chromium is the driving force for the loss of passive behavior. The alloy dissolution leaves hydrated Cr_2O_3 and hematite as main products. The formation of spinel products $Fe_xNi_yCr_zO_{(3/2\ x\ +\ y\ +3/2\ z)}$ is also possible. Its identification is difficult to be performed, due to the lack of reference XPS-spectra for these compounds. The acidity produced by chromium hydrolysis is a factor contributing to the stabilization of pit, but pit nucleation is enabled by the large concentration of chloride. It was shown that the presence of small amounts of sulfate exerts a mitigating effect on the corrosion of steel 309S. This finding provides a possible starting point for future approaches to mitigate canister corrosion by adjusting the chemical milieu in the near field of the radioactive waste canisters.

Dissemination of the work

The progress of this project was presented in intern seminars of the GRS and regular meetings of the project partners. Specially the international dissemination of this work is worthy to be mention:

- A.G. Muñoz, D. Schild, Corrosion of Steel in High-level Radioactive Waste Rock Repositories: Kinetics and Thermodynamics., Oral presentation and Proceeding of NACE 2018, April 2018, Phoenix, AZ.
- A.G. Muñoz, D. Schild, Corrosion of Austenitic Steel in Geochemical Near-Field Conditions of High-Level Radioactive Waste Rock Repositories, Oral presentation and Proceeding of EUROCORR 2018, September 2018, Cracow, Poland.
- Muñoz, A.G., Schild, D., Corrosion mechanisms of austenitic steel in salt rock repositories of high-level radioactive waste, 235th ECS Meeting (The Electrochemical Society), Dallas, TX (USA), 26.-30. Mai 2019 (oral presentation).

Acknowledgements

The author gratefully acknowledges the funding received by the Federal Ministry of Economic Affairs and Energy (BMWi), represented by the Project Management Agency Karlsruhe (PTKA-WTE), contract no. 02E11496A.

The author is also sincerely thankful for fruitful cooperation with Dr. Wolfram Calvet from Helmholtz Center Berlin – Bessy II and the invaluable assistance of Dr. Thorsten Meyer.

References

/ALL 1989/ Allen, G.C., Harris, S.J., Jutson, J.A., Dyke, J.M., A study of a number of mixed transition metal oxide spinels using X-ray photoelectron spectroscopy. Appl. Surf. Sci., 37 (1989) 111-134.

/BAB 2002/ Baba, H., Kodama, T., Katada, Y., Role of nitrogen on the corrosion behavior of austenitic stainless steels, Corros. Sci., 44 (2002) 2393-2407.

/BAR 2014/ Barret, N., et al., Microscopic work function anisotropy and surface chemistry of 316 L stainless steel using photoelectron emission microscopy, J. Electron. Spectrosc. Relat. Phenom., 195 (2014) 117-124.

/BEA 1992/ Beamson, G., Briggs, D., High resolution XPS of organic polymers - The Scienta ESCA300 Database Wiley Interscience, 1992.

/BEK 1979/ Beck, T.R., Alkire, R.C., Occurrence of salt films during initiation and growth of corrosion pits, J. Electrochem. Soc., 126 (1979) 1662-1666.

/BEK 1984/ Beck, T.R., Salt film formation during corrosion of aluminum, Electrochimica Acta, 29 (1984) 485-491.

/BEN 2008/ Bennett, D.G., Gens, R., Overview of European Concepts for High-level Waste and Spent Fuel Disposal with Special Reference Waste Container Corrosion, J. Nucl. Mat., 379 (2008) 1-8.

/BER 2016/ von Berlepsch, T., Haverkamp, B., Salt as a Rock for the Geological Repository for Nuclear Waste, Elements, 12 (2016) 257-262.

/BER 2017/ Bertrams, N., Herold, P., Herold, M., Krone, J., Lommerzheim, A., Prignitz, S., Kuate, E.S., Entwicklung eines technischen Konzeptes für ein generisches Endlager für wärmeentwickelnde Abfälle und ausgediente Brennelemente im Kristallingestein in Deutschland, Bericht FKZ 02E11516, DBE Tec GmbH, 2017, Peine, Germany.

/BER 2020/ Bertrams, N. et. al., Grundlagen zur Bewertung eines Endlagersystems in flach lagernden Salzformationen, RESUS - Technical Report GRS-568, Gesellschaft für Anlagen- und Reaktorsicherheit GRS gGmbH, Köln, 2020.

/BEV 1999/ Beverskog, B., Puigdomenech, I., Pourbaix diagrams for the ternary system of iron-chromium-nickel, Corrosion, 55 (1999) 1077-1087.

/DIA 1996/ Díaz, J., Paolicelli, G., Ferrer, S., Comin, F., Separation of the sp^3 and sp^2 components in the C1s photoemission spectra of amorphous carbon films, Phys. Rev. B, 54 (1996) 8064-8069.

/FAR 1999/ Farrell, J., Bostick, W.D., Jarabek, R.J., Fiedor, J.N., Uranium removal from ground water using zero valent iron media, Ground Water, 37 (1999) 618-624.

/FRA 2011/ Franke, P., Seifert, H.J., (Ed.), Thermodynamic properties of inorganic materials compiled by SGTE, Subvolume C, Ternary steel systems, Part 1, Landolt-Börnstein Series, Vol. 19, Springer, Heildelberg, 2011.

/GRA 2016/ Grambow, B., Geological disposal of radioactive waste in clay, Elements, 12 (2016) 239-245.

/GRE 2018/ Greczynski, G., Hultman, L., Reliable determination of chemical state in x-ray photoelectron spectroscopy based on sample-work-function referencing to adventitious carbon: Resolving the myth of apparent constant binding energy of the C 1s peak, Appl. Surf. Sci. 451 (2018) 99-103.

/HAS 2019/ Hassel, Th., Köhler, A., Kurt, Ö.S., Das ENCON-Behälterkonzept – Generische Behältermodelle zur Einlagerung radioaktiver Reststoffe für den interdisziplinären Optionsvergleich, ENTRIA-Arbeitsbericht-16, Institut für Werkstoffe, Leibniz-Universität Hannover (2019), Hannover, Germany.

/ISA 1973/ Isaacs, H.S., The behavior of resistive layers in the localized corrosion of stainless steel, J. Electrochem. Soc., 120 (1973) 1456.

/KAG 2003/ Kang, T.-H., Direct image observation of the initial forming of passive thin film on stainless steel surface by PEEM, Appl. Surf. Sci., 212-213 (2003) 630-635.

/KIE 2001/ Kienzler, B., Loida, A., Endlagerrelevante Eigenschaften von hochradioaktiven Abfallprodukten, Forschungszentrum Karlsruhe, Technical Report FZKA 6651, Karlsruhe, 2001.

/KIN 2006/ King, F., Padovani, C., Review of the corrosion performance of selected canister materials for disposal of UK HLW and/or spent fuel, Corros. Eng. Sci. Technol., 46 (2011) 82-90.

/KIN 2007/ King, F., Overview of a Carbon Steel Container Corrosion Model for a Deep Geological Repository in Sedimentary Rock, Nuclear Waste Management Organization Report NWMO TR-2007-01, Toronto, Canada, 2007.

/KIN 2010/ King, F., Canister materials for the disposal of nuclear waste, in Comprehensive nuclear materials, Oxford, UK, Elsevier, 2010.

/KIN 2010a/ King, F., Shoesmith, D.W., Nuclear waste canister materials, corrosion behaviour and long-term performance in geological systems in Geological repository systems for safe disposal of spent nuclear fuels and radioactive waste, Ahn, J., Apted, M. (Eds.), Oxford, UK, Woodhead Publishing, 2010.

/KIN 2014/ King, F., Kolář, M., Keech, P.G., Simulations of Long-term Anaerobic Corrosion of Carbon Steel Containers in Canadian Deep Geological Repository, Corr. Eng. Sci. Tech., 49 (2014) 455-459.

/KIN 2017/ King, F., Nuclear waste canister materials: Corrosion behavior and long-term performance in geological repository systems, in Geological Repository Systems for Safe Disposal of Spent Nuclear Fuels and Radioactive Waste (Second Edition), Apted, M.J, Ahn, J. (Editors), p. 365-408, Woodhead Publishing Series in Energy, Elsevier, 2017.

/KIN 2020/ King, F., Canister Materials for the Disposal of Nuclear Waste in Comprehensive Nuclear Materials 2nd Ed., Konings, R.J.M., Stoller, R.E. (Editors), Elsevier, Amsterdam, 2020.

/KIR 1999/ Kirklin, D.R., Properties of materials and systems of importance to environmental fates and remediation. III. Review of previous thermodynamic property values for chromium and some of its compounds, J. Phys. Chem. Ref. Data, 28 (1999) 1675-1704.

/KUR 2007/ Kursten, B., Smailos, E., Azkarate, I., Werme, L., Smart, N.R., Santarini, G., Technical report, FIKW-CT-2001-20138, State-of-the-art document on the corrosion behaviour of container materials, Luxemburg, COBEMA, European Commission, 2007.

/LAY 1998/ Laycock, N.J., Newman, R.C., Temperature dependence of pitting potentials for austenitic stainless steels above their critical pitting temperature, Corr. Sci., 40 (1998) 887-902.

/LEC 1966/ Leckie, H.P., Uhlig, H.H., Environmental factors affecting the critical potential for pitting in 18-8 stainless steel, J. Electrochem. Soc., 113 (1966) 1262.

/MAC 1987/ Macdonald, J.R., Impedance spectroscopy. Emphasizing solid materials and systems, John Wiley & Sons, NY, 1987.

/MAN 1975/ Mankowski, J., Szklarska-Smialowska, Z., Studies on accumulation of chloride ions in pits growing during anodic polarization, Corros. Sci., 15 (1975) 493-501.

/MAN 1977/ Mankowski, J., Szklarska-Smialowska, Z., The effect of the specimen position on the shape of corrosion pits in an austenitic stainless steel, Corros. Sci., 17 (1977) 725-735.

/MCG 2008/ McGuire, M., Stainless steels for design engineers, ASM International® Materials Park, Ohio, USA, 2008.

/MCI 2003/ McIntyre, N.S., et al., New frontiers in X-ray photoelectron spectroscopy, Vacuum, 69 (2003) 63-71.

/MIL 2002/ Miller, D.J., Biesinger, M.C., McIntyre, N.S., Interactions of CO2 and CO at fractional atmosphere pressures with iron and iron oxide surfaces: onepossible mechanism for surface contamination?, Surf. Interface Anal. 33 (2002) 299–305.

/MOE 2020/ Mönig, J., Bertrams, N., Fahrland, S., Frenzel, B., Maßmann, J., Müller-Hoeppe, N., Reinhold, K., Rübel, A., Schubarth-Engelschall, N., Simo, E., Thiedau, J., Weber, J. R., Wolf, J., Empfehlungen zur sicherheitsgerichteten Anwendung der geowissenschaftlichen Abwägungskriterien des StandAG (Synthesebericht), GRS-567, 08/2020, ISBN 978-3-947685-53-8, 2020.

/MOU 1995/ Moulder, J.F., Stickle, W.F., Sobol, P.E., Bomben, K.D., Handbook of X-ray photoelectron spectroscopy, Eds.: Chastain, J, King Jr., R.C., ULVAC-PHI, Inc., Japan; Physical Electronics USA, Inc, 1995.

/MUN 1999/ Muñoz, A.G., Bessone, J.B., Pitting of aluminium in non-aqueous chloride media, Corros. Sci., 41 (1999) 1447-1463.

/MUN 2018/ Muñoz, A.G., Schild, D., Corrosion of Steel in High-level Radioactive Waste Rock Repositories: Kinetics and Thermodynamics, Proceeding of CORROSION 2018, NACE, April 2018, Phoenix, AZ.

/NAT 2002/ Natishan, P.M., et al., X-ray absorption near edge structure and X-ray photoelectron spectroscopy studies of chloride in passive oxide films, Electrochim. Acta, 47 (2002) 3131-3136.

/NIN 2020/ Ninomiya, K., Kamitani, K., Tamenori, Y., Tsuruta, K., Okajima, T., Yoshimura, D., Sawada, H., Kinoshita, K., Nishibori, M., Observation of chemical state for interstitial solid solution of carbon in low-carbon steel by soft X-ray absorption spectroscopy, ISIJ International, 60 (2020) 114-119.

/NIS 2012/ Naumkin, A.V., Kraut-Vass, A., Gaarenstroom, S.W., Powell, C.J., NIST X-ray photoelectron spectroscopy database, NIST standard reference database 20, Version 4.1, DOI: http://dx.doi.org/10.18434/T4T88K, Gaithersburg, MD, USA, 2012.

/OLS 2003/ Olsson, C.-O.A., Landolt, D., Passive films on stainless steels-chemistry, structure and growth, Electrochim. Acta., 48 (2003) 1093-1104.

/PEI 2011/ Peiffer, F., McStocker, B., Gründler, D., Abfallspezifikation und Mengengerüst, Basis Ausstieg aus der Kernenergienutzung, Vorläufige Sicherheits-analyse Gorleben, Bericht zum Arbeitspaket 3, Gesellschaft für Anlagen- und Reaktorsicherheit (GRS) mbH, GRS-278, ISBN 978-3-939355-54-2, 2011.

/REN 2007/ Renault, O., Energy-filtered XPEEM with NanoESCA using synchrotron and laboratory X-ray sources: principles and first demonstrated results, Surf. Sci., 601 (2007) 4727-4732.

/SCH 1949/ Schaeffler, A.L.,Constitution diagram for stainless steel weld metal, Metal Prog., 56 (1949) 680-680B.

/SEA 1986/ Seah, M.P., Data compilations: their use to improve measurement certainty in surface analysis by aes and xps, Surf. Interf. Anal. 9 (1986) 85.

/SEA 1998/ Seah, M.P., Gilmore, I.S., Beamson, G., XPS: Binding energy calibration of electron spectrometers 5 – Re-evaluation of the reference energies, Surf. Interface Anal., 26 (1998) 642-649.

/SED 1996/ Sedriks, A.J., Corrosion of stainless steels, 2nd ed, New York, Wiley Interscience, 1996.

/SHO 2003/ Shoesmith, D.W., Kolar, M., King, F., A mixed potential model to predict fuel (uranium dioxide) corrosion within a failed nuclear waste container, Corrosion, 59 (2003) 802-816.

/SHO 2006/ Shoesmith, D.W., Assessing the corrosion performance of high-level nuclear waste containers, Corrosion, 62 (2006) 703-722.

/SIE 1967/ Siegbahn, K., Nordling, C., Fahlman A., Nordberg, R., Hedman, J., Johannson, G., Bergmark, T., Karlsson, S., Lindgren, T., Lindberg, B., Atomic, molecular and solid-state structure studied by means of electron spectroscopy, Nova Acta Regiae Soc. Sci. Ups 1967; IV: 20.

/SMA 2003/ Smailos, E., Cuñado, M.Á., Azkarate, I., Kursten, B., Marx, G., Long-term performance of candidate materials for HLW/spent fuel disposal containers, Technical report, Forschungszentrum Karlruhe, FZKA 6809 (2003), Karlsruhe. Germany.

/STA 2017/ Site selection law from 5th May 2017 (BGBl. I S. 1074), modified at by the article 2 paragraph 16 of the law from 20th July 2017 (BGBl. I S. 2808).

/SWI 1985/ Swift, P., Adventitious carbon-the panacea for energy referencing?, Surf. Interface Anal., 4 (1982) 47-51.

/WAN 2020/ Wang, Z., Seyeux, A., Zanna, S., Maurice, V., Marcus, P., Chloride-induced alterations of the passive film on 316L stainless steel and blocking effect of pre-passivation, Electrochim. Acta, 329 (2020) https://doi.org/10.1016/j.electacta.2019.135159.

List of figures

List of tables

Gesellschaft für Anlagen- und Reaktorsicherheit (GRS) gGmbH

Schwertnergasse 1
50667 Köln
Telefon +49 221 2068-0
Telefax +49 221 2068-888

Forschungszentrum
Boltzmannstraße 14
85748 Garching b. München
Telefon +49 89 32004-0
Telefax +49 89 32004-300

Kurfürstendamm 200
10719 Berlin
Telefon +49 30 88589-0
Telefax +49 30 88589-111

Theodor-Heuss-Straße 4
38122 Braunschweig
Telefon +49 531 8012-0
Telefax +49 531 8012-200

www.grs.de

ISBN 978-3-949088-12-4